

AD-A225 042

Final Report
to
U.S. Air Force Office of Scientific Research
on

**MODELING OF MICROMECHANISMS OF FATIGUE
AND FRACTURE IN HYBRID MATERIALS**

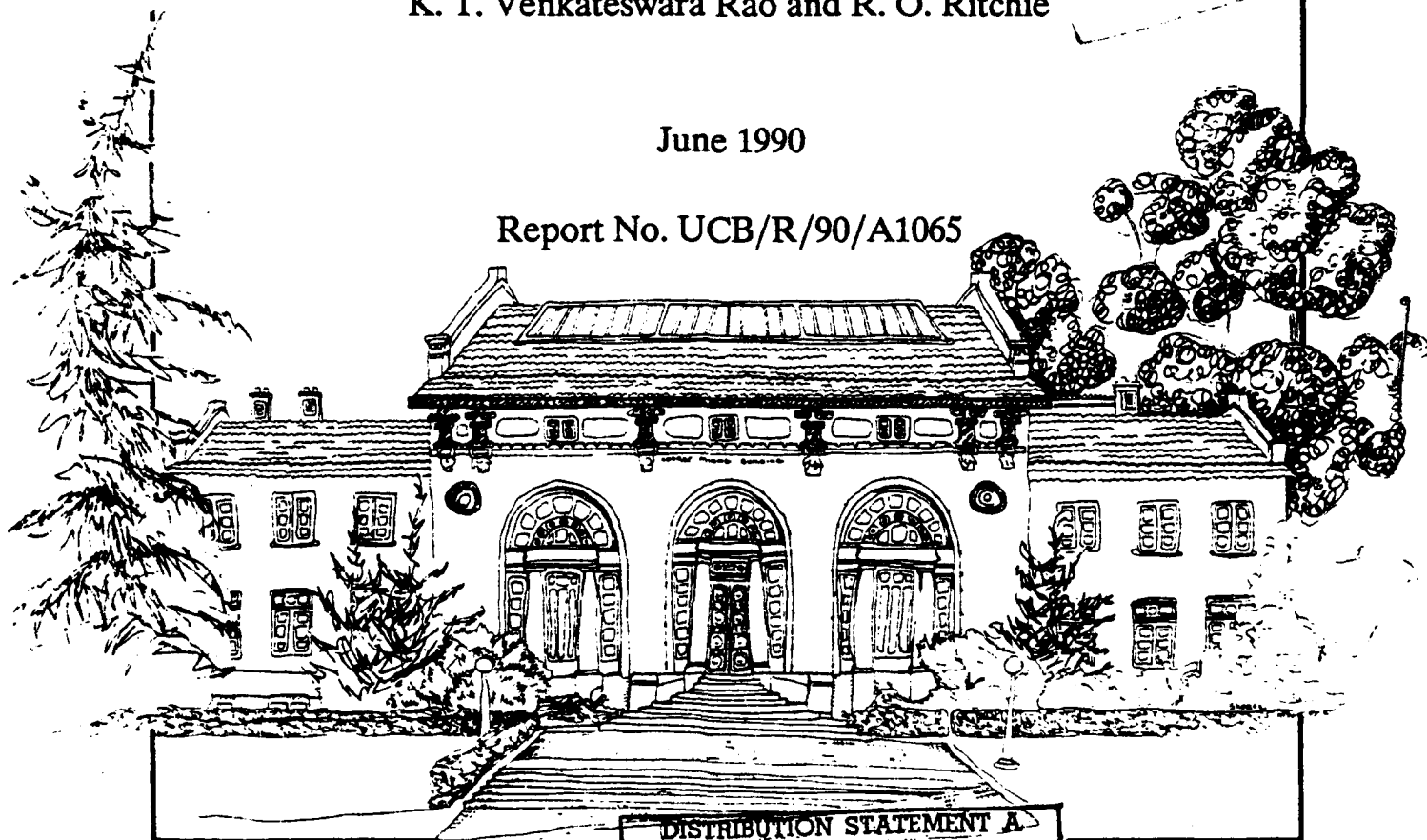
Grant AFOSR-87-0158
for period 15 April 1987 to 14 April 1990

by

L. H. Edelson, J.-K. Shang, S. C. Siu,
K. T. Venkateswara Rao and R. O. Ritchie

June 1990

Report No. UCB/R/90/A1065



DISTRIBUTION STATEMENT A

Approved for public release;
Distribution Unlimited

Department of Materials Science and Mineral Engineering
University of California, Berkeley, California 94720

90 07 30 027

DTIC
ELECTE
JUL 30 1990
S E D

REPORT DOCUMENTATION PAGE

1a. REPORT SECURITY CLASSIFICATION Unclassified			1b. RESTRICTIVE MARKINGS None		
2a. SECURITY CLASSIFICATION AUTHORITY Not Applicable			3. DISTRIBUTION / AVAILABILITY STATEMENT Not Applicable		
2b. DECLASSIFICATION / DOWNGRADING SCHEDULE Not Applicable			Approved for public release; Distribution Unlimited		
4. PERFORMING ORGANIZATION REPORT NUMBER(S) UCB/R/90/A1065			5. MONITORING ORGANIZATION REPORT NUMBER(S)		
6a. NAME OF PERFORMING ORGANIZATION Robert O. Ritchie, Dept. of Mat. Sci. & Minl. Eng.		6b. OFFICE SYMBOL (If applicable)	7a. NAME OF MONITORING ORGANIZATION Air Force Office of Scientific Research AFOSR/NE		
6c. ADDRESS (City, State, and ZIP Code) University of California Hearst Mining Building Berkeley, California 94720			7b. ADDRESS (City, State, and ZIP Code) Bldg. 410, Bolling AFB Washington, D.C. 20322 ATTN: Dr. A. H. Rosenstein, AFOSR/NE		
8a. NAME OF FUNDING / SPONSORING ORGANIZATION AFOSR		8b. OFFICE SYMBOL (If applicable) NE	9. PROCUREMENT INSTRUMENT IDENTIFICATION NUMBER AFOSR-87-0158		
8c. ADDRESS (City, State, and ZIP Code) Bldg 410 Bolling AFB DC 20332			10. SOURCE OF FUNDING NUMBERS		
			PROGRAM ELEMENT NO. 61102F	PROJECT NO. 2306	TASK NO. A1
			WORK UNIT ACCESSION NO.		
11. TITLE (Include Security Classification) MODELING OF MICROMECHANISMS OF FATIGUE AND FRACTURE IN HYBRID MATERIALS (Unclassified)					
12. PERSONAL AUTHOR(S) EDELSON, L.H. SHANG, J.-K., SIU, S. C., VENKATESWARA RAO, K. T., and RITCHIE, R. O.					
13a. TYPE OF REPORT Final		13b. TIME COVERED FROM 87/4/15 TO 90/4/14		14. DATE OF REPORT (Year, Month, Day) 1990 June 15	
15. PAGE COUNT 84					
16. SUPPLEMENTARY NOTATION					
17. COSATI CODES			18. SUBJECT TERMS (Continue on reverse if necessary and identify by block number)		
FIELD	GROUP	SUB-GROUP	Fatigue; Fracture Toughness; Subcritical Crack Growth; Metal-Matrix Composites; Laminates; Fatigue Cracks; Crack Closure; Crack Bridging; Aluminum Alloys; Titanium Alloys.		
19. ABSTRACT (Continue on reverse if necessary and identify by block number)					
<p>The obvious benefits of the design of aerospace structures using lighter materials with high specific strengths and stiffnesses had led to the development of numerous reinforced composite metallic and intermetallic materials, which have become serious commercial competitors to traditional monolithic metallic alloys. While significant advances in processing technology have made the fabrication of such hybrid materials more of an economic reality, their widespread use in airframes or other structures has been limited by serious deficiencies in mechanical properties, particularly ductility, toughness and fatigue. This problem is compounded by the lack of fundamental studies which provide a rational basis for the underlying sources of crack-propagation resistance, and in particular which define the critical role of composite microstructure. Accordingly, this program was aimed at studying the physics and micromechanisms of fatigue-crack growth resistance in laminate, discontinuously-reinforced and continuously-reinforced metal-matrix, and to a lesser extent intermetallic-matrix, composites, with special reference to the role of microstructure. The central hypothesis of this work is that crack-propagation behavior in these materials primarily results from mutual</p>					
20. DISTRIBUTION / AVAILABILITY OF ABSTRACT <input checked="" type="checkbox"/> UNCLASSIFIED/UNLIMITED <input type="checkbox"/> SAME AS RPT. <input type="checkbox"/> DTIC USERS			21. ABSTRACT SECURITY CLASSIFICATION Unclassified		
22a. NAME OF RESPONSIBLE INDIVIDUAL Robert O. Ritchie			22b. TELEPHONE (Include Area Code) (415) 442-0417		22c. OFFICE SYMBOL NE

competition between intrinsic toughening mechanisms, which increase the microstructural resistance to crack extension, and extrinsic mechanisms, which reduce the local "driving force" through crack-tip shielding. The program was focused on i) the role of crack bridging and crack deflection in influencing crack growth behavior in aluminum alloys reinforced with sheets of epoxy impregnated with high-strength unidirectional aramid fibers (ARALL Laminates®), ii) a comparison of long and microstructurally-small crack growth in cyclically-loaded aluminum alloys continuously-reinforced with SiC fibers, iii) studies on the fatigue behavior of TiC-particulate reinforced Ti-6Al-4V composites, and iv) a preliminary examination of the microstructure of titanium aluminides.

Report No. UCB/R/90/A1065

Final Report
to
U.S. Air Force Office of Scientific Research
on
**MODELING OF MICROMECHANISMS OF FATIGUE
AND FRACTURE IN HYBRID MATERIALS**

Grant No. AFOSR-87-0158
for period 15 April 1987 to 14 April 1990

submitted to

U.S. Air Force Office of Scientific Research
Bldg. 410, Bolling Air Force Base
Washington, D.C. 20322
Attention: Dr. Alan H. Rosenstein

Accession For	
NTIS GRA&I	<input checked="checked" type="checkbox"/>
DTIC TAB	<input type="checkbox"/>
Unannounced	<input type="checkbox"/>
Justification	
By	
Distribution/	
Availability Codes	
Dist	Avail and/or Special
A-1	

submitted by

L. H. Edelson, J.-K. Shang, S. C. Siu, K. T. Venkateswara Rao and R. O. Ritchie
Department of Materials Science and Mineral Engineering
University of California
Berkeley, California 94720

June 1990

TABLE OF CONTENTS

	Page
FORWARD.....	iv
ABSTRACT.....	v
1. INTRODUCTION	1
2. ARALL LAMINATES: ROLE OF CRACK BRIDGING	4
3. FATIGUE IN CONTINUOUSLY-REINFORCED COMPOSITES.....	30
4. TiC-PARTICULATE-REINFORCED Ti-6Al-4V COMPOSITES	52
5. TITANIUM ALUMINIDE INTERMETALLICS	59
6. ACKNOWLEDGEMENTS.....	81
7. PROGRAM ORGANIZATION AND PERSONNEL	81
8. PUBLICATIONS.....	82
9. DISTRIBUTION LIST	84

MODELING OF MICROMECHANISMS OF FATIGUE AND FRACTURE IN HYBRID MATERIALS

L. H. Edelson, J.-K. Shang, S. C. Siu, K. T. Venkateswara Rao and R. O. Ritchie

(Grant No. AFOSR-87-0158)

FORWARD

This manuscript constitutes the Final Report on Grant No. AFOSR-87-0158, administered by the U.S. Air Force Office of Scientific Research, with Dr. Alan H. Rosenstein as Program Manager. The work, covering the period April 15, 1987, through April 14, 1990, was performed under the direction of Dr. R. O. Ritchie, Professor of Materials Science, University of California at Berkeley, with Dr. K. T. Venkateswara Rao and J.-K. Shang (10/1 - 12/31/89) as Research Engineers, S. C. Siu and L. H. Edelson as graduate students, and D. Kovar as undergraduate aide.

ABSTRACT

The obvious benefits of the design of aerospace structures using lighter materials with high specific strengths and stiffnesses had led to the development of numerous reinforced composite metallic and intermetallic materials, which have become serious commercial competitors to traditional monolithic metallic alloys. While significant advances in processing technology have made the fabrication of such hybrid materials more of an economic reality, their widespread use in airframes or other structures has been limited by serious deficiencies in mechanical properties, particularly ductility, toughness and fatigue. This problem is compounded by the lack of fundamental studies which provide a rational basis for the underlying sources of crack-propagation resistance, and in particular which define the critical role of composite microstructure. Accordingly, this program was aimed at studying the physics and micromechanisms of fatigue-crack growth resistance in laminate, discontinuously-reinforced and continuously-reinforced metal-matrix, and to a lesser extent intermetallic-matrix, composites, with special reference to the role of microstructure. The central hypothesis of this work is that crack-propagation behavior in these materials primarily results from mutual competition between intrinsic toughening mechanisms, which **increase** the microstructural resistance to crack extension, and extrinsic mechanisms, which **reduce** the local "driving force" through crack-tip shielding. The program was focused on i) the role of crack bridging and crack deflection in influencing crack growth behavior in aluminum alloys reinforced with sheets of epoxy impregnated with high-strength unidirectional aramid fibers (ARALL Laminates®), ii) a comparison of long and microstructurally-small crack growth in cyclically-loaded aluminum alloys continuously-reinforced with SiC fibers, iii) studies on the fatigue behavior of TiC-particulate reinforced Ti-6Al-4V composites, and iv) a preliminary examination of the microstructure of titanium aluminides.

1. INTRODUCTION

In recent years, the need for lighter materials with high specific strengths and stiffnesses, coupled with major advances in processing, has led to the development of numerous composite or hybrid materials as serious competitors to traditional engineering alloys. The majority of such materials are reinforced with high-strength, high-modulus (and often brittle) second phases, in the form of fibers, whiskers, particles or laminated sheets, embedded in a more ductile metallic or polymeric matrix, although other permutations such as ceramic-ceramic composites are not uncommon. Often, the properties of hybrid materials are highly anisotropic compared to equivalent monolithic materials, showing both distinct improvements and distinct detriments in specific mechanical properties.

Of particular interest in the aerospace and defense industry are polymer- or ceramic-reinforced metal-matrix composites [1]. Here, much effort has been directed towards the development of high performance composites utilizing aluminum and titanium matrices [2]. Where very high strengths and moduli are required for specialized applications, particularly at temperatures 100 degrees or so above that normally contemplated for the corresponding monolithic alloy, the use of aligned continuous fibers has been considered to induce very high, directional properties [3]. Conversely, for lower cost applications where such extreme properties are not a requirement, discontinuous metal-matrix composites consisting of whisker, nodule, platelet or particulate reinforcement (e.g., typically involving up to 40 volume % of SiC) have been shown to offer substantially improved strength and modulus properties compared to conventional aluminum alloys [2-8]. In the latter case, the advantages of the discontinuous composites are that properties become essentially isotropic, and that fabrication can be achieved with standard metallurgical processing, such as powder metallurgy, direct casting, rolling, extrusion, etc. However, their disadvantage is poor ductility, toughness and fatigue-crack growth performance compared to that of the constituent matrix.

Where toughness and especially fatigue properties are a necessity, such as in tension-dominated, fatigue and fracture critical aircraft structures (e.g., fuselages, lower wings, tail skins), a third class of weight-sensitive metal-matrix composite, involving metal-organic polymer laminates, has shown particular promise [9-12]. Such hybrids, which consist of thin aluminum-alloy sheets bonded by adhesive impregnated with strong aramid fibers (ARALL Laminates®), show spectacular resistance to fatigue-crack growth without compromise in strength, and further retain all the traditional advantages of a metal, i.e., plasticity, impact strength, formability and machinability [12]. Whereas potential weight savings of between 15 and 30% have been projected for aircraft structures utilizing ARALL, the disadvantages of these materials are their current low resistance to shear or delamination, and their toughness or residual strength in the presence of a notch or through-thickness crack (in which the fibers are broken).

® ARALL Laminate is a registered trademark of the Aluminum Company of America.

Despite the radical impact of the potential widespread use of metal-matrix composites in the aerospace industry, it is perhaps surprising that relatively few systematic studies of a fundamental nature have been performed to relate mechanistically, and ultimately model, the role of the composite microstructure in controlling toughness and fatigue resistance in these materials. This is particularly important as crack-propagation resistance is often the limiting property. In fact, in a very recent review of SiC-reinforced aluminum alloy composites [2], it was concluded that fracture toughness was the least investigated aspect of their material behavior, and furthermore that "...the fracture science of (these) composites needs to be re-examined...". This lack of understanding is illustrated by the case of P/M aluminum alloys discontinuously reinforced with platelet SiC. These composites are relatively isotropic, light weight, high modulus, high strength materials with improved wear and creep resistance, which are economical to produce and easy to shape. However, with all these advantages, they are yet to be used for airframes or other critical structures, primarily because of their inadequate ductility and fracture toughness [5]. Clearly, the factors governing the toughness of composite microstructures are far more complex than in homogeneous materials. In fact, as stated by Harris, there is no simple recipe to date for predicting the properties in all composites [13], as the viable mechanisms for impeding crack growth are both numerous and in many cases extremely material specific.

An example of the complexities of toughening hybrid materials can be appreciated by considering the role of the interface. It is clear that crack extension will be affected by the presence of the interface, both at the microstructural level between the fiber and the matrix and at the macroscopic level as planes of weakness between separate laminations in a multiple laminate. However, it is by no means clear what the nature of the interface should be for optimum toughness. For most metal-matrix fiber composites, it is the perception that a strong interfacial bond is required between the matrix and fiber [2]. Many ceramic-ceramic composites, conversely, derive their best fracture resistance where the interfacial shear strength is weak, such that relative sliding along the interface permits the matrix crack to grow leaving the fibers intact, thus bridging the crack [14]. In fact, it is interesting to note that one of the few metal-matrix composites with excellent crack-growth resistance, namely ARALL Laminates, have a weak interface between the aramid fibers and epoxy matrix to permit controlled delamination and hence crack bridging by unbroken fibers [10].

Accordingly, the principal thesis of this study is to identify and model the salient micromechanism of toughening and fatigue resistance in each of the three classes of metal-matrix and intermetallic hybrid materials (laminates, continuous fiber and discontinuously reinforced composites), and specifically to relate these mechanisms to the characteristic features in the microstructure. The approach is considered to be novel in that it will employ, and optimize, the two distinct routes to achieve toughening in materials, namely *intrinsic* mechanisms, which enhance the material's resistance to crack advance, and *extrinsic* mechanisms, which locally reduce the "driving force" for such advance [15]. The aim of this work is to describe and model in a quantitative fashion the mechanisms of failure of advanced hybrid materials on the microstructural scale, to provide a basis for the rational design of new composite microstructures with improved fracture and fatigue properties.

1.1 References

1. S. Dermarkar, Metals and Materials, 2 (1986) p. 144.
2. S. V. Nair, J. K. Tien, and R. C. Bates, Int. Metals Rev., 30 (1985) p. 275.
3. D. L. McDanel, Metall. Trans. A, 16A (1985) p. 1105.
4. R. J. Arsenault, Mater. Sci. Eng., 64 (1984) p. 171.
5. Y. From and R. J. Arsenault, J. Metals, 38 (1986) p. 31.
6. W. A. Logsdon and P. K. Liaw, Eng. Fract. Mech., 24 (1986) p. 737.
7. D. R. Williams and M. E. Fine, in Fifth Intl. Conf. Composite Matls. (ICCM-V), W. C. Harrigan et al., eds., TMS-AIME, Warrendale, PA, 1985, p. 639.
8. D. L. Davidson, Metall. Trans. A, 18A (1987) p. 2215.
9. L. B. Vogelesang and J. W. Gunnink, "ARALL, a Material for the Next Generation of Aircraft. A State of Art," Report LR-400, Delft University of Technology, The Netherlands, 1983.
10. R. Marissen, Eng. Fract. Mech., 19 (1984) p. 261.
11. R. W. Schultz, M. A. Gregory, and J. L. Teply, in Proc. First OMAE Specialty Symp. on Offshore and Arctic Frontiers, M. M. Salama, ed., American Society of Mechanical Engineers, New York, NY, 1986.
12. R. J. Bucci, L. N. Mueller, R. W. Schultz, and J. L. Prohaska, "Results from a Cooperative Test Program on ARALL, Aramid Aluminum Laminate," ALCOA Report, Aluminum Company of America, Alcoa Center, PA, 1986.
13. B. Harris, Metal Science, 14 (1980) p. 351.
14. A. G. Evans, M. D. Thouless, D. P. Johnson-Walls, E. Y. Luh, and D. B. Marshall, in Proc. Fifth Int. Conf. on Composite Materials (ICCM-V), W. C. Harrigan et al., eds., TMS-AIME, Warrendale, PA, 1985, p. 543.
15. R. O. Ritchie, Mater. Sci. Eng., 103A (1988) p. 15.

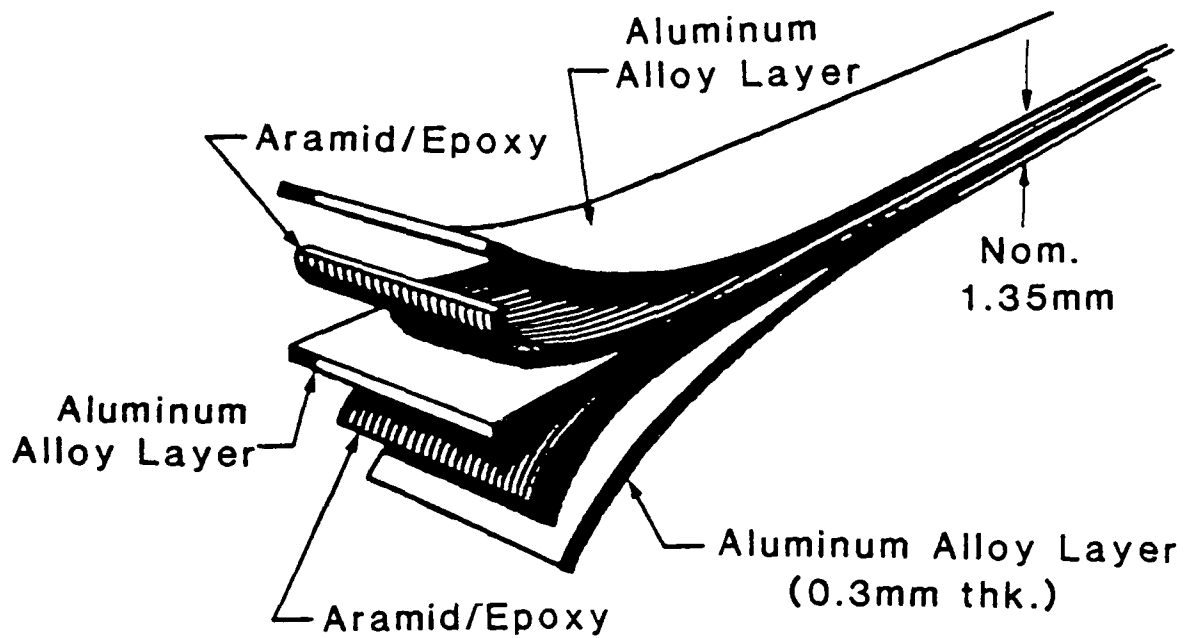
2. FATIGUE-CRACK PROPAGATION IN ARALL LAMINATES: ROLE OF CRACK-TIP SHIELDING FROM CRACK BRIDGING

2.1 Introduction

Aramid-fiber reinforced aluminum-alloy laminates (ARALL®) are a new class of hybrid materials which consist of alternating layers of thin aluminum-alloy sheets bonded by a structural metal adhesive impregnated with high-strength unidirectional aramid fibers (Fig. 2.1). Originally developed for fatigue-critical aircraft structures where up to 50% potential weight savings have been predicted [1-4], these composites show a range of attractive, albeit directional, properties, including 15-20% lower density, up to 60% higher strength (at comparable stiffness), good impact and damping properties, and most importantly superior fatigue crack-propagation resistance, compared to monolithic high-strength aluminum alloys [1-5]. Moreover, property characteristics can be readily modified, for example, through the use of post-stretching or by using various matrix alloys, varying fiber-resin systems, and different stacking sequences and cross-piles, although few of these variants are commercially available at present.

ARALL derives its superior crack-growth properties (under tensile loading) by promoting extensive crack bridging in the wake of the crack tip [4-8]. Mechanistically, for crack extension perpendicular to the fiber direction, as the crack propagates in the aluminum layers, controlled delamination between the metal, epoxy and fiber interfaces redistributes stresses both ahead and behind the tip, permitting individual aramid fibers to remain intact and span the crack in the wake of the tip [7,8]. Thus, similar to behavior in certain ceramic-matrix composites [9], the fibers act as bridges to restrain crack opening, thereby reducing the effective "crack driving force" actually experienced at the crack tip. In stretched ARALL Laminates, where the metal layers are left in residual compression and the fibers in residual tension, self-arrest can result with crack extension [10], leading to the claim that ARALL is a "fatigue insensitive" material.

Crack bridging in ARALL Laminates is an example of crack-tip shielding, where toughness is enhanced, or more generally crack advance is impeded, not by increasing the intrinsic microstructural resistance but by mechanisms which act to lower the *local* near-tip "driving force" [11,12]. As illustrated schematically in Fig. 2.2 [11,12], other examples include rubber-toughening in polymers [13], transformation, microcrack and fiber toughening in ceramics [14,15], crack bridging via uncracked ligaments in metals, ceramics and composites [16-18], and crack closure in fatigue [12,19]. In all these cases, the predominant shielding mechanisms act in the crack wake such that, depending upon the extent of the "shielding zone" behind the tip, crack-growth behavior becomes crack-size dependent, i.e., in terms of the globally calculated applied stress intensity K , the usually assumed similitude of the crack-tip fields for cracks of differing size will be compromised. This leads to certain definitive fracture properties, such as marked resistance-curve toughness behavior, as seen for example in toughened ceramics [14,15,17], and the elevated growth rate of small cracks, as seen for near-threshold fatigue in metals [11,20,21].



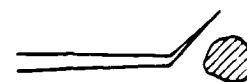
Schematic of ARALL Laminate

XBL 8712-5152

Fig. 2.1: Illustration of the layup of 3/2 ARALL-2 Laminate.

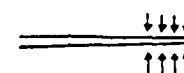
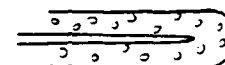
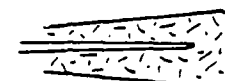
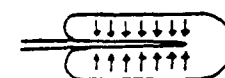
EXTRINSIC TOUGHENING MECHANISMS

1. CRACK DEFLECTION AND MEANDERING



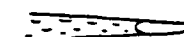
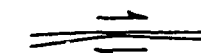
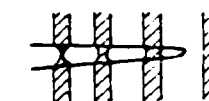
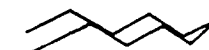
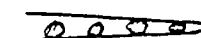
2. ZONE SHIELDING

- transformation toughening
- microcrack toughening
- crack wake plasticity
- crack field void formation
- residual stress fields
- crack tip dislocation shielding



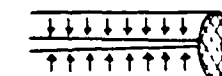
3. CONTACT SHIELDING

- wedging:
 - corrosion debris-induced crack closure
 - crack surface roughness-induced closure
- bridging:
 - ligament or fiber toughening
- sliding:
 - sliding crack surface interference
- wedging + bridging:
 - fluid pressure-induced crack closure



4. COMBINED ZONE AND CONTACT SHIELDING

- plasticity-induced crack closure
- phase transformation-induced closure



XBL 861-7432

Fig. 2.2: Schematic representation of the classes and mechanisms of crack-tip shielding [11,12].

The theoretical modelling of crack-tip shielding is in many cases well developed, particularly for the transformation/microcrack toughening [14,15,22] and crack-bridging mechanisms [7-9,16,17]. There have been few studies, however, to verify experimentally these models and specifically to measure the extent of shielding and the effective near-tip "driving force". An exception to this is crack closure in fatigue where an effective stress-intensity range can be evaluated, for example, in terms of compliance changes resulting from physical contact between the crack surfaces during the unloading cycle [3.g., refs. 11,23,24]. The objective of the present work has been to describe experimental techniques to measure quantitatively the magnitude of crack-tip shielding by crack bridging as well as crack closure in an ARALL Laminate, in order to estimate the effective near-tip stress-intensity range during fatigue crack growth in this material. In addition, the mechanistic characteristics of crack propagation, delamination and crack-bridging behavior in the laminate are described for a wide spectrum of growth rates.

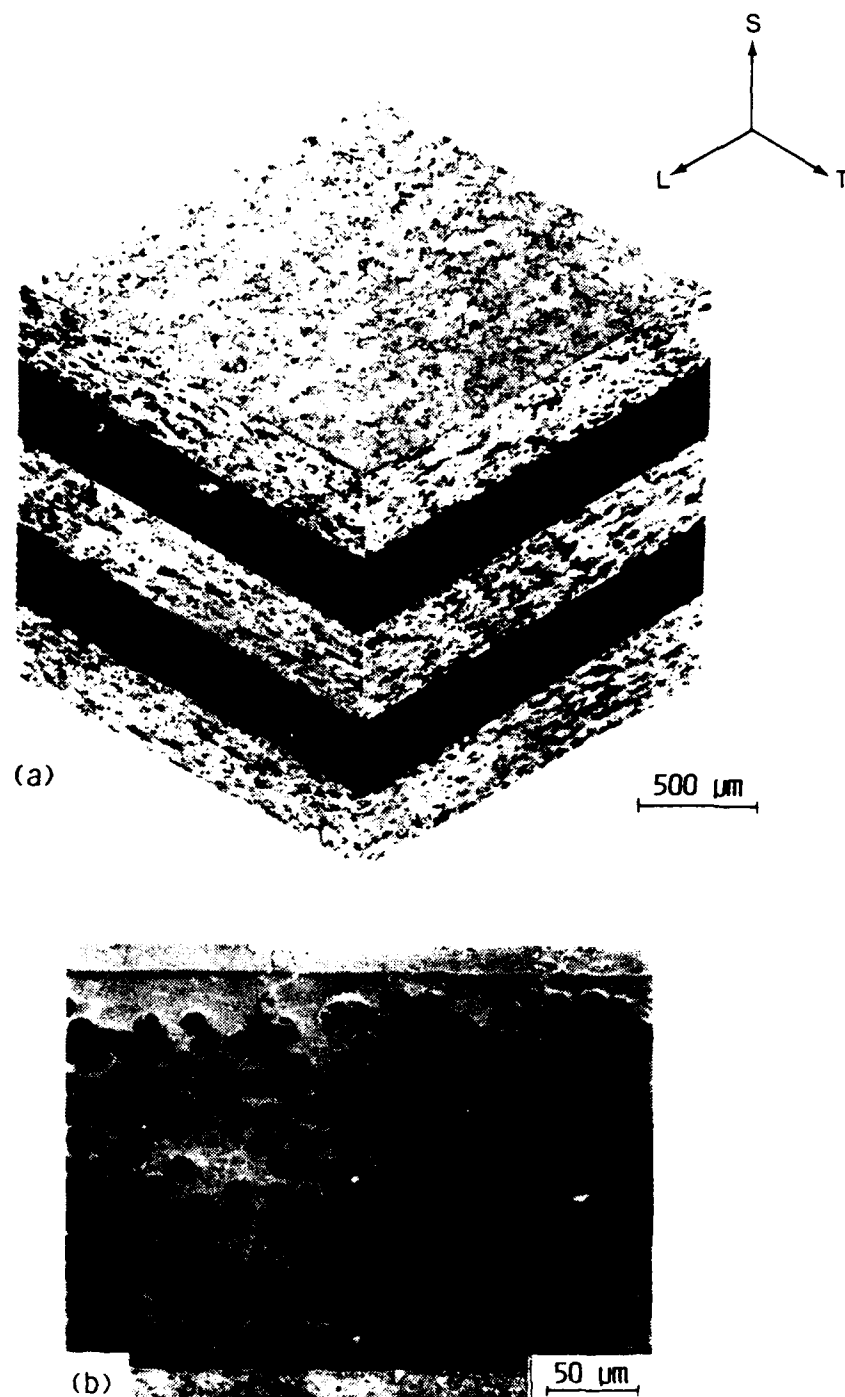
2.2 Experimental Procedures

Materials: The ARALL Laminates used in this study were 1.35-mm-thick five-layer composites with two 0.2-mm-thick unidirectional aramid-fiber/epoxy ("prepreg") layers sandwiched between three 0.3-mm-thick chromic-acid-anodized and primed aluminum-alloy sheets, supplied by Alcoa (Fig. 2.3). The prepreg layers consist of an epoxy based adhesive system impregnated with uniaxial, high-modulus aramid fibers, in a 50/50 fiber/adhesive weight ratio. The fiber direction is aligned parallel to the rolling direction of the aluminum sheet.

The specific ARALL Laminates (3/2 layups) are listed in Table 2.1; corresponding ambient-temperature mechanical properties are given in Table 2.2 [25].

Fatigue Testing: Long-crack (>10 mm) fatigue-crack propagation tests on ARALL Laminates were performed with compact C(T) and center-crack sheet CC(T) test pieces, machined from the full thickness of the plate in the L-T (0°, crack growth perpendicular to fiber direction) and T-L (90°, crack growth parallel to fiber direction) orientations. Comparison tests on 2024-T351 were performed on 7-mm-thick C(T) test pieces, machined in the T-L orientation from the center thickness of 25-mm-thick plate. All testing was carried out in controlled room-temperature air (22°C, 45% relative humidity) using computer-controlled electro-servo-hydraulic testing machines, operating at 50 Hz sinusoidal frequency with a load ratio ($R = K_{min}/K_{max}$) of 0.1.

Crack lengths were monitored using a direct-current electrical-potential technique on the outer aluminum layer (Fig. 2.4). The accuracy of this technique in thin sheet was estimated to be within ± 0.01 mm on crack length. Additionally, the compliance of the specimen was monitored in C(T) specimen using a back-face strain gauge mounted on the central aluminum layer at the midpoint opposite the crack mouth (Fig. 2.4); in CC(T) specimens, conversely, a compliance (clip) gauge was utilized. Both electrical-potential and compliance signals were fed into a real-time computerized data-acquisition and control system, which was used both to control the test and to compute continuously crack-closure loads. The latter effect of crack closure was defined in terms of a closure stress intensity, K_{cl} , measured at the point of first contact of the



XBB 8712-10279

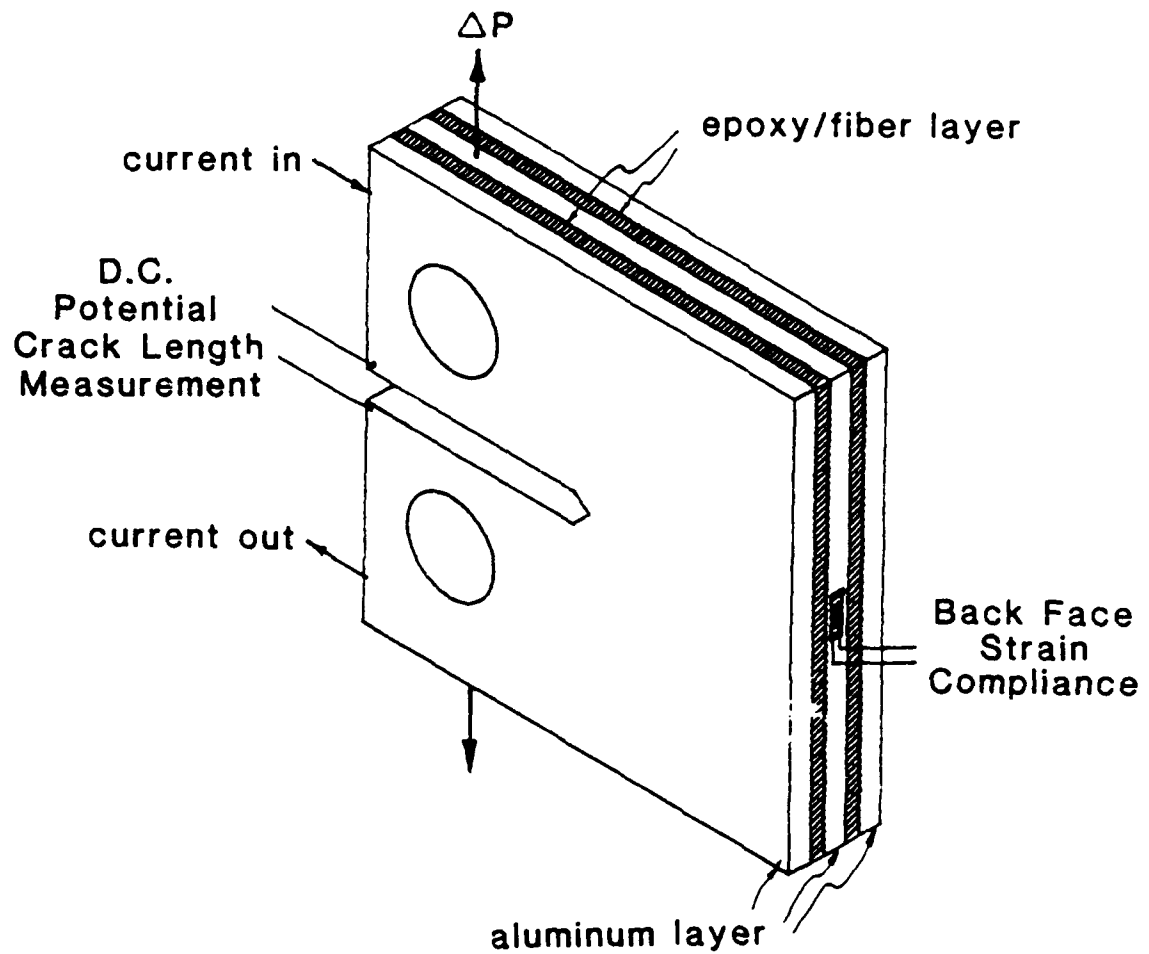
Fig. 2.3: Optical micrographs of a) three-dimensional microstructure of ARALL-2, and b) cross-section showing prepreg layers sandwiched between aluminum layers. Note in b) the resin-rich (fiber-poor) regions close to the prepreg/aluminum interfaces.

Table 2.1
ARALL Laminate Commercial Product Forms

Description	Characteristics
ARALL-1 Laminate Alloy 7075-T6 120°C cure prepreg 0.5% permanent stretch	Superior fatigue High Strength
ARALL-2 Laminate Alloy 2024-T3 120°C cure prepreg with or without 0.4% stretch	Excellent fatigue Increased formability Damage tolerant
ARALL-3 Laminate Alloy 7075-T76 120°C cure prepreg 0.4% permanent stretch	Superior fatigue Controlled toughness Good exfoliation High strength
ARALL-4 Laminate Alloy 2024-T8 175°C cure prepreg with or without 0.4% stretch	Excellent fatigue Elevated temperature

Table 2.2
Ambient-Temperature Mechanical Properties of ARALL Laminates (3/2)

Alloy		Yield Strength		UTS	Elastic Modulus		Strain to Failure
		Tensile (MPa)	Compressive (MPa)		Tensile (GPa)	Compressive (GPa)	
ARALL-1	L	655	365	772	64.1	70.3	1.7
	T	324	379	379	49.0	51.7	7.8
ARALL-2	L	359	262	717	64.1	64.8	2.5
	T	228	234	317	49.0	51.7	12.7
ARALL-3	L	589	-	827	68.0	-	2.2
	T	317	-	372	51.0	-	-
ARALL-4	L	374	-	732	61.4	-	2.6
	T	316	-	336	49.0	-	4.6



XBL 8712-5153

Fig. 2.4: Illustration of the fatigue test specimen showing the location of the electrical-potential crack monitoring probes, attached to the outer aluminum layer, and the back-face strain gauge used to measure compliance, attached to the central aluminum layer.

crack surfaces on unloading. Stress intensities were calculated from standard handbook solutions [26] for both the C(T) and CC(T) geometries, using the full thickness of the composite.

The crack-propagation tests were performed under computer control with a constant stress-intensity gradient, in general accordance with ASTM Standard E 647-86A. Data were first generated under decreasing ΔK conditions using an automated load-shedding scheme of $\Delta K = \Delta K_0 \exp[C(a - a_0)]$, where ΔK and a are the instantaneous values of stress-intensity range ($K_{\max} - K_{\min}$) and crack length, ΔK_0 and a_0 are their initial values, and C is the normalized stress-intensity gradient set to -0.1 per mm of crack extension. Following crack arrest at a "threshold" condition, tests were continued under increasing ΔK conditions, with C set to 0.15 mm^{-1} . Using these procedures, crack-propagation rate data were generated over a wide spectrum of growth rates, from roughly 10^{-11} to 10^{-5} m/cycle. Data are presented both in terms of the nominal (applied) stress-intensity range ($\Delta K = K_{\max} - K_{\min}$) and an effective (near-tip) stress-intensity range ($\Delta K_{\text{eff}} = K_{\max} - K_{\text{cl}}$), which accounts for the shielding effect from crack closure.

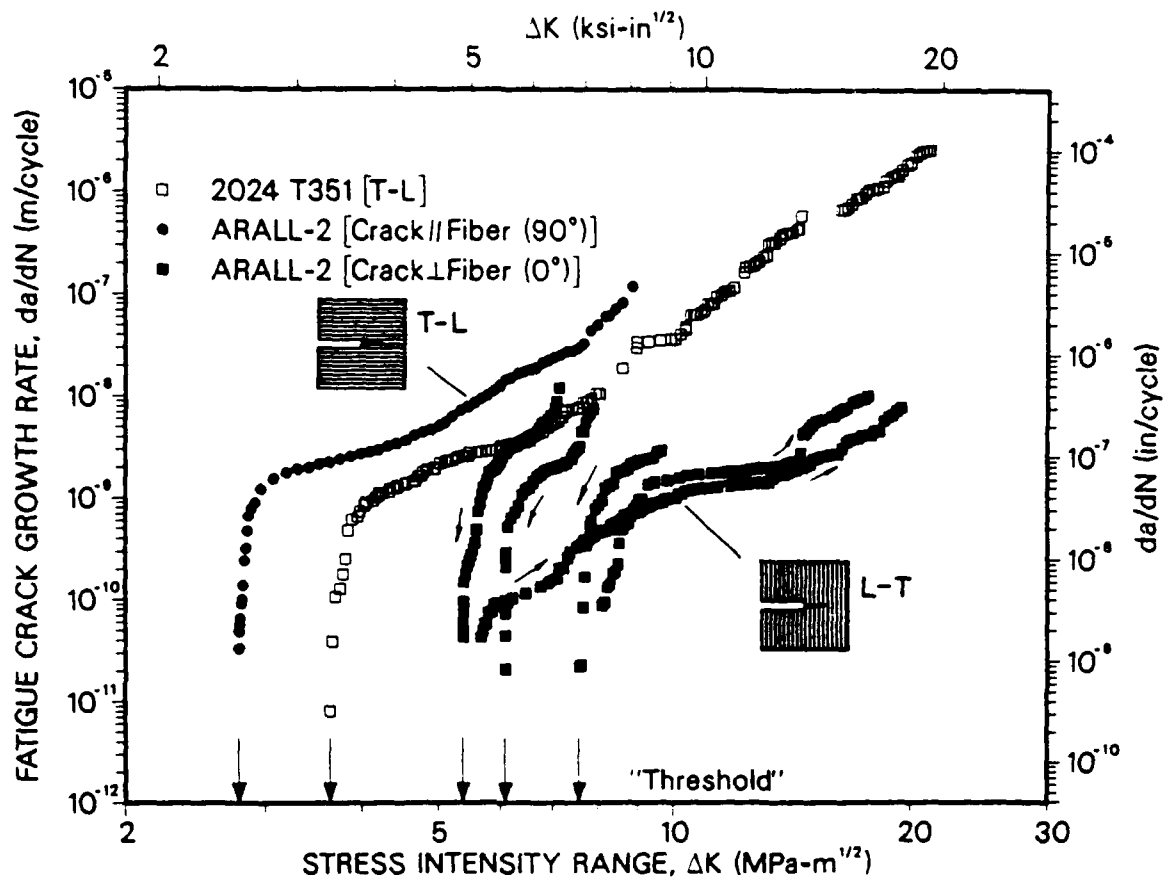
2.3 RESULTS AND DISCUSSION

Fatigue Crack Growth Behavior: Results of the constant-amplitude fatigue-crack propagation tests, in the form of growth rates, da/dN , as a function of the nominal stress-intensity range, ΔK , are shown in Fig. 2.5 for the 0° (L-T) and 90° (T-L) orientations in ARALL-2 Laminate; data are compared to that for monolithic 2024-T351 (T-L orientation).

Where fatigue-crack propagation in the laminate is along the fiber direction (90° orientation), growth rates are faster than in the monolithic alloy, although the form of the growth-rate curve is similar. If the ARALL data for this orientation are normalized with respect to the actual total thickness of the aluminum in the composite, i.e., assume that the aluminum carries all load, crack growth rates for ARALL-2 (90°) coincide with those for the monolithic 2024-T351 alloy (Fig. 2.6). This result implies that the role of the fibers (and the resin) in the laminate can be ignored for crack growth in the transverse (90°) direction.

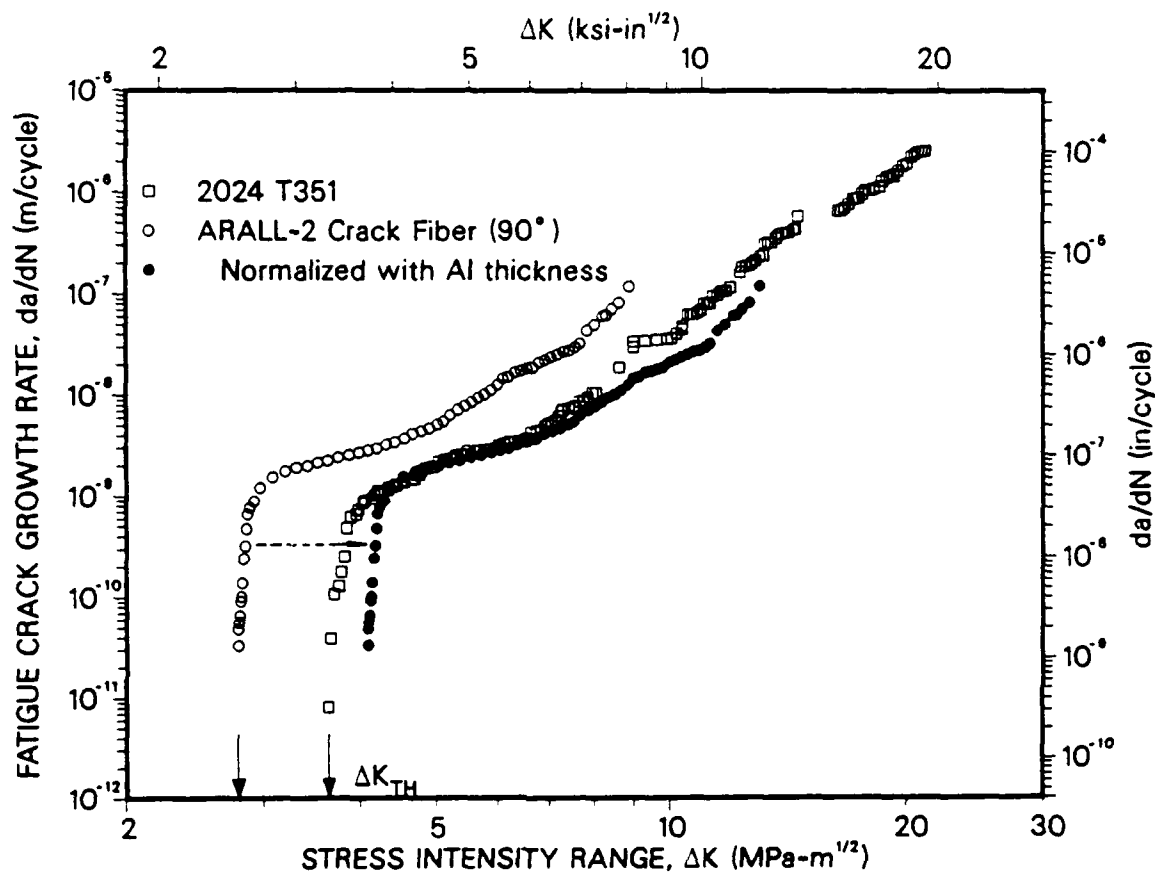
Conversely, where fatigue crack propagation in the laminate is perpendicular to the fiber direction (0° orientation), due to the contribution of the aramid fibers, behavior is quite different from 2024-T351. Firstly, growth rates in the laminate are in general significantly slower (by up to almost three orders of magnitude) than in the monolithic aluminum alloy, indicating that the fatigue crack growth resistance of ARALL-2 in this orientation is extremely high. Secondly, similar to behavior reported for other ARALL laminates [1-8,10,27], crack growth rates become non-unique with respect to the nominal stress-intensity range ΔK , showing a marked history and crack-size dependence.

Fractographic Studies: The reinforcement role of the fibers during crack growth in the latter longitudinal (0°) orientation was examined using scanning electron



XBL 8712-5154

Fig. 2.5: Variation in fatigue crack propagation rates (da/dN) for ARALL-2 Laminate, as a function of the nominal stress-intensity range ($\Delta K = K_{max} - K_{min}$), in the longitudinal (0° , L-T) and transverse (90° , T-L) orientations. Data are compared with results for monolithic 2024-T351 alloy (T-L orientation). Vertical arrows show the effective fatigue "thresholds", i.e., the values of ΔK at crack arrest. Small arrows on curves indicate whether data were obtained under decreasing or increasing growth-rate conditions.



XBL 8712-5155

Fig. 2.6: Variation in fatigue crack propagation rates (da/dN) as a function of the nominal stress-intensity range (ΔK) for ARALL-2 and 2024-T351 alloy in the transverse (T-L) orientation, showing the correspondence of growth-rate behavior in the laminate and the monolithic alloy by assuming that the aluminum layers carry all the load in ARALL-2.

microscopy of metallographic sections taken across the crack perpendicular to the crack surface. Figure 2.7 shows one such cross-section, located ~3 mm from the crack tip, looking into the crack in the crack propagation direction, i.e., from the wake toward the tip. The fatigue crack can be readily seen in the aluminum layers, but is also still visible in the epoxy layer. Numerous strands of aramid fibers, however, remain unbroken across the crack.

To lower the probability of fiber breakage necessary to permit such crack bridging, some degree of controlled delamination is essential to reduce the magnitude of fiber loading and lower through-thickness constraint [8]. Claims that such delamination occurs principally within the epoxy near the prepreg/metal interface, specifically at the boundary between the fiber-rich and resin-rich layers [6-8], have been made. However, the fact that the crack can be imaged throughout the thickness of the epoxy layer (Figs. 2.7 and 2.8) suggests an alternative explanation. In the present case, the interface between the aluminum sheet and the epoxy, and between the resin-rich and fiber-rich layers within the epoxy, only suffered minor delamination, whereas extensive separation was apparent among various bundles of fibers, implying that failure of individual fiber/epoxy interfaces is the primary source of the delamination process.

Figure 2.7 also shows evidence of "bulged out" fibers at the crack line, which suggests some degree of prior kinking. Fiber kinking is known to be severely detrimental to the fatigue properties of ARALL as it promotes breakage of the aramid fibers [27]; for this reason ARALL laminates are intended for tension-dominated cyclic loading application, and as such are not suited for high compressive loading during service. However, such kinking in the present study is probably the result of the predominantly bending stress field implicit with compact test piece which, unlike center-cracked tension geometries, subjects fibers located well ahead of the crack tip (below the neutral axis) to prior compressive loads. Crack growth behavior in ARALL is thus predicted to be geometry-dependent.

Another example of geometry-dependent behavior is apparent at high stress-intensity ranges, where the marked difference in crack propagation resistance between the 0° and 90° orientations (due to selective fiber bridging) leads to a tendency for crack growth in the 0° direction to deviate along the fiber direction in compact C(T) geometries. This phenomenon causes marked crack bifurcation, as shown in Fig. 2.8, which results in additional crack-tip shielding by crack deflection at high ΔK . However, in center-cracked tension CC(T) sheet geometries, where off-angle crack propagation is not stabilized, such crack-bifurcation behavior is rarely observed.

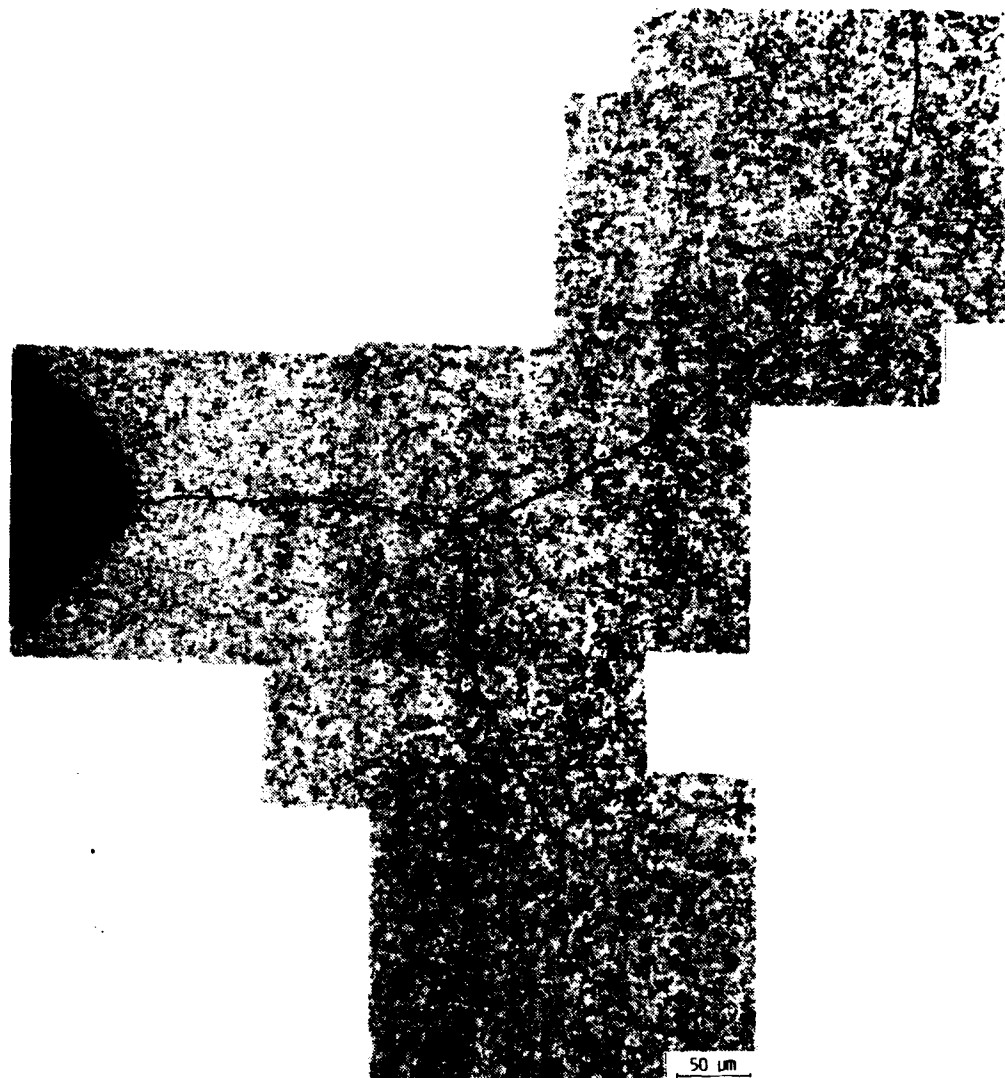
Measurement of Crack-Bridging Zone: In order to verify further the role of fiber bridging influencing fatigue crack propagation behavior in ARALL, and specifically to determine the location and size of the "bridging zone" of unbroken fibers behind the crack tip (Fig. 2.9), experiments were performed where the wake of the crack was progressively removed while simultaneously monitoring the change in elastic compliance (as a measure of how much the fibers restrain crack opening).

The experiment was conducted on an arrested crack that had been cycled for 10^7 cycles at an apparent threshold of $\Delta K = 7.6 \text{ MPa}\sqrt{\text{m}}$, following normal load-



XBB 8712-10280

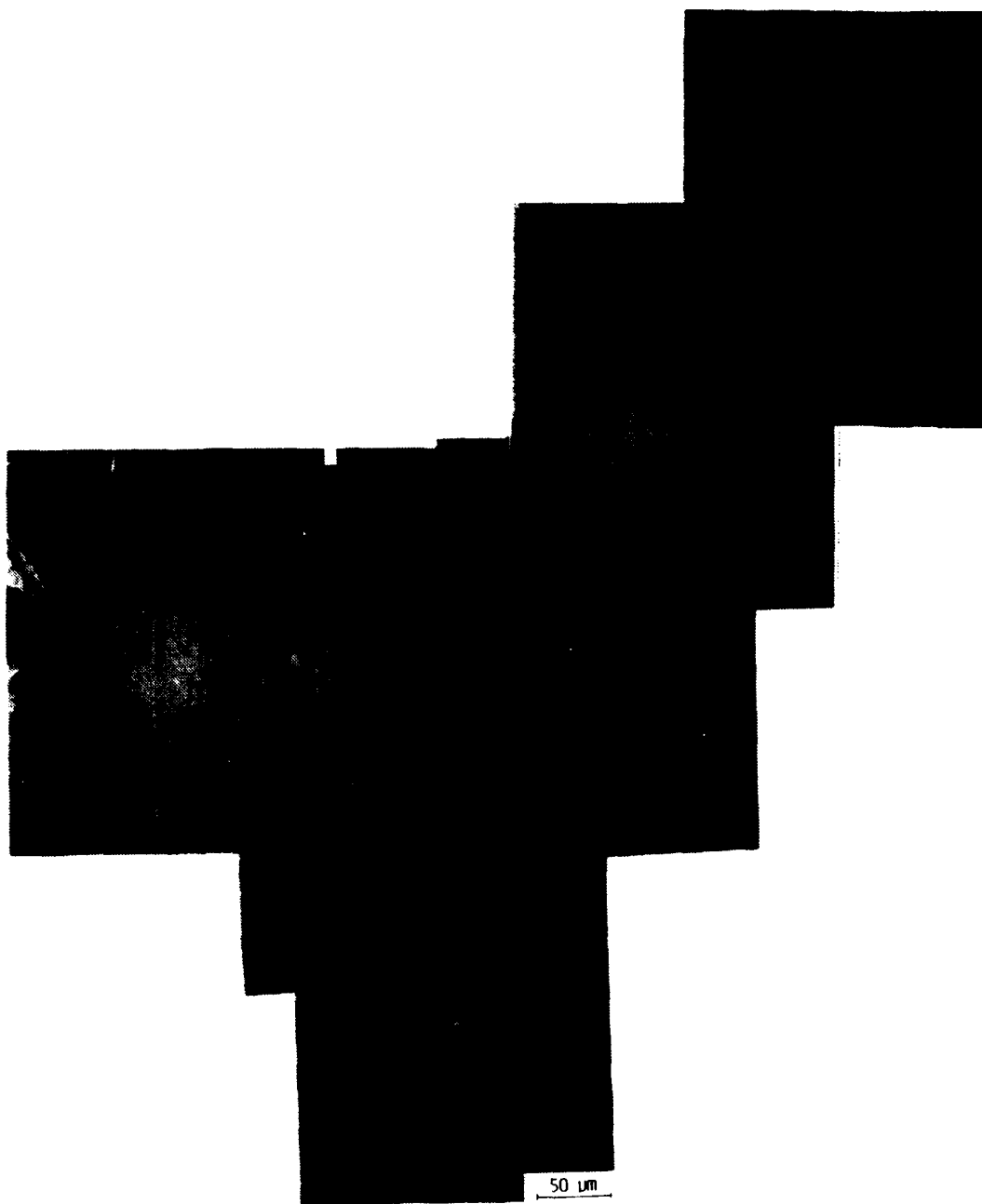
Fig. 2.7: Scanning electron micrograph of a metallographic section taken across the wake of a fatigue crack in ARALL-2 (imaged ~3 mm from the crack tip, looking into the crack mouth toward the tip), showing numerous strands of unbroken aramid fibers bridging the crack. Note that the crack is still visible in the epoxy layer, indicating that the delamination is primarily at individual fiber/epoxy interfaces.



(a)

X3B 8712-10277

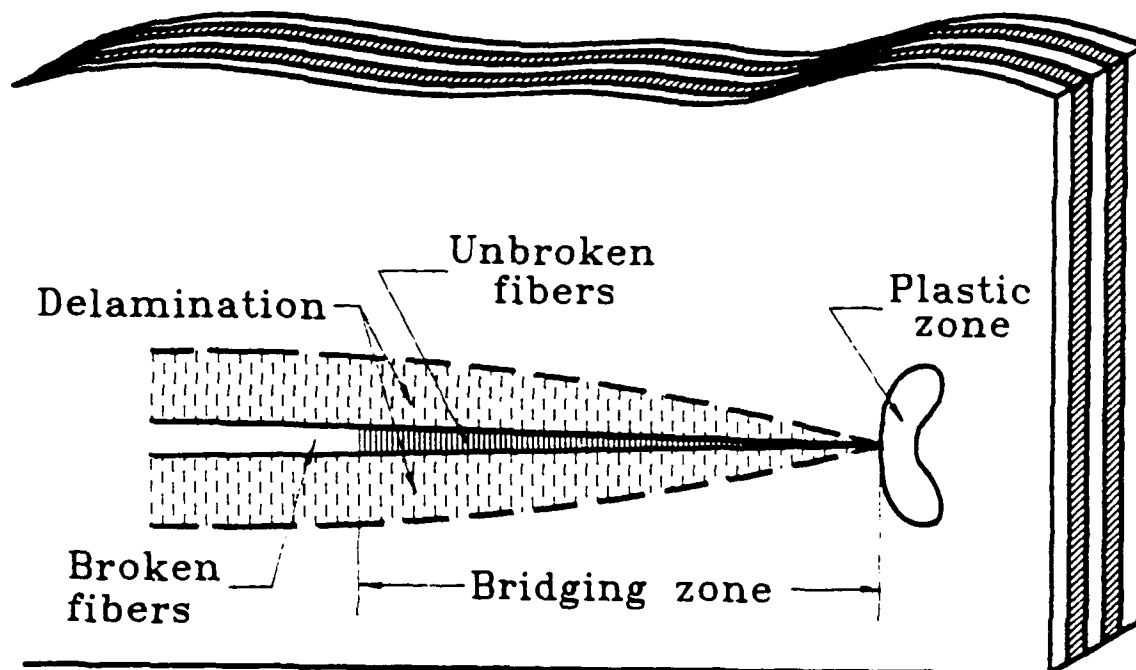
Fig. 2.8: Metallographic section perpendicular to the crack plane showing crack bifurcation during fatigue crack propagation at high stress-intensity ranges ($\Delta K \sim 15 \text{ MPa}\sqrt{\text{m}}$) in ARALL-2, as imaged a) in the outer aluminum layer, and b) in the epoxy layer after etching away the aluminum. Note that as the crack is still visible within the epoxy layer, the principal delamination is not at the resin-rich/fiber-rich boundary.



(b)

XBB 8712-10278

Fig. 2.8(b)



XBL 8712-5210

Fig. 2.9: Schematic illustration of a fatigue crack in ARALL, showing the location of the bridging (or shielding) zone.

shedding procedures. Using a fine jeweler's saw, a 1-mm-wide slot was machined from the V-notch along the dormant crack to within ~ 0.2 mm of the crack tip. Approximately every 1 mm, the elastic compliance was measured using the back-face strain gauge mounted on the central aluminum layer (Fig. 2.4), while monitoring the length (\tilde{a}) of the remaining portion of the crack with a traveling microscope; results are plotted in Fig. 2.10a. For the ~ 26 -mm-long crack, removing the wake to within roughly 5 mm of the crack tip had little effect on the compliance, implying that the fibers were broken this far from the tip. Conversely, the compliance increased sharply as the last ~ 5 mm of wake were removed, indicating that the fibers in this region were originally intact across the fatigue crack and were being severed by the jeweler's saw.

Such measurements suggest a shielding (or bridging) zone in ARALL of the order of 5 mm behind the crack tip where the principal fiber bridging takes place. Compared to the size of this zone for other mechanisms of shielding in Fig. 2.2, this is extremely large. For example, similar wake-machining experiments in monolithic aluminum alloys to determine the extent of crack closure (primarily from asperity wedging) in the wake of arrested cracks suggest shielding-zone sizes closer to $500\text{ }\mu\text{m}$ [28,29]. Furthermore, in the case of corrosion-debris induced crack closure, where the fretting oxide deposits accumulate only very close to the tip [30,31], the shielding zone may be less than $\sim 10\text{ }\mu\text{m}$. Since the magnitude of the shielding zone behind the crack tip primarily dictates the history- and crack-size dependence of the crack-growth behavior, such results are consistent with the experimental observations (Fig. 2.5) that longitudinal growth rates in ARALL do not display a unique dependence upon ΔK .

To examine the re-generation of the bridging zone with crack extension, following wake machining the remaining 0.2-mm fatigue crack, emanating from the machined slot, was cycled at the original "threshold" ΔK level of $7.6\text{ MPa}\sqrt{\text{m}}$. As shown in Fig. 2.10b, although the crack commenced to propagate immediately on application of the cyclic load, growth rates progressively decayed with subsequent crack extension (at constant ΔK) until the crack re-arrested after more than 10^8 cycles. The crack length needed for re-arrest, i.e., to re-establish a bridging zone behind the crack tip, can be seen to be of the order of 3 mm, somewhat less than the 5 mm or so required for arrest during load shedding (Fig. 2.10a). Such differences presumably reflect different loading histories prior to arrest, namely decreasing ΔK conditions during programmed load shedding compared to constant ΔK conditions (at the lowest "threshold" level) in the above experiment.

Measurement of Crack-Tip Shielding: Whereas the fatigue crack propagation properties of ARALL Laminates in the longitudinal (0°) orientation are clearly excellent, from the perspective of analysis and prediction of crack extension and lifetime, the non-uniqueness of the crack growth data (in terms of ΔK) is far from ideal. As noted above, such non-uniqueness, with respect to crack size, geometry and loading history, results from differing degrees of crack bridging in the wake of the crack (and associated delamination), which reduces the effective ΔK experienced locally at the crack tip. Although modelled by Marissen [7,8] for the center-cracked tension geometry, there have been no attempts experimentally to measure the bridging effect, in order to determine an effective ΔK which would suitably characterize the crack-tip fields in ARALL and thus potentially normalize the longitudinal crack growth data.

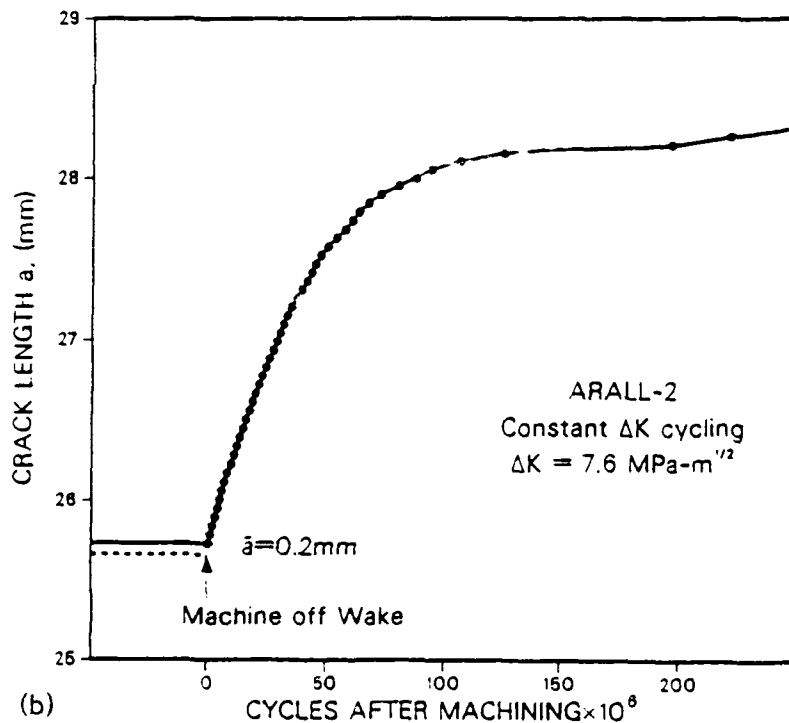
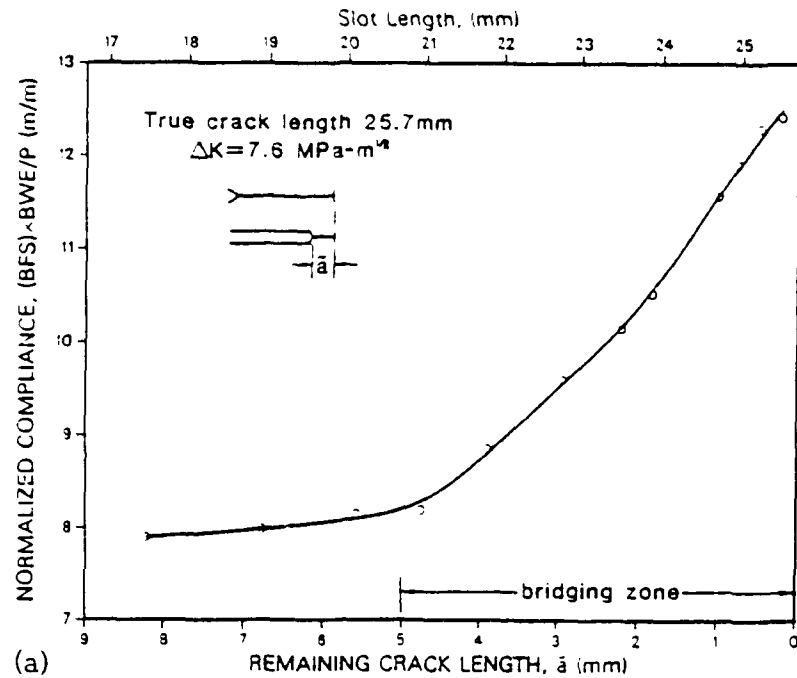


Fig. 2.10: Results of experiments to estimate the size of the bridging zone in ARALL showing a) the change in compliance as a function of the remaining length of fatigue crack, \bar{a} , during progressive removal of the crack wake, and b) the initial acceleration and subsequent progressive deceleration of crack growth from the machined slot (initial $\bar{a} = 0.2 \text{ mm}$). All results were determined at a constant ΔK of $7.6 \text{ MPa} \cdot \text{m}^{1/2}$, where prior to machining the crack had arrested.

Below we describe an experimental scheme, intended to provide this characterization through the measurement of the effect of crack-tip shielding from both crack bridging and crack closure using combined electrical-potential and compliance monitoring.

Principle: The principle of the measurement technique is illustrated schematically in Fig. 2.11. Shielding is assumed to affect the applied "crack driving force", $\Delta K = K_{\max} - K_{\min}$, in two ways, specifically by crack closure (i.e., wedging through crack-surface contact), which primarily increases the effective K_{\min} , and crack bridging, which primarily decreases the effective K_{\max} . Accordingly, the effective stress-intensity experienced at the tip may be defined as:

$$\Delta K_{\text{eff}} = K_{\text{br}} - K_{\text{cl}}, \quad (2.1)$$

where K_{br} is the effective K_{\max} (corrected for crack bridging) and K_{cl} is the effective K_{\min} (corrected for crack closure). Experimental techniques to measure each parameter are described below.

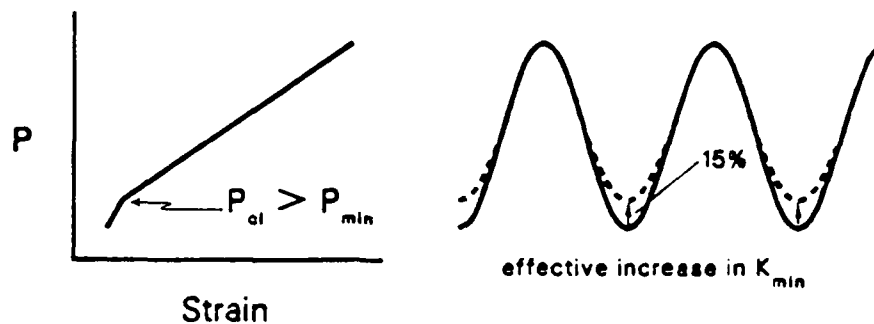
Crack closure: In aluminum alloys at low ΔK levels, the principal source of crack closure arises from wedging of crack surfaces by fracture-surface asperities (roughness-induced closure), aided by that induced by cyclic plasticity in the wake of the crack tip [e.g., refs. 29,33]. Accordingly, the closure stress intensity K_{cl} is generally measured at the point of first contact of the crack surfaces during an unloading cycle [e.g., refs. 11,24]. In the present study, this was achieved by monitoring the elastic unloading compliance derived from the back-face strain gauge. Specifically, the data-acquisition and control system was programmed to determine, using a maximum correlation-coefficient procedure [11], the K_{cl} value in real time in terms of the highest load where the elastic unloading compliance curve deviated from linearity (Fig. 2.11).

Using such procedures, closure levels in ARALL were found to be comparable with those in monolithic 2024-T351 sheet, but due to the higher ΔK levels required for propagation, their effect was proportionally smaller. In fact, closure was clearly of secondary importance to crack bridging in governing the value of ΔK_{eff} (see below). Specifically, closure levels were enhanced with decreasing ΔK , as wedging is more effective at smaller crack opening displacements (CODs), but never resulted in more than a 15% increase in the effective K_{\min} .

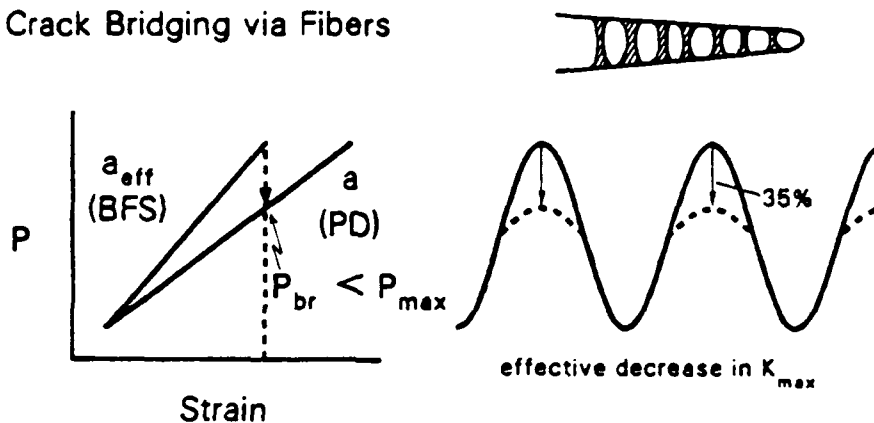
*It should be noted here that in the general case, crack closure, induced by cyclic plasticity [23] or fluid pressure [32] for example, may have a small additional influence in reducing the effective K_{\max} . By the same token, depending upon the mechanical properties of the fibers, crack bridging may influence the effective K_{\min} . However, the proposed measurements are not specific to the microstructural origins of the shielding mechanisms and will thus evaluate the total effect.

Crack Tip Shielding Mechanisms

1. Wedging via Crack Closure (fracture surface asperities)



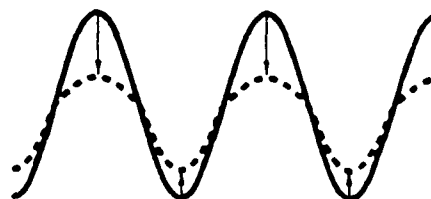
2. Crack Bridging via Fibers



3. Total Shielding

$$\text{from } \Delta K = K_{max} - K_{min}$$

$$\text{to } \Delta K_{eff} = K_{br} - K_{cl}$$



XBL 8712-5158

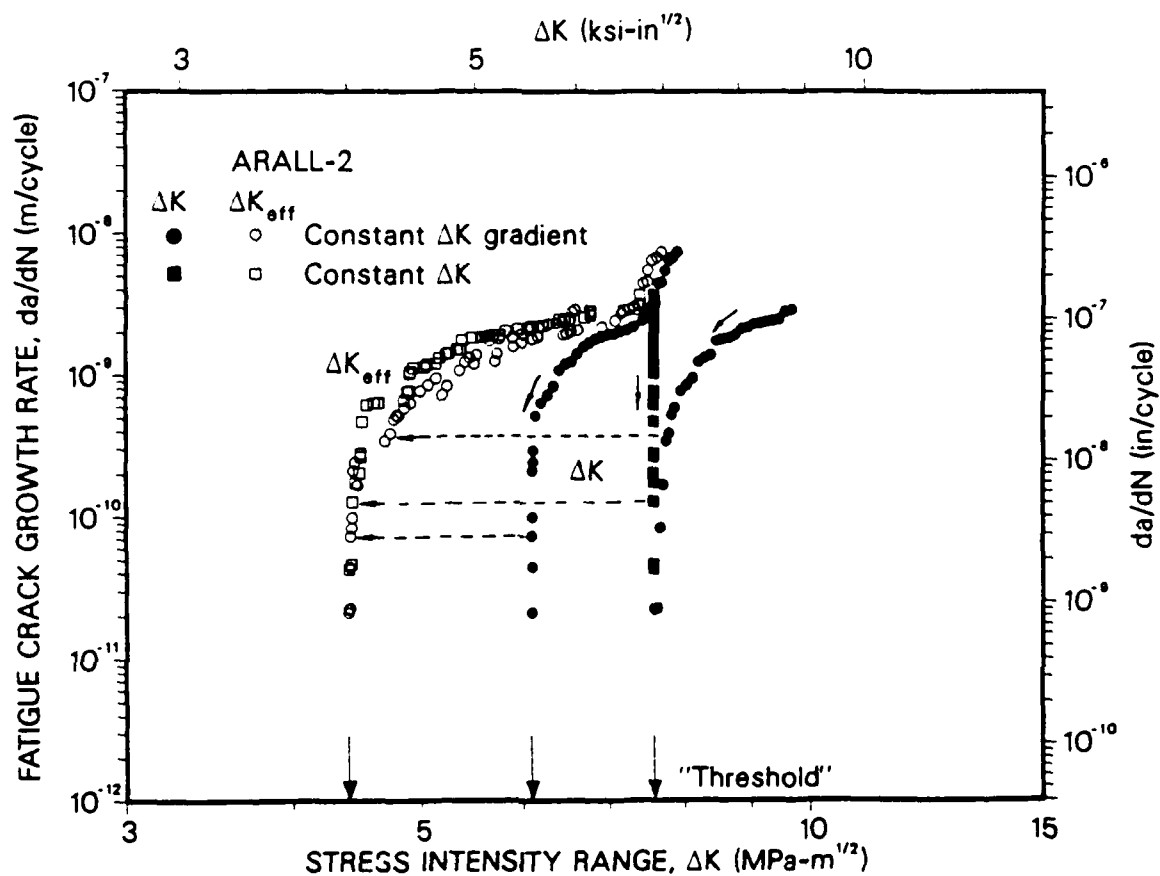
Fig. 2.11: Schematic illustrations of the primary crack-tip shielding mechanisms in ARALL, namely crack bridging and crack closure, and the experimental techniques used to quantify their effect on the effective near-tip "crack-driving force", i.e., $\Delta K_{eff} = K_{br} - K_{cl}$.

Crack bridging: The effect of crack bridging on the effective K_{max} value was estimated using a new technique which combines measurement of the actual length of the full crack, using electrical-potential methods on the outer aluminum layer, with measurement of the compliance of the bridged crack, using back-face strain gauges on the central aluminum layer (Fig. 2.4).

For each cycle, an elastic compliance curve of measured back-face strain vs. load P was determined; the slope of this curve (ignoring non-linearities due to closure at very low loads) represents the compliance of the bridged crack. Simultaneously, electrical-potential measurements were used to estimate the true length of the crack and, using an experimentally verified compliance calibration for back-face strain in the C(T) geometry [34-37], the theoretical compliance curve for the full-length (unbridged) crack was computed. As illustrated in Fig. 2.11, the slopes of these two curves are different. The experimental curve, derived from back-face strain measurements, is steeper (implying a smaller effective crack size) because the compliance is reduced by the fiber bridges; the theoretical curve, computed from electrical measurements of the true crack length, conversely is insensitive to the bridging effect.* Thus, at a given load, the measured strain (representative of the actual crack opening displacement) can be seen to be less than that predicted from the true (unbridged) crack length, because of the restraint on crack opening by the unbroken fibers. On this basis, the reduction in effective K_{max} due to bridging can be estimated by comparing these two curves at a given strain, for example, representative of the actual COD at maximum load. As shown in Fig. 2.11, the measured load (P_{max}) acting on the bridged crack length is clearly larger than that predicted (P_{br}) for the true (unbridged) crack length; the difference is essentially the load carried by the bridges. Accordingly, values of P_{br} can be used to compute the approximate magnitude of K_{br} as the effective maximum stress intensity in the fatigue cycle (after correcting for bridging).

With such procedures, the measured effect of crack bridging in ARALL was found to be far greater than that due to crack closure, resulting in up to 35% reductions in effective K_{max} values in the fatigue cycle. The success of this approach may be judged with reference to Fig. 2.12 where, by using both closure and bridging corrections for shielding to compute ΔK_{eff} values from Eq. 2.1, the fatigue crack propagation data for ARALL-2 in the longitudinal (0°) orientation from Fig. 2.5, and from Fig. 2.10b for crack growth at constant ΔK from the wake-machined notch, are replotted in terms of ΔK_{eff} . Once the allowance is made for both closure and bridging in the computation of the appropriate "crack driving force", crack propagation behavior in the laminate is no longer dependent upon history and crack size, and is a unique function of ΔK_{eff} . (Results of the highest ΔK levels are not plotted in Fig. 2.12 as they involve macroscopic crack bifurcation and thus are not amenable to this simple analysis).

* In ARALL Laminates, the fiber bridges are non-conducting and thus do not compromise the electrical-potential measurements of true crack size. In materials where the bridges are conducting, or conversely where the matrix is non-conducting, actual crack size measurements can still be made by monitoring the electrical resistance of a thin metal film, either evaporated or affixed to the side face of the specimen [37].



XBL 8712-5159

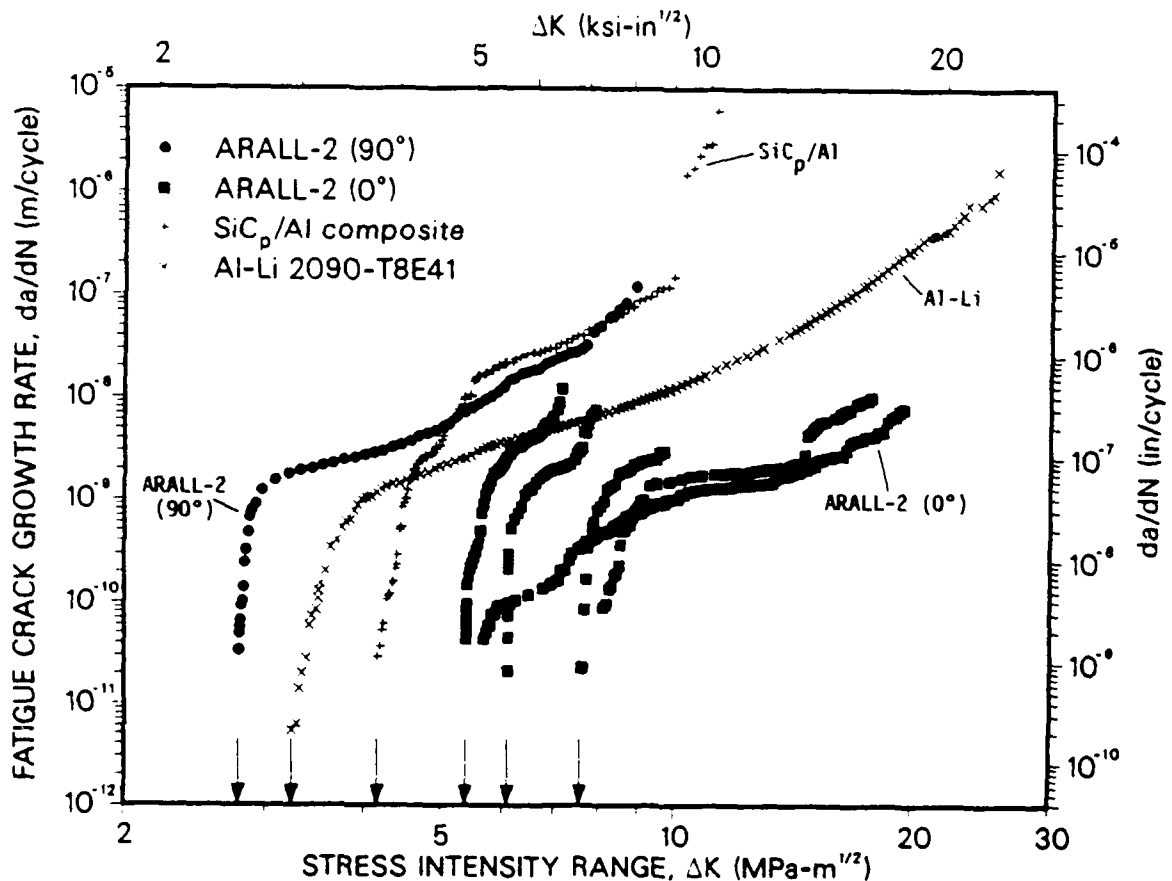
Fig. 2.12: Fatigue crack propagation results for ARALL-2 in the longitudinal (0°) orientation (from Figs. 2.5 and 2.10), plotted as a function of the nominal ($\Delta K = K_{max} - K_{min}$) and effective ($\Delta K_{eff} = K_{br} - K_{cl}$) stress-intensity ranges. Note how characterization in terms of ΔK_{eff} normalizes the previously crack-size and history dependent growth-rate data (horizontal dashed arrows). Small arrows on curves indicate whether data were obtained under decreasing or increasing growth-rate conditions.

Comparison with Advanced Aluminum Alloys: From the perspective of high-performance applications, ARALL Laminates must compete with other advanced aluminum alloys, and in particular with aluminum-lithium alloys and metal-matrix composites. A comparison of the fatigue crack growth performance of these materials at ambient temperatures is shown in Fig. 2.13., based on the current ARALL-2 data and published results (at $R = 0.1$) for a commercial aluminum-lithium alloy 2090-T8E41 [38] and a SiC-particulate reinforced P/M Al-9%Zn-3%Mg-2½%Cu (ALCOA MB78) alloy [18]. The fatigue crack growth resistance of ARALL-2 in the transverse (90°) orientation is inferior to that of the other alloys; however, in the longitudinal (0°) orientation where cracks propagate perpendicular to the fiber direction, the laminate is superior to the metal-matrix composite, and furthermore shows significantly improved crack growth properties over the aluminum-lithium alloy. Since the 2090-T8E41 alloy may be considered as having (long-crack) fatigue properties superior to most, if not all, high-strength monolithic aluminum alloys, the use of ARALL for unidirectionally loaded, fatigue-critical structures provides a clear potential for markedly improved durability and damage-tolerance.

2.4 Conclusions

Based on an experimental study of fatigue crack propagation and crack-tip shielding behavior in a 2024-T351 aluminum-alloy/aramid-fiber epoxy 3/2 laminated composite, ARALL-2 Laminate, the following conclusions can be made:

1. Over the range of growth rates from $\sim 10^{-11}$ to 10^{-5} m/cycle (at $R = 0.1$), rates of fatigue crack propagation in ARALL-2 were found to be far slower than in the constituent matrix alloy 2024-T351 for crack advance perpendicular to the fiber direction (0° or longitudinal orientation); rates parallel to the fiber direction (90° or transverse orientation), conversely, were typically a factor of 4 faster.
2. Whereas differences in the growth-rate behavior between ARALL-2 and monolithic 2024-T351 can be predicted in the transverse (90°) orientation by assuming that the fibers play no role and that the aluminum-alloy layers carry all load, the superior crack-growth resistance of the laminate in the longitudinal (0°) orientation is associated with crack-tip shielding primarily by crack bridging from unbroken aramid fibers in the wake of the crack tip, with smaller contributions from crack closure and bifurcation.
3. The occurrence of crack bridging by unbroken fibers was promoted by controlled delamination, principally along the fiber/epoxy interfaces. Using wake-removal experiments, the length of crack over which the fibers remained unbroken in the wake of the crack tip, i.e., the bridging zone, was found to be between 3 to 5 mm, far larger than shielding zones measured for other mechanisms of shielding.
4. Owing to such extensive shielding from crack bridging, fatigue crack growth rates in the longitudinal (0°) orientation were crack-size and history dependent and showed no unique correlation with the applied stress-intensity range ΔK .



XBL 8712-5160

Fig. 2.13: Comparison of the fatigue crack propagation behavior of ARALL-2 (0° and 90° orientations), as a function of ΔK at $R = 0.1$, with other advanced aluminum alloys, namely aluminum-lithium alloy 2090-T8E41 and SiC-particulate reinforced P/M Al-9%Zn-3%Mg-2%Cu (ALCOA MB78) metal-matrix composite. Data for 2090 and SiC_p/Al composite taken from refs 38 and 18, respectively.

5. A new experimental procedure, involving both electrical-potential and back-face strain compliance monitoring, is presented to enable the measurement of the reduction in effective K_{max} in the fatigue cycle due to crack bridging. Coupled with standard unloading compliance measurements of the increase in effective K_{min} due to crack closure, an effective (near-tip) stress-intensity range, ΔK_{eff} , can be derived which embodies the effect of both crack bridging and closure. When characterized in terms of this local field parameter, longitudinal crack growth rates in ARALL lose their crack-size and history dependence and become a unique function of ΔK_{eff} .

6. Under tension-tension fatigue loading, ARALL-2 Laminates display inferior crack-propagation resistance in the transverse (90°) orientation, and superior fatigue crack-propagation resistance in the longitudinal (0°) orientation, compared to monolithic aluminum and SiC-particulate reinforced aluminum alloys.

2.5 References

1. J. Schijve and L. B. Vogelesang, "Development of ARALL, a New Material for Aircraft Structures," Memorandum M-434, Delft Univ. of Technology, Dept. of Aerospace Engineering, Sept. 1982.
2. L. B. Vogelesang and J. W. Gunnink, "ARALL, a Material for the Next Generation of Aircraft. A State of Art," Report LR-400, Delft Univ. of Technology, Dept. of Aerospace Engineering, Aug. 1983.
3. L. N. Mueller, J. L. Prohaska, and J. W. Davis, in Proc. AIAA Aerospace Eng. Conf., AIAA, Los Angeles, Ca, 1985.
4. L. B. Vogelesang and J. W. Gunnick, Materials and Design, 7 (1986) p. 2.
5. R. Marissen, Eng. Fract. Mech., 19 (1984) p. 261.
6. R. Marissen, K. H. Trautmann, J. Foth, and H. Nowack, in Fatigue 84, Proc. 2nd Intl. Conf. on Fatigue and Fatigue Thresholds, C. J. Beevers, ed., vol. II, IMAS Ltd., Warley, U.K., 1984, p. 1081.
7. R. Marissen, "Fatigue Crack Growth in Aramid Reinforced Aluminum Laminates (ARALL), Mechanisms and Predictions," Report DFVLR-FB-84-37, DFVLR, Institut fur Werkstoff-Forschung, 1984.
8. R. Marissen, in Fatigue 87, Proc. 3rd Intl. Conf. on Fatigue and Fatigue Thresholds, R. O. Ritchie and E. A. Starke, eds., vol. 3, EMAS Ltd., Warley, U.K., 1987, p. 1271.
9. D. B. Marshall, B. N. Cox, and A. G. Evans, Acta Metall., 33 (1985) p. 2013.
10. R. J. Bucci, L. N. Mueller, R. W. Schultz, and J. L. Prohaska, in Advanced Materials Technology 87, Proc. 32nd Intl. SAMPE Symp., Sci. of Adv. Matls. and Proc. Eng., vol. 32, 1987, p. 902.
11. R. O. Ritchie and W. Yu, in Small Fatigue Cracks, R. O. Ritchie and J. Lankford, eds., TMS-AIME, Warrendale, PA, 1986, p. 167.

12. R. O. Ritchie, in Mechanical Behavior of Materials - V, Proc. 5th Intl. ICM Conf., M. G. Yan, S. H. Zhang, and Z. M. Zheng, eds., vol. 2, Pergamon Press, Oxford, U.K., 1988, p. 1399.
13. A. G. Evans, Z. B. Ahmad, D. G. Gilbert, and P. W. R. Beaumont, Acta Metall., 34 (1986) p. 79.
14. A. G. Evans and R. M. Cannon, Acta Metall., 34 (1986) p. 761.
15. A. G. Evans and K. T. Faber, J. Am. Ceram. Soc., 67 (1974) p. 250.
16. A. R. Rosenfield and B. S. Majumdar, Metall. Trans. A, 18A (1987) p. 1053.
17. Y.-W. Mai and B. R. Lawn, J. Am. Ceram. Soc., 70 (1987) p. 289.
18. J.-K. Shang, W. Yu, and R. O. Ritchie, Mater. Sci. Eng. A, 102A (1988) p. 181.
19. S. Suresh and R. O. Ritchie, in Fatigue Crack Growth Threshold Concepts, D. L. Davidson and S. Suresh, eds., TMS-AIME, Warrendale, PA, 1984, p. 227.
20. S. Suresh and R. O. Ritchie, Intl. Metals. Rev., 29 (1981) p. 445.
21. J. Lankford, Fatigue Fract. Engng. Mater. Struct., 8 (1985) p. 161.
22. J. W. Hutchinson, Acta Metall., 35 (1987) p. 1065.
23. W. Elber, in Damage Tolerance in Aircraft Structures, ASTM STP 486, American Society for Testing and Materials, Philadelphia, PA, 1971, p. 230.
24. J. E. Allison, in Fracture Mechanics 18th Symposium, ASTM STP 945, R. P. Read and D. T. Reed, eds., American Society for Testing and Materials, Philadelphia, PA, 1987, p. 913.
25. M. A. Gregory, "ARAL": 1, 2, 3 and 4 Laminates. Preliminary Technical Information," Alcoa Technical Report, Aluminum Company of America, Alcoa Center, PA, 1987.
26. H. Tada, P. C. Paris, and G. R. Irwin, The Stress Analysis of Cracks Handbook (2nd edition), Paris Productions/Del Research Corp., St. Louis, MO, 1985.
27. F. E. H. M. Smulders and G. H. J. J. Roebroeks, "Mechanism of Prepreg Failure Under R = 0 Fatigue Loading in ARALL Laminate," Technical Report, Delft University of Technology, Dept. of Aerospace Engineering, 1987.
28. K. Minakawa, J. C. Newman, and A. J. McEvily, Fatigue Engng. Mater. Struct., 6 (1983) p. 359.
29. E. Zaiken and R. O. Ritchie, Metall. Trans. A, 16A (1985) p. 1467.
30. S. Suresh, D. M. Parks, and R. O. Ritchie, in Fatigue Thresholds, Proc. 1st Intl. Conf. on Fatigue Thresholds, J. Bäcklund, A. F. Blom, and C. J. Beevers, eds., vol. I, EMAS Ltd., Warley, U.K., 1982, p.391.
31. S. Suresh and R. O. Ritchie, Scripta Metall., 17 (1983) p. 575.

32. J.-L. Tzou, C. H. Hseuh, A. G. Evans, and R. O. Ritchie, Acta Metall., 33 (1985) p. 117.
33. R. D. Carter, E. W. Lee, E. A. Starke, and C. J. Beevers, Metall. Trans. A, 15A (1984) p. 555.
34. W. F. Deans and C. E. Richards, J. Test. Eval., 7 (1979) p. 147.
35. C. E. Richards and W. F. Deans, in The Measurement of Crack Length and Shape during Fracture and Fatigue, C. J. Beevers, ed., EMAS Ltd., Warley, U.K., 1980, p. 28.
36. D. C. Maxwell, "Strain-based Compliance Method for Determining Crack Length for a C(T) Specimen," Materials Laboratory, Air Force Wright Aeronautical Laboratories, Report No. AFWAL-RT-87-4046, Wright-Patterson Air Force Base, Dayton, OH, 1987.
37. P. K. Liaw, H. R. Hartmann, and W. A. Logsdon, J. Test. Eval., 11 (1983) p. 202.
38. K. T. Venkateswara Rao, W. Yu, and R. O. Ritchie, Eng. Fract. Mech., 31 (1988) p. 623.

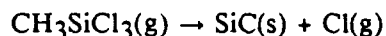
3. FATIGUE-CRACK PROPAGATION STUDIES IN CONTINUOUSLY-REINFORCED METAL-MATRIX COMPOSITES

3.1 Introduction

The mechanisms affecting fatigue-crack growth and crack-tip shielding in continuously-reinforced metal-matrix composites, specifically with 40% unidirectional SCS-8 (SiC) fibers in a 6061 aluminum-alloy matrix, were examined in this project. The composites, which were supplied by Lockheed, were fabricated from 8 layers of 140- μm -diameter fibers, plasma sprayed with 6061 and diffusion bonded together. The resulting 1.5 mm-thick sheet was annealed for 2 hr at 430°C, and slow cooled at 30°C/hr to 100°C.

3.2 Material

The microstructure of the composite is shown in Fig. 3.1. The SiC fiber is produced via chemical vapor deposition of Si onto a carbon filament (Fig. 3.2), according to the following reaction at 1300°C:



resulting in a β -SiC fiber with a carbon rich core. Fig. 3.3, supplied by Textron Speciality Materials who manufacture the fiber, shows the approximate composition of the fiber in the radial direction. The outermost layer consists of a carbon rich coating about 1 μm thick, then a layer of fine-grained β -SiC. The carbon layer is applied before application of the aluminum alloy.

3.3 Microstructural Study

Specimen Preparation: Thin samples of the composite were cut in various orientations, and mechanically ground to a $\frac{1}{2}$ μm finish, before being mounted on a copper grid with silver epoxy and cured at 90°C for 1 hr. Specimens were then dimpled and polished to 20 μm using a VCR D500 dimpler, and then ion milled with a Gatan 600A cold stage mill at 4.5 kV.

Scanning Electron Microscopy: Fig. 3.4 shows the secondary electron, compositional and topographic images of the metal-matrix composite. In the compositional image (Fig. 3.4b), topographical information is suppressed, such that elements with low atomic number appear darker. Thus, the C core, SiC coating and aluminum matrix appear progressively lighter. The core itself has a 32 μm diameter; the second compositional ring of C-rich SiC extends ~ 15 μm from the core.

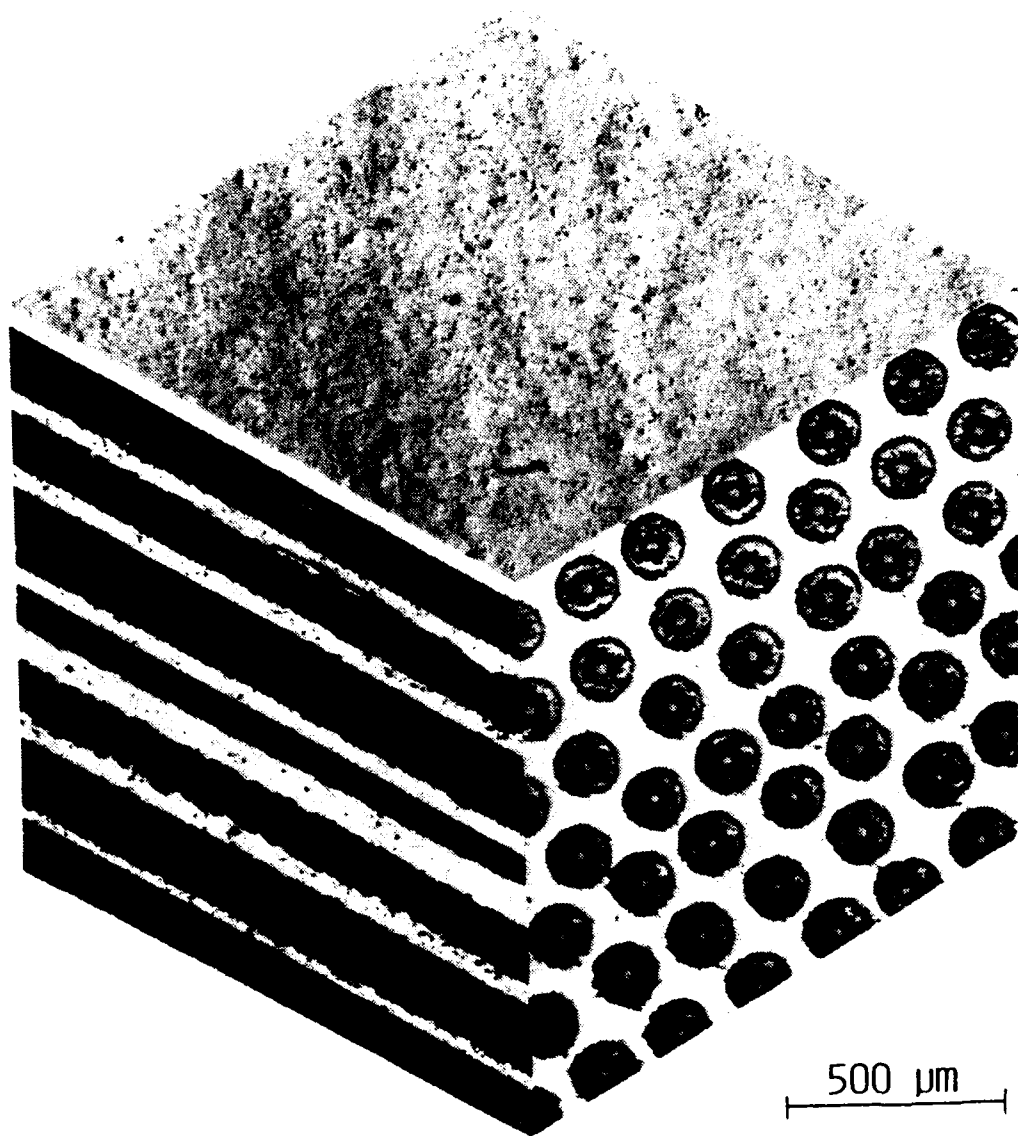


Fig. 3.1: Three dimensional optical micrograph of SiC_f continuous reinforced 6061 metal matrix composites. Fiber diameter is $140\text{ }\mu\text{m}$.

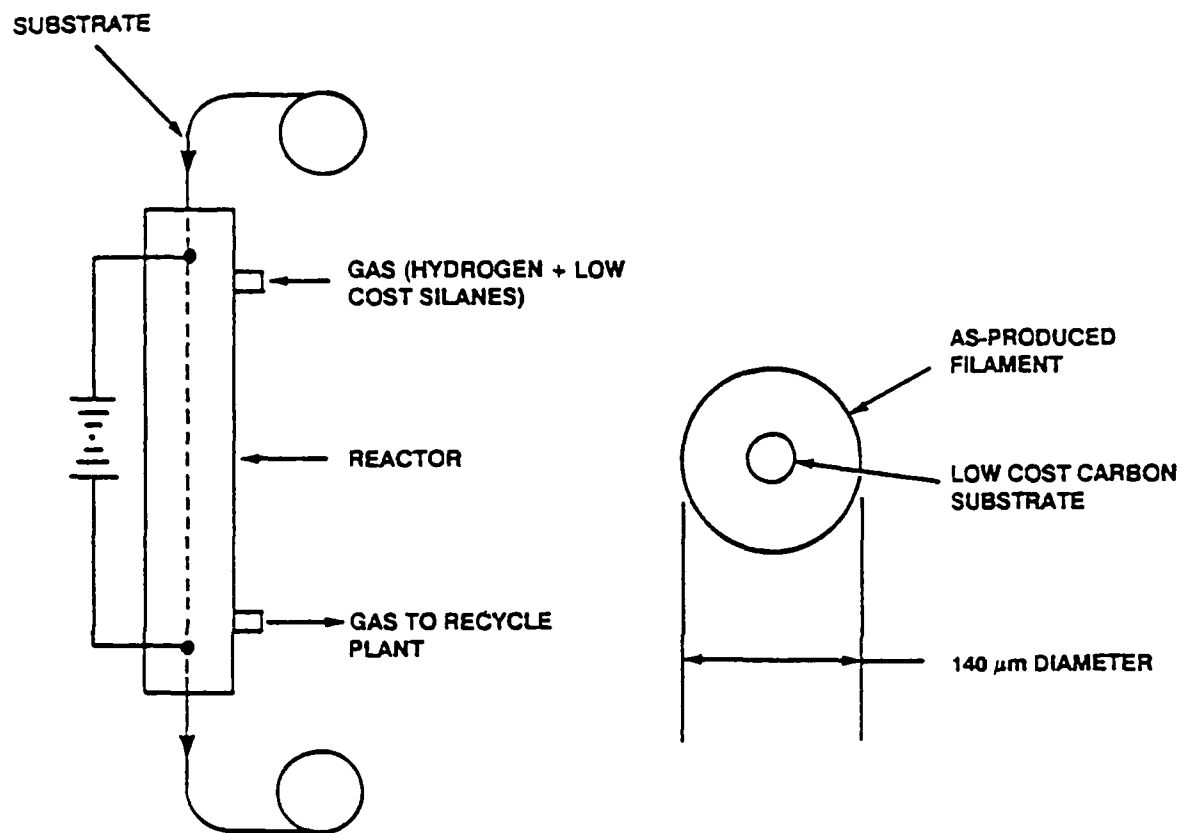


Fig. 3.2: Schematic of fabrication of silicon carbide fiber.

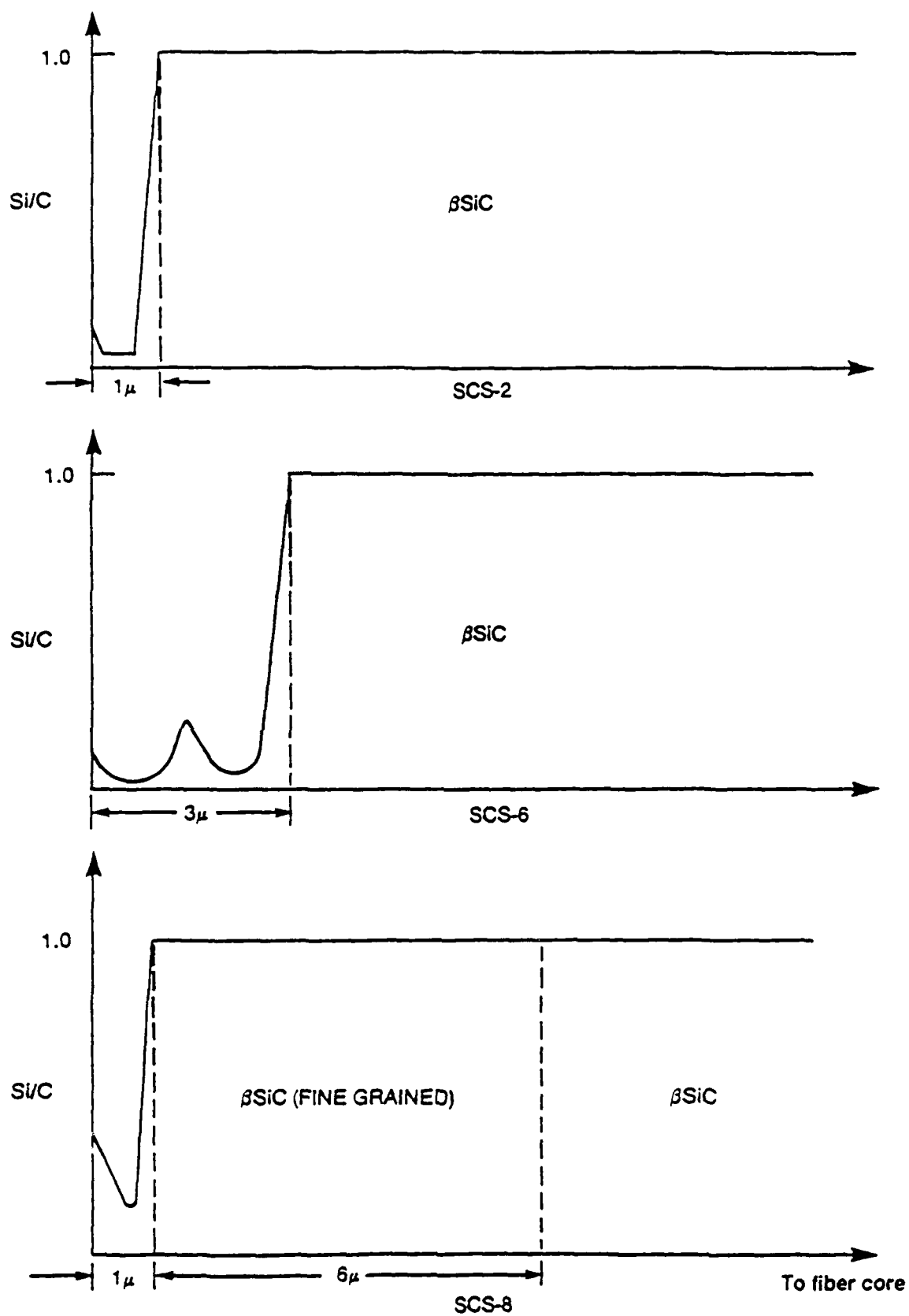


Fig. 3.3: Schematic of surface region compositions of AVCO silicon carbide.

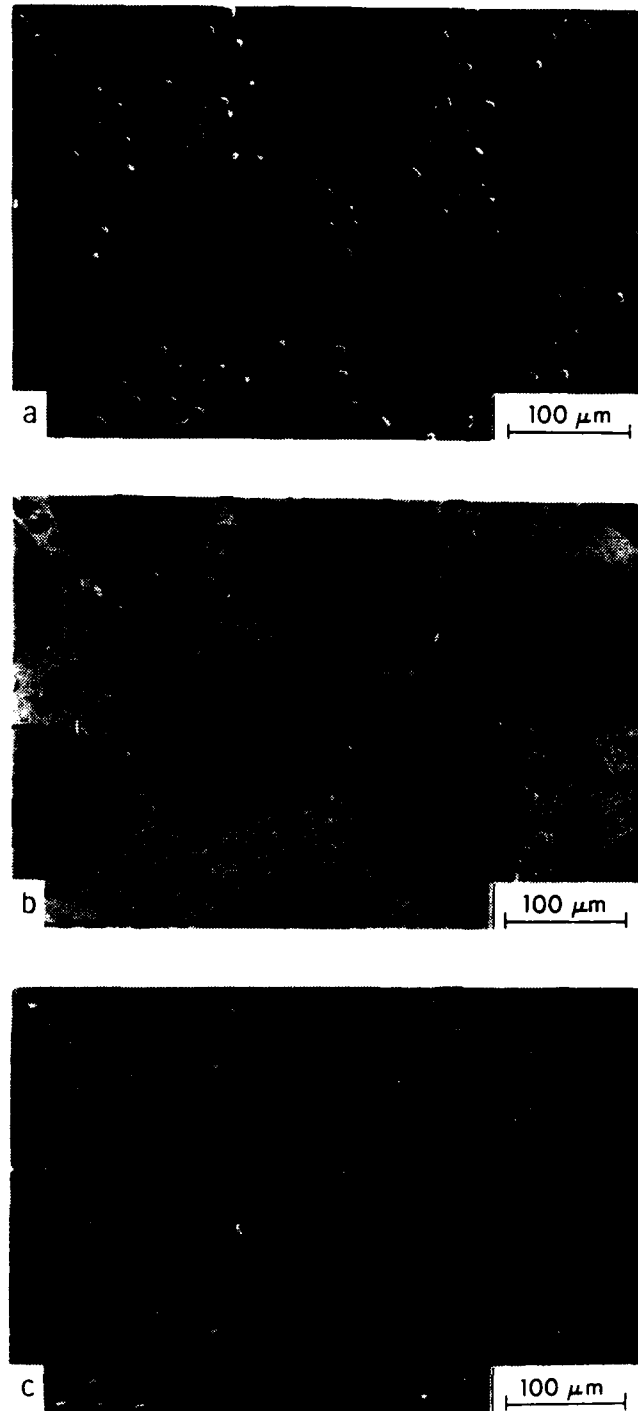


Fig. 3.4: a) Secondary, b) composition, and c) topographical SEM images of 6061/SiC_f composite at 25 keV. In the composition image the lighter elements appear dark, and the heavier elements appear light, e.g., carbon appears as black, SiC as dark gray, and alum. um as light gray. Note the large number of carbon particles scattered throughout the aluminum matrix. These particles are probably the result of poor processing technique.

Surrounding the fibers, 5 to 20 μm sized carbon particles are in evidence, presumably formed as a result of poor processing techniques. These are shown in Fig. 3.5, together with a closer view of the fiber/matrix interface.

Transmission Electron Microscopy Study: Shown in Fig. 3.6 is the β -SiC fiber, as imaged in a Phillips 301 transmission electron microscope (TEM). The fine needle-like grains, roughly 0.05 to 0.3 μm wide and $>28 \mu\text{m}$ long, are aligned radially outward in the fiber. Within each grain, there are numerous parallel dark lines, indicating the presence of microtwins and stacking faults [1]. Fig. 3.7 shows an image of the fiber/matrix interface; the bright area is the fiber carbon coating.

The high dislocation density in aluminum matrix at the fiber/matrix interface and the absence of voids indicate strong bonding between fiber and matrix. Because of differences in thermal expansion between the fiber and matrix, thermal stresses develop on cooling after fabrication. With weak interfacial bonding, void nucleation would result in the interface as the matrix pulls away from the fiber; with strong bonding, conversely, the matrix cannot separate and thus thermal stresses are relieved by the generation of dislocations. Dislocation densities at Al-SiC interface can be very high ($10^9 - 10^{10} \text{ cm}^{-2}$), which contributes to the high overall strength of the composite [2]. In the present study, dislocation densities surrounding the SiC fibers are estimated to be of the order of $5 \times 10^9 \text{ cm}^{-2}$.

Clearly, the strong interface between the matrix and fiber is associated with the good wettability of SiC by aluminum [3]. Flom and Arsenault [2] have determined a lower bound value for the strength of this Al-SiC bond from tensile tests on a 6061 alloy reinforced with 1 vol.% SiC particulate; local stresses during plastic deformation under a triaxial stress state were calculated resulting in a lower bound bond strength of 1690 MPa. These authors concluded that where limited debonding did occur in these composites, it was probably the result of defects generated during fabrication [2].

The formation of the brittle Al_4C_3 phase was not observed in the present alloy; it is believed that the presence of free Si in the aluminum matrix inhibits the formation of this phase [3-4].

3.4 Uniaxial Tensile Properties

Uniaxial tensile tests, with 12.7-mm gauge length, were performed in the 0° (longitudinal) and 90° (transverse) orientations; results are summarized in Table 3.1. For comparison, literature values for the composite and the constituent matrix and fiber materials are listed in Table 3.2.

It is apparent that although the composite shows a five-fold increase in strength and a three-fold increase in stiffness in the 0° orientation (i.e., with the applied load parallel to the fibers) compared to the monolithic aluminum alloy, its strength properties in the 90° orientation are severely degraded (e.g., the tensile strength in the transverse orientation is less than a third of the unreinforced material).

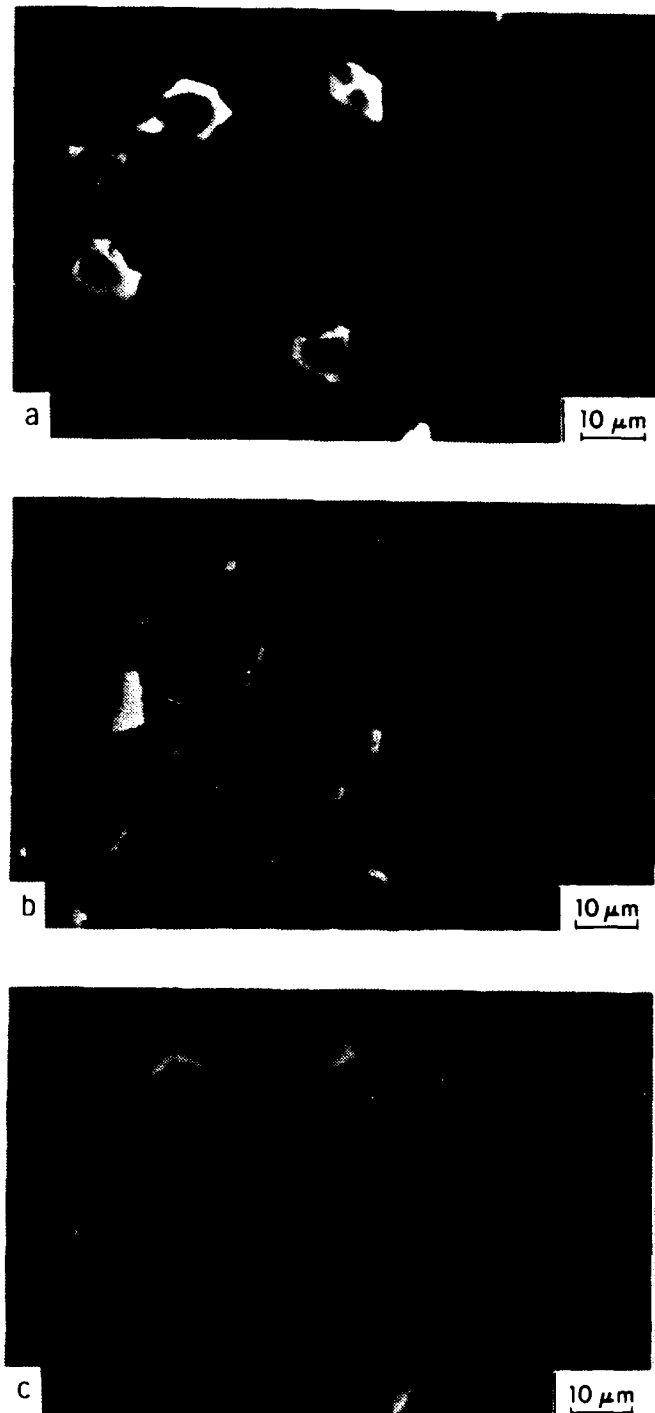


Fig. 3.5: a) Secondary, b) composition, and c) topographical SEM images of 6061/SiC_f composite at 25 keV. A closeup view of the 6061/SiC_f composite shows a high carbon content interface about 1.0 μm thick. Carbon particles in the matrix are about 10 μm in diameter. The white colored particles seen in the composition image are iron precipitates.



Fig. 3.6: Bright field TEM image of SiC fiber at 100 keV. Note the directional fine needle-like grains. Microtwins and fine dislocations can be seen within each grain.

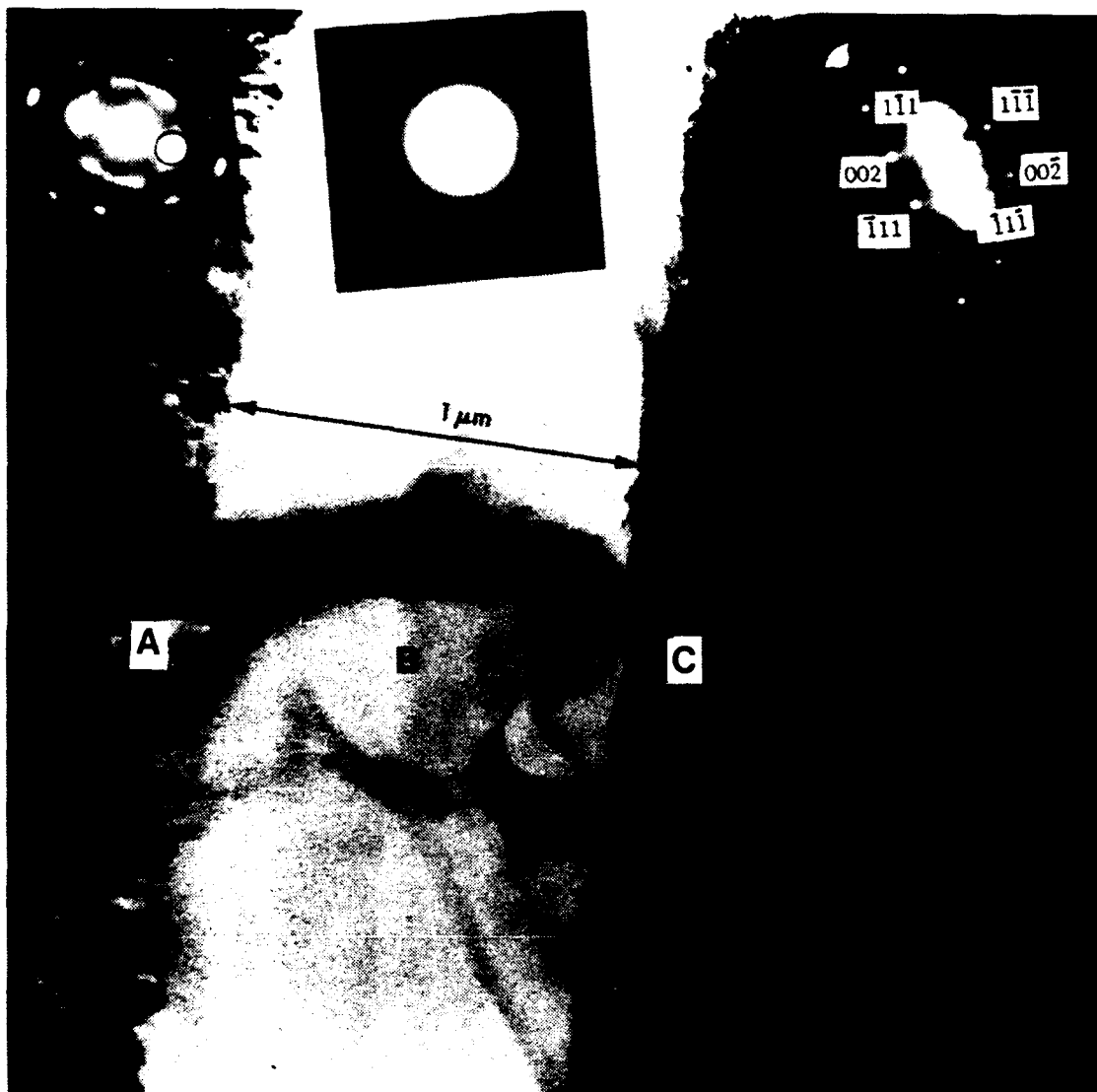


Fig. 3.7: Bright field TEM image of fiber/matrix interface at 100 keV. Selected area diffraction patterns taken from each area are shown. Area A is the SiC fiber, area B is the carbon rich interface, and area C is the aluminum matrix.

Table 3.1
Experimental Uniaxial Tensile Properties of Al/SiC_f Composite

Orientation	Tensile Strength (MPa)	Young's Modulus (GPa)	Strain to Failure (% on 12.7 mm gauge)
0° (L)	1492.0	220	0.84
90° (T)	83.5	106	4.13

Table 3.2
Literature Uniaxial Tensile Properties of Al/SiC_f Composites and their Constituents

Material	Tensile Strength (MPa)	Young's Modulus (GPa)	Strain to Failure (%)	Reference
Composite-0°	1462	204	0.89	[5]
Composite-90°	86	118	-	[5]
6061-T6 matrix	290	69	10.0	[6]
SCS-2 SiC fiber	4000	400	-	[5]

The variation in tensile properties of the composite with orientation shown above can be rationalized using the simple rule of mixtures concept [7]. For the 0° orientation, where applied loads are parallel to the fiber direction, the stresses in the fiber (σ_f) and matrix (σ_m) can be considered to be additive:

$$\sigma_c^l = v_f \cdot \sigma_f^l + (1 - v_f)\sigma_m \quad , \quad (3.1)$$

where σ_c is the stress in the composite, v_f is the volume fraction of fibers, and the superscript l refers to the longitudinal orientation; therefore, the elastic modulus of the composite (E_c) in this orientation is given in terms of the moduli of the fiber and matrix, E_f and E_m , respectively:

$$E_c^l = v_f \cdot E_f^l + (1 - v_f) \cdot E_m \quad . \quad (3.2)$$

For the 90° orientation, conversely, the strains are additive; the modulus in this orientation is given by:

$$1/E_c^t = v_f/E_f^t + (1 - v_f)/E_m \quad , \quad (3.3)$$

where the superscript t refers to the transverse orientation. Using these simple relationships, the elastic modulus for both 0° and 90° orientations can be calculated to within 10% of the experimentally measured values.

The fracture surfaces of the tensile specimens of the composite show matrix failure by microvoid coalescence, and fiber failure by transgranular cleavage (Fig. 3.8). In both 0° and 90° orientations, the aluminum matrix is found to adhere to the fiber; in fact areas of fiber/matrix separation are rare. Evidence for fiber pullout is clearly apparent in the 0° orientation (Fig. 3.9); in the 90° orientation, conversely, failure occurs primarily through the matrix with some fiber cleavage both near the specimen surface and in the middle of the specimen gauge (Fig. 3.10). Cleavage of fibers near the surface, however, is probably accentuated by the high stress concentrations generated from electric discharge machining (EDM) damage.

3.5 Fatigue-Crack Propagation Behavior

Experimental Procedures: Compact tension C(T) specimens of the composite were machined from the heat-treated sheet using electric discharge machining in both the 0° (L-T) and 90° (T-L) orientations. Note that in the 0° orientation, the crack path is perpendicular to the fiber direction; in the 90° orientation, it is parallel to the fiber direction. Data were compared with that for the unreinforced constituent matrix alloy 6061 in the L-T orientation. Backface strain gauges were bonded onto the back of the specimen to provide *in situ* monitoring of the elastic compliance; such measurements permit estimation of the magnitude of crack closure, specifically the closure stress intensity, K_{cl} , by determining the first contact of the fracture surfaces during unloading. The d.c. electrical-potential method was used to determine crack lengths. The experimental set-up is shown schematically in Fig. 3.11. Crack-growth rates were determined over the range $\sim 10^{-11}$ to 10^{-6} m/cycle under computer-controlled K-decreasing and K-increasing conditions. A fatigue threshold stress-intensity range, ΔK_{TH} , below which crack growth is presumed dormant, was defined as the maximum stress-intensity range at which growth rates did not exceed 10^{-11} m/cycle. Thresholds were approached by varying the applied loads so that the instantaneous values of crack length, a , and stress-intensity range, ΔK , changed according to the equation:

$$\Delta K = \Delta K_0 \exp[C^* (a - a_0)] , \quad (3.4)$$

where a_0 and ΔK_0 are the initial values of a and ΔK , and C^* is the normalized K-gradient ($1/K \cdot dK/da$) set to $\pm 0.08 \text{ mm}^{-1}$. Crack-growth rate (da/dN) data are presented both in terms of the nominal stress-intensity range ($\Delta K = K_{max} - K_{min}$), and the effective (near-tip) stress-intensity range ($\Delta K_{eff} = K_{max} - K_{cl}$).

Results and Discussion: The variation in fatigue-crack propagation rates, as a function of the nominal stress-intensity range at $R = 0.1$, for the 0° and 90° orientations in the Al/SiC_f composite is shown in Fig. 3.12; data are compared with corresponding results in the constituent 6061 matrix alloy. It is apparent that continuous

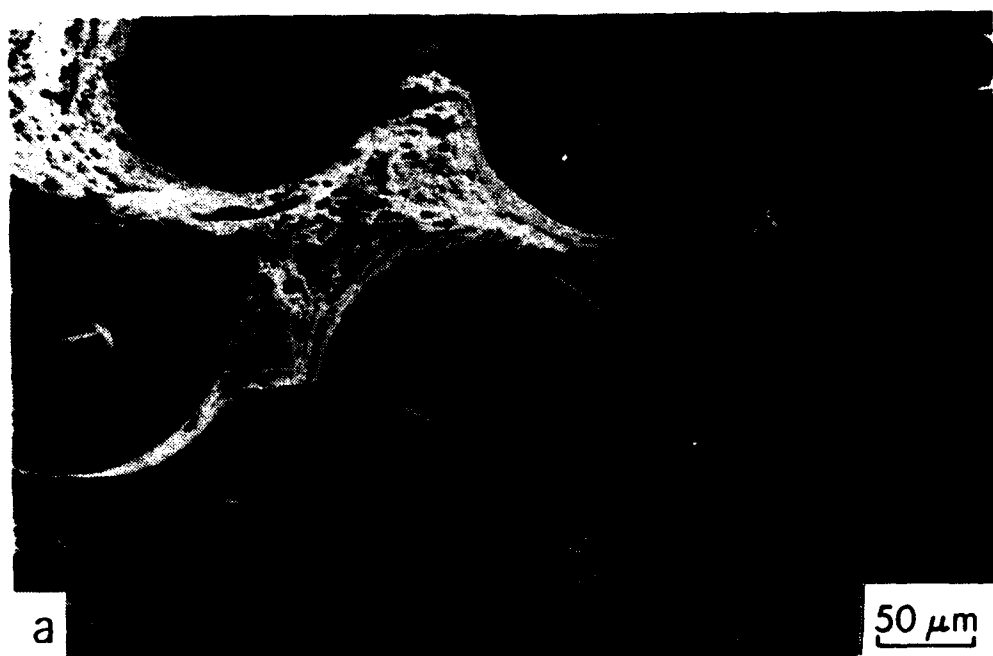


Fig. 3.8: SEM image of 0° 6061/SiC_f composite tensile fracture surface showing fiber cleavage and separation from the aluminum matrix; note the aluminum still adhering to fibers.

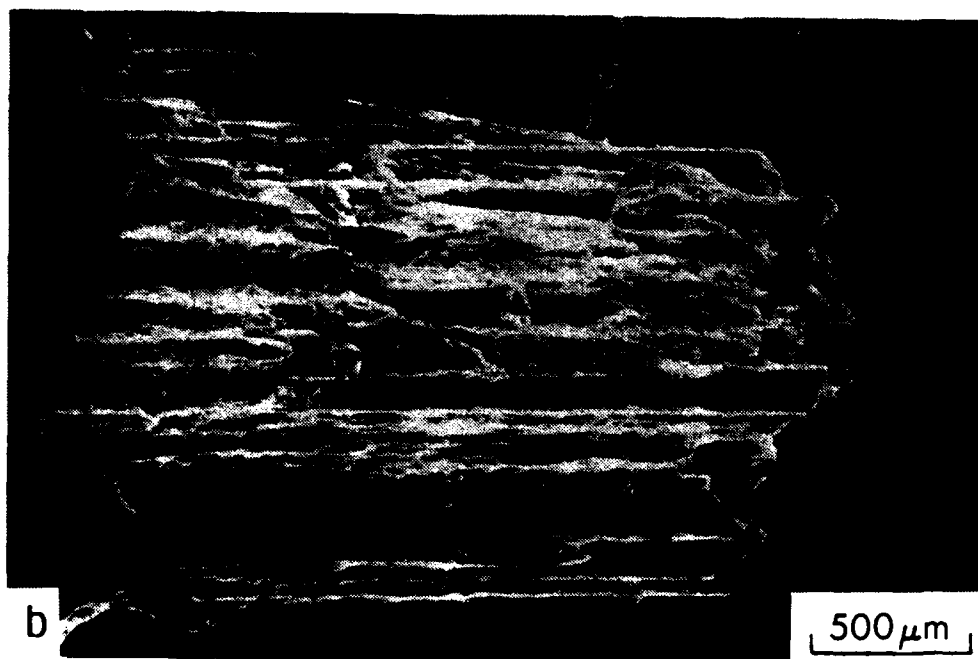
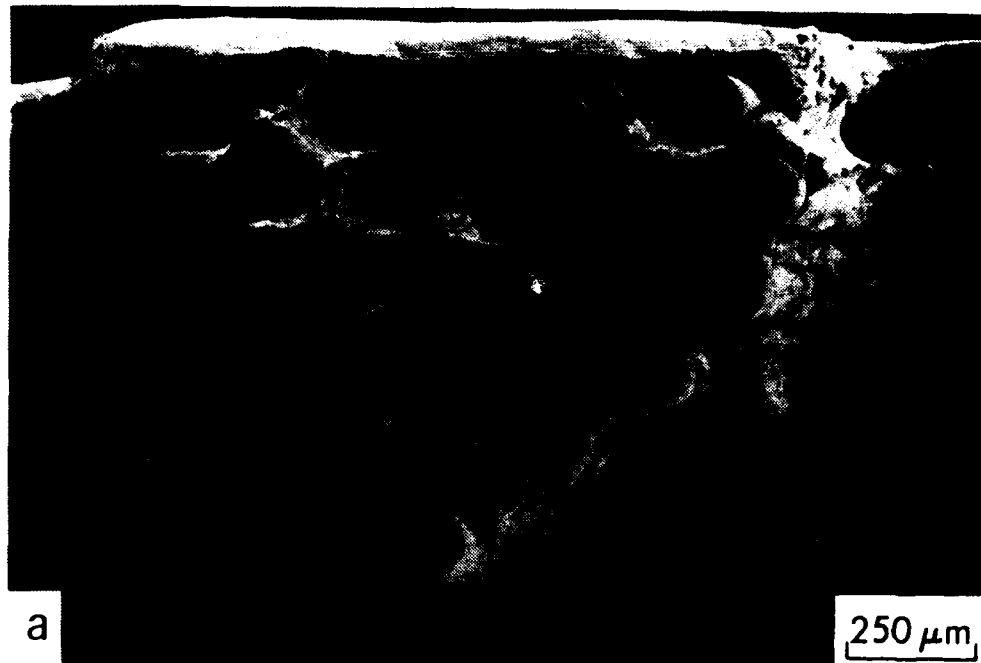


Fig. 3.9: SEM image of 0° 6061/SiC_f composite tensile fracture surface, a) top view, b) side view. Fiber pullout is evident in matrix as well as carbon core pullout from within the fiber.

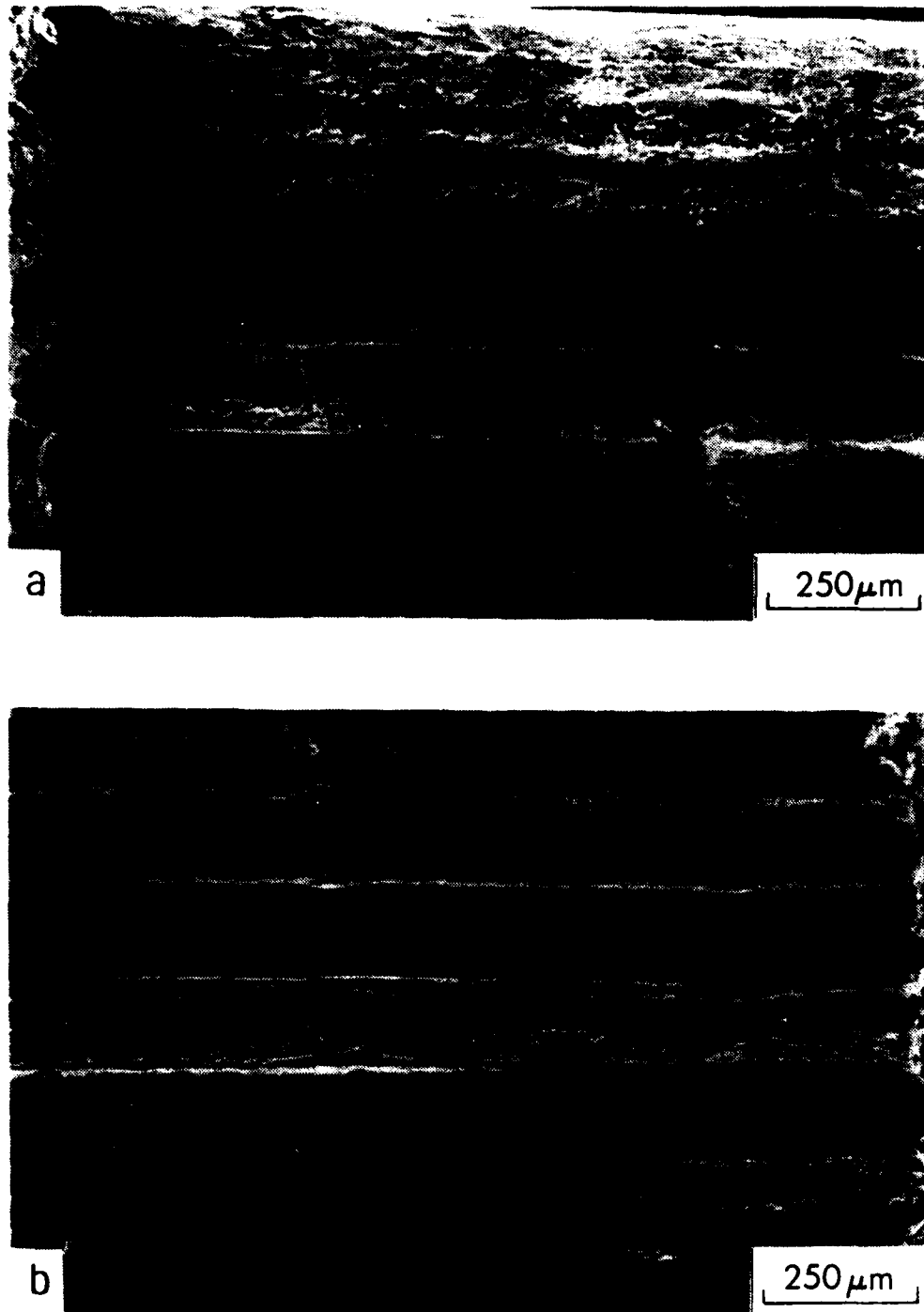


Fig. 3.10: SEM image of the a) LHS and b) RHS of a 90° 6061/SiC_f composite tensile fracture surface. Note the fiber cleavage and ductile fracture of the aluminum matrix. Fiber cleavage usually starts from the edge of the tensile specimen where EDM damage occurs.

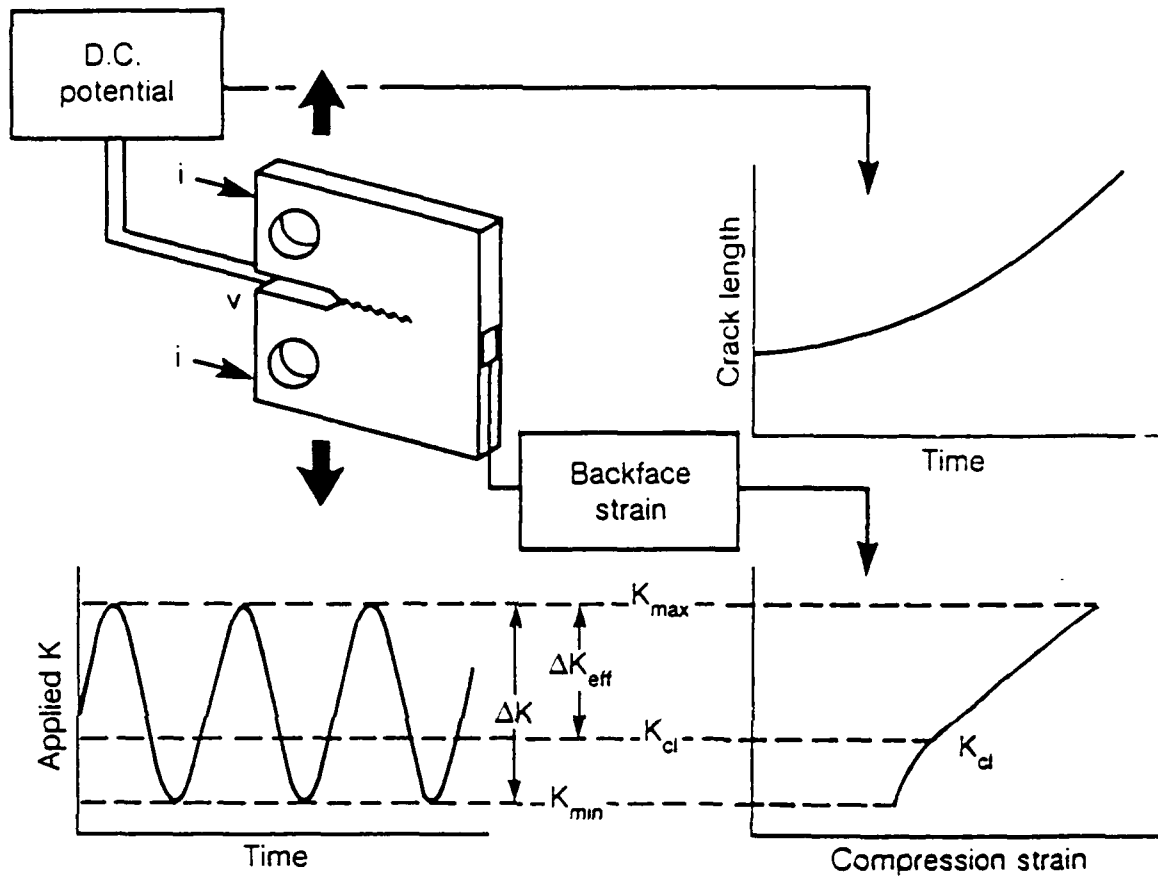


Fig. 3.11: Schematic illustration of the principal experimental methods used to continuously monitor crack length and crack closure. Crack closure was measured as the closure stress intensity (K_{cl}), at first deviation from linearity on the compliance curve, obtained using back-face strain compliance techniques.

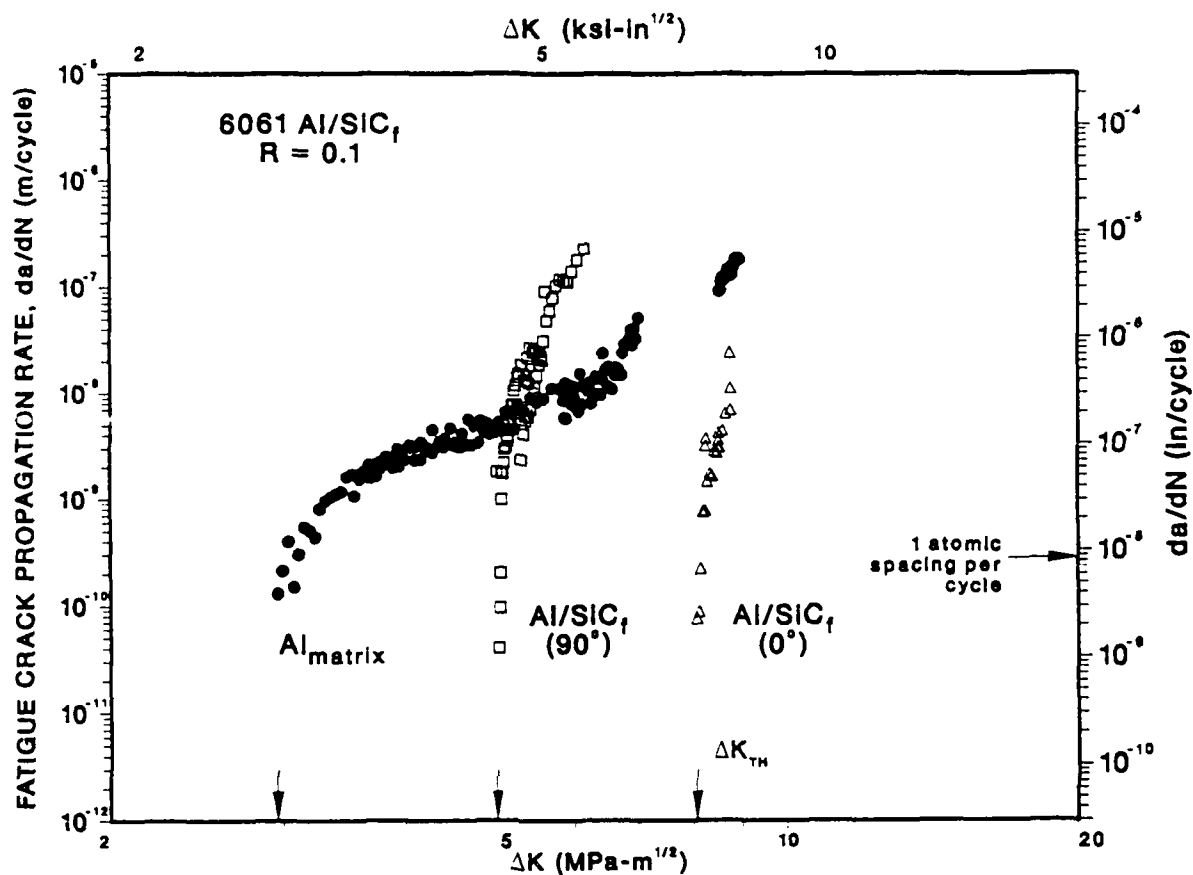


Fig. 3.12: Fatigue da/dN vs. ΔK data for 0° and 90° orientation of the 6061/SiC_f composite compared to the matrix monolithic aluminum alloy.

reinforcement with SiC fibers in general acts to reduce fatigue-crack growth rates in both 0° and 90° orientations compared to the unreinforced alloy; however, the dependence of growth rates on ΔK is far higher in the composites such that above $\sim 10^{-8}$ m/cycle, the matrix alloy can show slower growth rates.

Corresponding results on the magnitude of crack closure in the 90° composite and unreinforced matrix alloy are shown in Fig. 3.13. Characteristic of crack-tip shielding mechanisms originating from wedge contact between the crack surfaces [8], K_{cl} values increase with decreasing ΔK . However, closure levels are significantly higher at a given ΔK level in the composite. Such higher levels of crack closure are consistent with the extremely rough fracture surfaces in the composite, particularly through the test piece thickness (Fig. 3.14). Although fatigue failure in the 90° composite appears to involve fine-scale microvoid coalescence (Fig. 3.15), the crack path tends to follow a region close to the fiber interface, which leads to the through-thickness "hill and valley" fracture surface (Fig. 3.14). It is reasoned that such surfaces result in high closure levels due to asperity contact induced by Mode III (anti-plane shear) displacements, which cause a lack of registry between mating crack surfaces.

Measured threshold ΔK_{TH} values are considerably higher (~ 67 -167%) in both orientations in the composite, specifically ~ 8 and $5 \text{ MPa}\sqrt{\text{m}}$ for the 0° and 90° orientations, respectively, compared to $\sim 3 \text{ MPa}\sqrt{\text{m}}$ in monolithic 6061. Such high thresholds are certainly associated with higher levels of crack closure resulting from the rougher fracture surfaces in the composites, but may also be associated with a crack-trapping phenomena resulting from the presence of the fibers. Similar to behavior reported for particulate-reinforced aluminum-matrix composites [9], as the extent of crack-tip plasticity at ΔK_{TH} can be comparable with the size of the reinforcement (at $\Delta K = 5 \text{ MPa}\sqrt{\text{m}}$, the average plastic zone size is $\sim 5 \mu\text{m}$, compared to an average fiber diameter and spacing of ~ 140 and $50 \mu\text{m}$, respectively), the presence of the fibers can act to impede the motion of the crack front. This is perhaps apparent by replotting the data shown in Fig. 3.12 for the 90° composite and unreinforced matrix in terms of a near-tip ΔK_{eff} value, after correcting for the effect of crack closure. As shown in Fig. 3.16, whereas differences between the crack-growth behavior of the two materials are reduced, the composite still displays lower growth rates suggesting that mechanisms other than crack closure play a significant role.

3.6 Conclusions

1. The tensile strength of the Al/SiC_f composite in the 0° (longitudinal) orientation was found to be ~ 5 times higher than that of the matrix alloy; the elastic modulus was similarly 3 times higher. In the 90° (transverse) orientation, conversely, the tensile strength was extremely low (a factor of 3 less than the matrix alloy), although ductility values were 5 times higher than for the 90° orientation.

2. Fatigue-crack growth rates are significantly reduced in the composite compared to the unreinforced matrix alloy, except above $\sim 10^{-8}$ m/cycle in the 90° orientation (where crack extension is parallel to the fibers direction). Specifically, compared to the matrix alloy, fatigue threshold ΔK_{TH} values for the continuously-

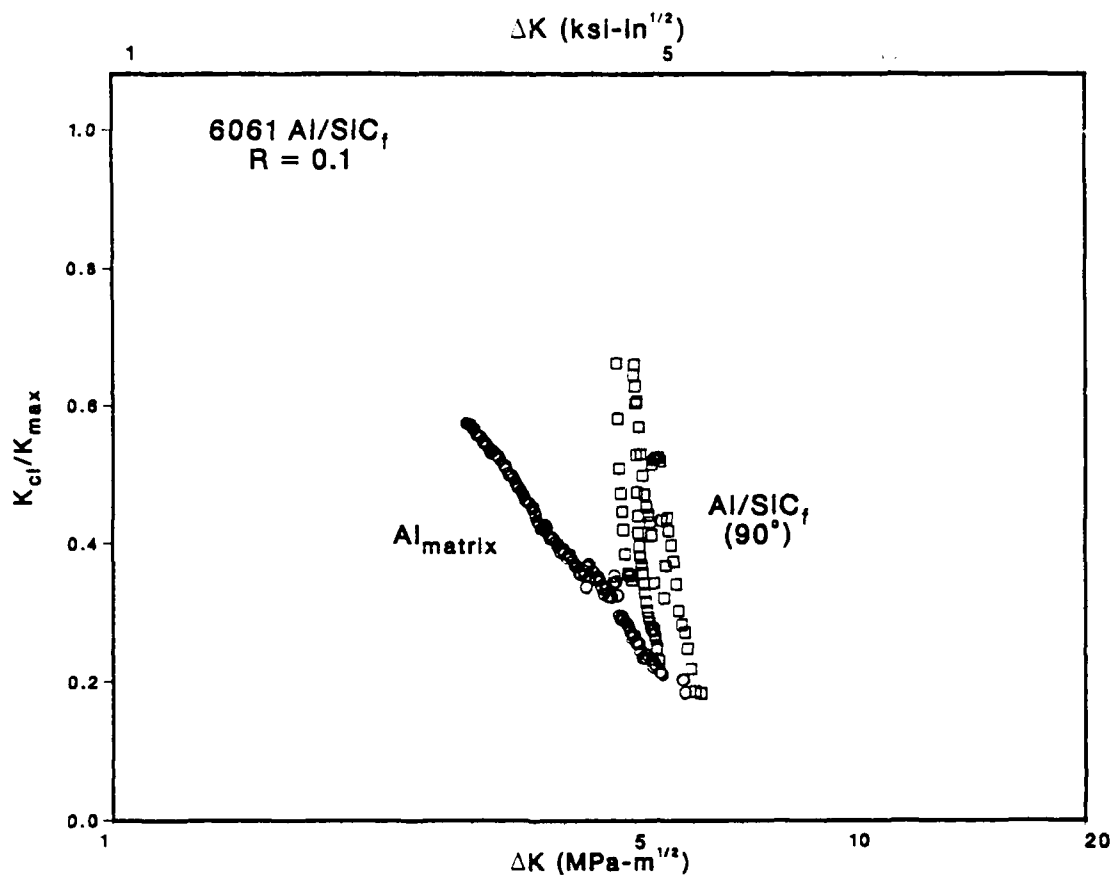


Fig. 3.13: Variation in crack closure for the Al/SiC_f composite and matrix material, plotted as K_{cl}/K_{max} as a function of ΔK .



Fig. 3.14: Compact test specimen Al/SiC_f composite (90° orientation, crack parallel to fibers) fractured under fatigue. Section of fracture surface looking into the crack mouth. Note the broken fiber out of focus in the background, thus showing the meandering and bridging of the crack. Fracture surface is very rough and not flat. Image taken in SEM at 25 keV, 200X.

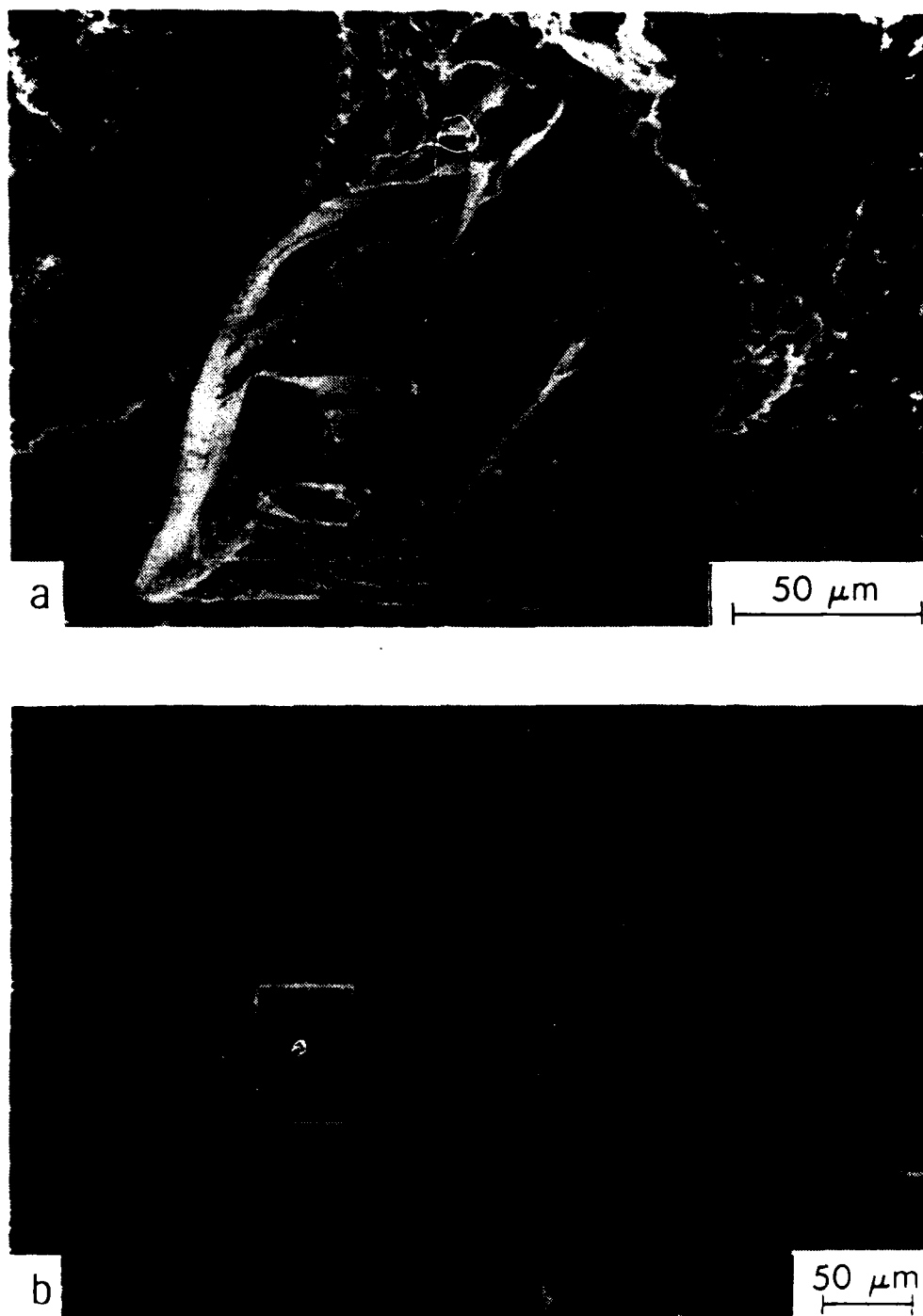


Fig. 3.15: SEM image of 90° Al/SiC_f composite fatigue fracture surface, $\Delta K = 5.5$ MPa \sqrt{m} , and crack propagation direction from left to right. Failure occurs near fiber/matrix interface with aluminum still adhering to the fibers.

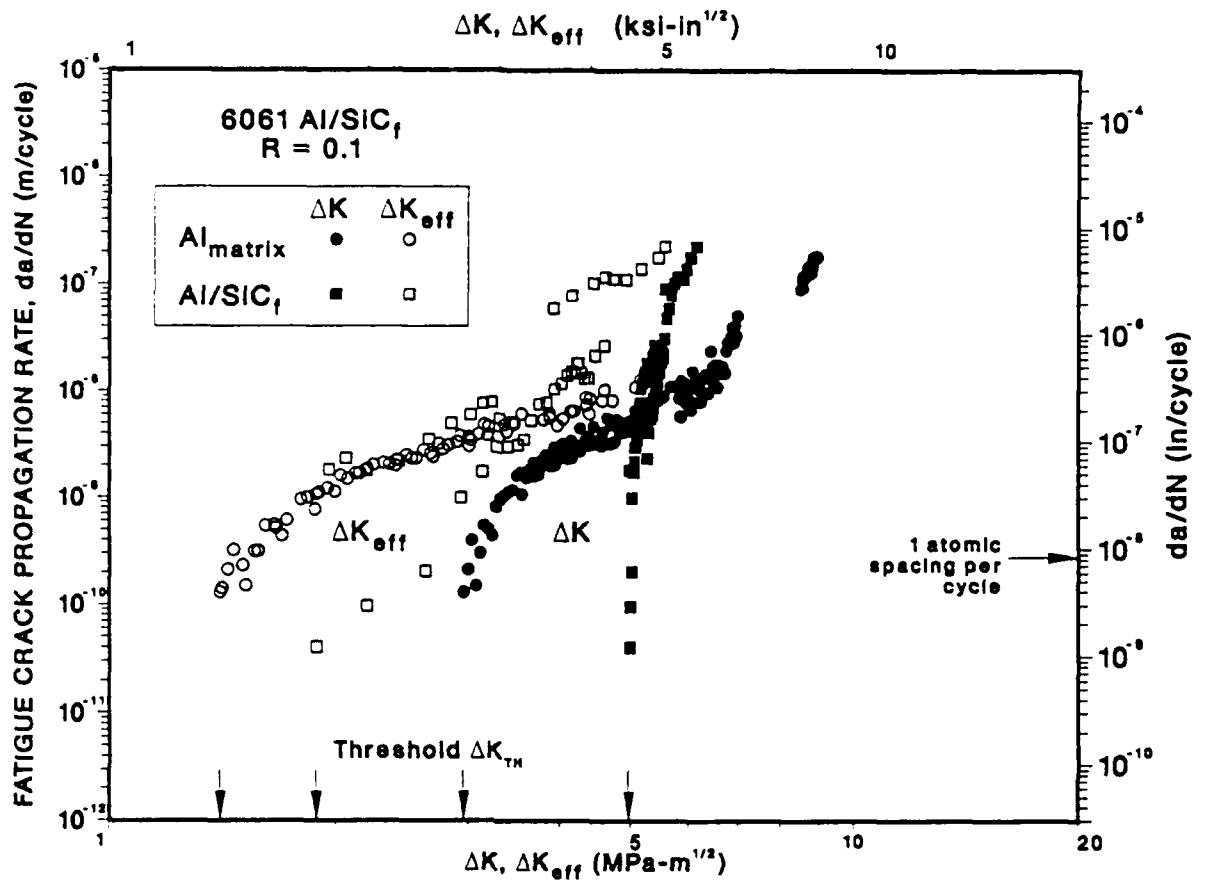


Fig. 3.16: Fatigue da/dN vs. ΔK data for Al/SiC_f composite and unreinforced matrix material as a function of ΔK and ΔK_{eff} .

reinforced composite are ~67% higher in the 90° (T-L) orientation and ~167% higher in the 0° (L-T) orientation.

3. The superior fatigue-crack growth properties of the 90° composite are concurrent with significantly higher levels of crack closure; this is presumed to be a function of their much rougher fracture surfaces (particularly through-thickness) which results from a "hill and valley" crack path close to the fiber/matrix interface. However, due to limited crack-tip plasticity at near-threshold levels, crack-trapping effects due to the presence of the fibers may also play an important role.

4. The higher fatigue-crack growth resistance is seen in the 0° composite; this is attributed to crack impedance at crack deflection and the fiber/matrix interfaces, which ultimately results in crack bifurcation along the transverse direction parallel to the fiber direction.

3.7 References

1. G. Thomas and D. R. Clarke, in Proc. Sixth European Congress on Electron Microscopy, 1976, p. 564.
2. Y. Flom and R. J. Arsenault, Mater. Sci. Eng., 77 (1986) p. 191.
3. V. Laurent, D. Chatain, N. Eustathopoulos, J. Mater. Sci., 22 (1987) p. 244.
4. T. Iseki, T. Kameda, and T. Maruyama, J. Mater. Sci., 19 (1984) p. 1692.
5. Anon, "Continuous Silicon Carbide Metal Matrix Composites," Textron Speciality Materials.
6. Anon, "Aluminum Standards and Data," Eighth Edition, The Aluminum Association Inc., 1984.
7. N. L. Hancox, Met. Mater. (1986).
8. R. O. Ritchie, Mater. Sci. Eng. A, 103A (1988) p. 15.
9. Jian Ku Shang and R. O. Ritchie, Acta Metall., 37 (1989) p. 2267.

4. MONOTONIC AND CYCLIC CRACK GROWTH IN A TiC-PARTICULATE-REINFORCED Ti-6Al-4V METAL-MATRIX COMPOSITE

4.1 Introduction

High specific strength, specific modulus and elevated-temperature properties of titanium and its alloys have made them ideal candidate matrices for developing high-performance metal-matrix composites for use in aerospace applications [1-7]. However, early work on Ti-matrix composites [1,2] has shown that extensive interfacial reaction can occur between typical reinforcements, e.g., B or SiC fibers, and the titanium matrix, which has a detrimental effect on overall composite properties. While attempts have been made to alloy titanium with different elements to obtain a compatible matrix composition [3], alternative reinforcing phases have also been suggested [4]. Among these, TiC is particularly attractive because it is completely compatible to titanium and its alloys, and high quality TiC particles are readily available. Moreover, cold and hot isostatic pressing (CIP/HIP) processes have recently been developed, which provide a viable method for the production of TiC particulate-reinforced Ti-6Al-4V composites [8].

The objective of this note is to describe the preliminary results of a study on the fatigue-crack growth and fracture-toughness behavior of such composites, specifically to examine the role of the reinforcement phase in affecting crack-growth resistance.

4.2 Materials and Procedures

The material used in this investigation was a 20 vol.% TiC particulate-reinforced powder-metallurgy (P/M) Ti-6Al-4V alloy composite (CermeTi-20 ELCl), received in the form of 30 mm diameter extruded rod, and with the chemical composition listed in Table 4.1. The alloy was processed by Dynamet (Burlington, MA) from alloy powders containing extra low chloride (5 ppm) CIP'd at 380 MPa pressure, vacuum sintered at 1200°C, HIP'd at a "proprietary" temperature/pressure, and held at 924°-980°C for 1-2 hr before being hot extruded. The resulting microstructure consisted of 100% Widmanstätten $\alpha + \beta$ with package sizes of 20 to 30 μm , with the distribution of TiC particles shown in Fig. 4.1. Particle analysis based on sampling 718 particles showed the average particle size to be 7.4 μm with a volume fraction of 28%. Particles were fairly spherical with an aspect ratio of 0.8. In addition, the composite contained about 5% porosity (Fig. 4.1), which increased from less than 1% at the center to ~7% on the outer layer of the rod; the majority of the voids were associated with clusters of particles. Mechanical properties of the composite alloy at ambient temperature are listed in Table 4.2.

Fatigue and fracture-toughness data for the composite are compared with those published previously [9,10] for the unreinforced matrix alloy, namely a HIP processed P/M Ti-6Al-4V alloy with a fully Widmanstätten $\alpha + \beta$ microstructure.

TABLE 4.1
Chemical Composition (in wt%) of the Matrix Alloy

Al	V	Ni	Cu	Zn	Ti
6.85	4.12	0.55	0.57	0.68	balance

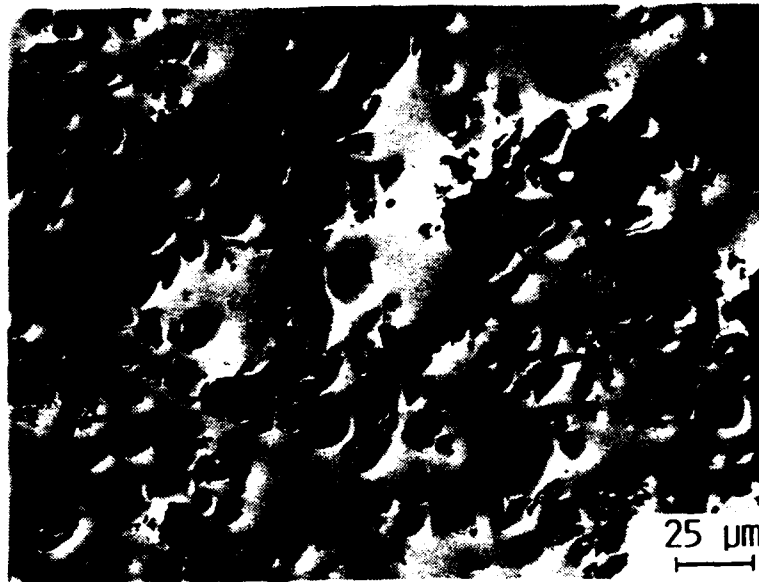


Fig. 4.1: Optical microstructure of TiC-particulate-reinforced Ti-6Al-4V composite alloy processed by cold and hot isostatic pressing [8], showing TiC particles and voids associated with particle clusters in the titanium alloy matrix.

Table 4.2
Room-Temperature Mechanical Properties

	Yield Strength (MPa)	Tensile Strength (MPa)	Elongation (%)	Redn. Area (%)	Young's Modulus (GPa)	K_{Ic} (MPa \sqrt{m})
TiC _p /Ti-6Al-4V	943	959	0.3	1.0	139	18.4

Fatigue-crack growth and fracture-toughness (resistance-curve) tests were performed on 6.4 mm thick disk-shaped compact tension (DC(T)) specimens, sliced from the extruded rod, with both the loading (Mode I) and crack-growth directions perpendicular to the extrusion direction. Fatigue tests were conducted in room air (22°C, 45% relative humidity) at a sinusoidal frequency of 50 Hz. Crack-growth rates over a range 10^{-6} m/cycle to 10^{-11} m/cycle were measured using electrical-resistance (K_{rak}) gauges mounted on specimens cycled in automated electro-servo-hydraulic testing machines under decreasing and increasing stress-intensity "K" control; the stress-intensity range ($\Delta K = K_{\max} - K_{\min}$) was varied exponentially with crack extension at a normalized K-gradient of 0.1 mm^{-1} and a constant load ratio ($R = K_{\min}/K_{\max}$) of 0.10. Full details are given elsewhere [11,12]. Specimens were subsequently examined using scanning electron microscopy to characterize fatigue and fracture surface morphologies.

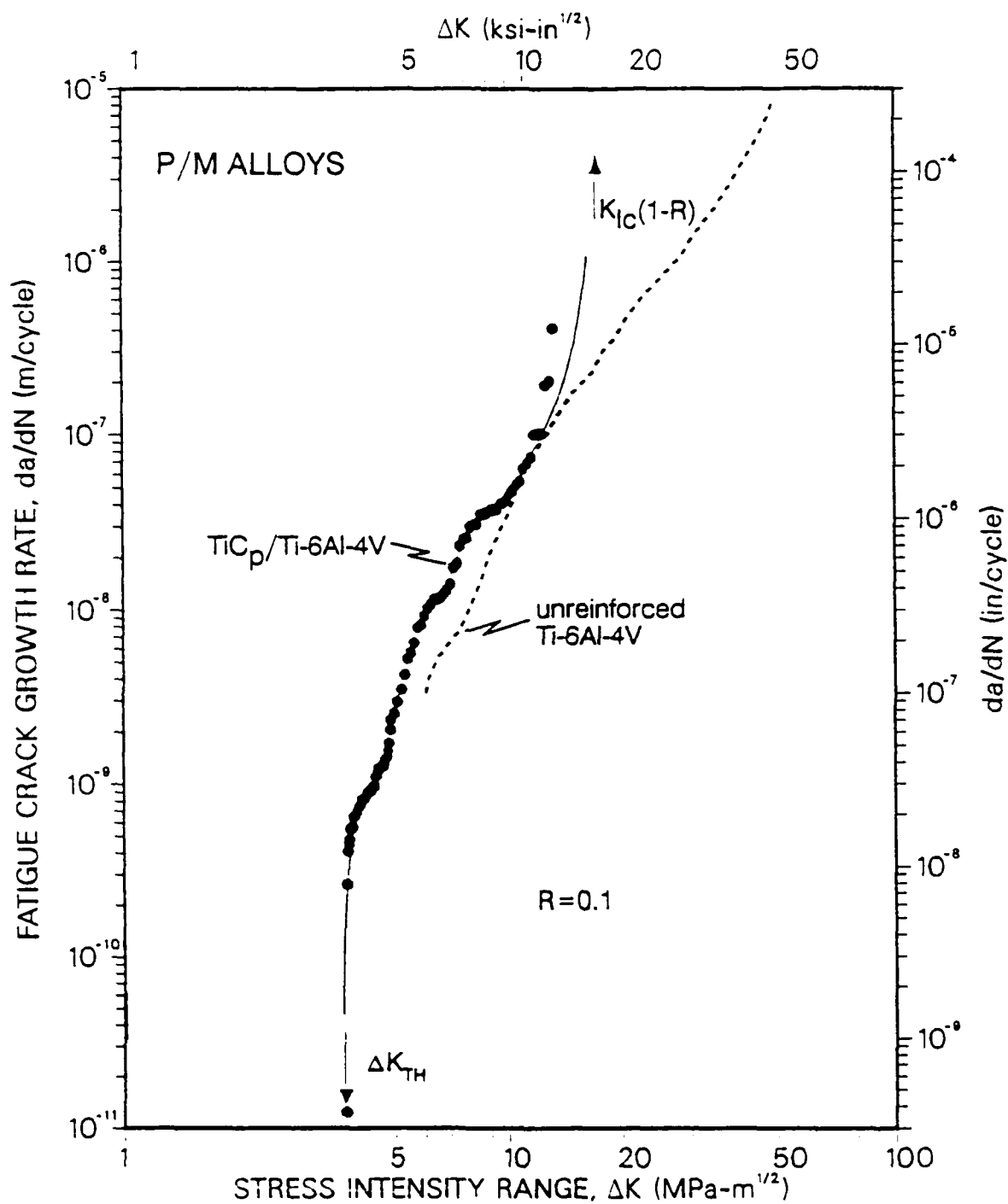
4.3 Results and Discussion

Fatigue-crack growth behavior for the as-received TiC_p-reinforced Ti-6Al-4V composite is shown in Fig. 4.2. Similar to most metallic monolithic and composite microstructures [e.g. refs. 13,14], crack-growth rates show a sigmoidal relationship with ΔK , in this alloy bounded by a threshold stress-intensity range ΔK_{TH} of $\sim 4 \text{ MPa}\sqrt{\text{m}}$ and a fracture toughness K_{IC} of $\sim 18 \text{ MPa}\sqrt{\text{m}}$. Compared to the unreinforced P/M matrix alloy [9], the composite displays similar fatigue-crack growth behavior over the mid-range of growth rates ($\sim 10^{-9}$ to 10^{-7} m/cycle). However, above 10^{-7} m/cycle, growth rates are far higher in the composite due to an earlier onset of fast fracture, resulting from the much lower toughness of the composite.

The fracture-toughness resistance-curve properties of the composite are shown in Fig. 4.3. Values of the crack-initiation toughness K_{IC} are approximately $18 \text{ MPa}\sqrt{\text{m}}$, over 4 times lower than the fracture toughness of the P/M matrix alloy which has been measured at $77 \text{ MPa}\sqrt{\text{m}}$ [10]. Crack-growth toughness, characterized by the slope of the resistance-curve, is associated with a series of crack jumps at roughly constant stress intensity ("pop-ins"); optical observation of crack extension on the surface and measurements from the electrical-resistance gauges suggest that such jumps result from highly nonlinear, stepwise advance of the crack front.

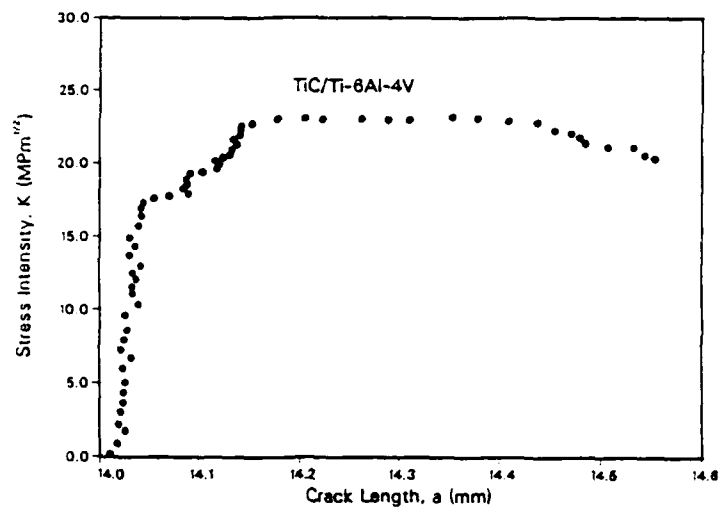
Fatigue and overload fracture surfaces are shown in Fig. 4.4. Under cyclic loading, the crack path does not appear to be greatly affected by the presence of the TiC particles or the porosity; in contrast to low ΔK fatigue behavior in SiC-particulate reinforced aluminum-alloy composites [14,15], the fraction of particles on the fatigue fracture surface approaches that of the particle volume fraction in the microstructure. However, fatigue fracture surfaces do show evidence of many cleaved TiC particles surrounded by laminar fracture of the $\alpha + \beta$ plates; also there are areas of loosely compacted aggregates presumably caused by lack of densification during processing (Fig. 4.4).

In contrast, the crack path appears to be markedly affected by the presence of TiC particles and porosity (from particle clusters) during monotonic (overload) fracture,



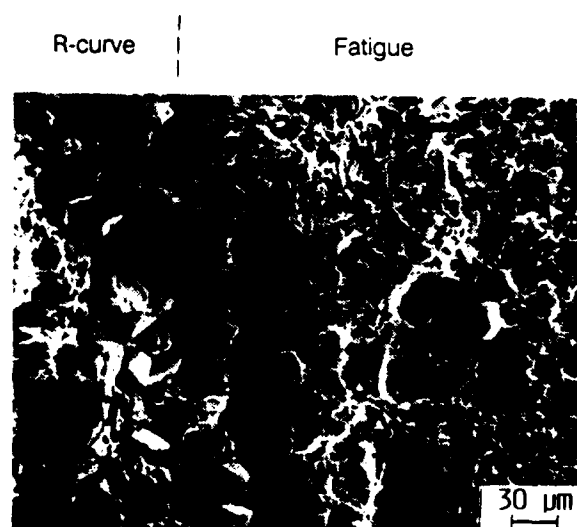
XBL 905-1928

Fig. 4.2: Variation in fatigue-crack growth rates (da/dN) as a function of the stress-intensity range (ΔK) for the as-received $TiC_p/Ti-6Al-4V$ composite alloy. Results are compared with those for the unreinforced matrix alloy [9] with similar Widmanstätten $\alpha + \beta$ microstructure.



XBL 905-1927

Fig. 4.3: Resistance-curve behavior used to estimate the fracture toughness K_{IC} of the as-received $TiC_p/Ti-6Al-4V$ composite alloy.



XBB 905-4355

Fig. 4.4: Fracture-surface morphology of $TiC_p/Ti-6Al-4V$ composite alloy, showing the transition in fracture morphology from fatigue-crack growth ($\Delta K \sim 8 \text{ MPa}\sqrt{m}$) to overload fracture ($K_{IC} \sim 18 \text{ MPa}\sqrt{m}$). Arrow indicates direction of crack growth.

consistent with the much lower toughness of the composite alloy compared to the unreinforced matrix material (Fig. 4.4). This can be understood by considering the different sampling volumes involved in crack propagation at different stress intensities (i.e., the volume of microstructure where the crack-tip stresses and displacements are sufficient to induce local cracking processes associated with crack advance) [15,16]. During fatigue-crack growth at ΔK levels below say 8 MPa \sqrt{m} , sampling volumes (which can be approximated by the maximum plastic-zone size) are of the order of 10 μm ; accordingly, the probability of the crack "seeing" a particle cluster or associated void is not large. Conversely, with the larger stress-intensity levels (~ 18 to 25 MPa \sqrt{m}) involved in monotonic crack extension, sampling volumes approach 60 to over 100 μm such that many voids can now interact with the crack-tip field; in fact, the crack is attracted to them. It is reasoned that this interaction between the crack front and the voids from TiC-particle clusters is responsible for the non-uniform crack extension and stepwise nature of the resistance curve, which in turn results in the low toughness of the composite material.

4.4 Conclusion

Compared to behavior in HIP-processed P/M Ti-6Al-4V monolithic alloys, fatigue-crack propagation behavior in extrusions of TiC-particulate reinforced P/M Ti-6Al-4V metal-matrix composites is found to be comparable for intermediate and near-threshold stress intensities below typically 10 MPa \sqrt{m} . However, the approximately 5% processing induced porosity associated with TiC particle clusters appears to have a very detrimental effect on high ΔK fatigue-crack growth and fracture toughness; in fact K_{IC} values for the composite alloy are 4 times lower than for the unreinforced material with similar matrix microstructure.

4.5 References

1. A. G. Metcalfe, J. Comp. Mater., 1 (1967) p. 356.
2. A. G. Metcalfe and G. K. Schmitz, SAE Transactions, 76 (1968) p. 2669.
3. A. G. Metcalfe and M. J. Klein, in Titanium Science and Technology, R. I. Jaffee and H. M. Burte, eds., Plenum Press, New York, NY, 1973, p. 2285.
4. J. Kennedy and G. Geschwind, *ibid.*, p. 2299.
5. D. S. Mahulikar, Y. H. Park, and H. L. Marcus, ASTM STP 791, American Society for Testing and Materials, Philadelphia, PA, 1981, p. 579.
6. D. L. Davidson, R. M. Arrowood, J. E. Hack, G. R. Leverant, and S. P. Clough, in Mechanical Behavior of Metal Matrix Composites, J. E. Hack and M. F. Amateau, eds., TMS-AIME, Warrendale, PA, 1987, p. 117.
7. K. S. Chan and D. L. Davidson, Metall. Trans. A, 21A (1990) in press.
8. S. Abkowitz and P. Weihrauch, Adv. Mater. Proc., 136(1) (July 1989) p. 31.

9. S. W. Schwenker, A. W. Sommer, D. Eylon, and F. H. Froes, Metall. Trans. A, 14A (1983) p. 1524.
10. F. H. Froes and D. Eylon, Powder Metallurgy Intl., 17 (1985) p. 235.
11. R. O. Ritchie and W. Yu, in Small Fatigue Cracks, R. O. Ritchie and J. Lankford, eds., TMS-AIME, Warrendale, PA, 1986, p. 167.
12. R. H. Dauskardt and R. O. Ritchie, Closed Loop, 17 (1989) p. 7.
13. R. O. Ritchie, Int. Met. Rev., 20 (1979) p. 205.
14. J.-K. Shang and R. O. Ritchie, in Metal Matrix Composites, R. J. Arsenault and R. K. Everett, eds., Academic Press, Boston, MA, 1990, in press.
15. J.-K. Shang, W. Yu, and R. O. Ritchie, Mater. Sci. Eng., 102 (1988) p. 181.
16. T. Lin, A. G. Evans, and R. O. Ritchie, J. Mech. Phys. Solids, 34 (1986) p. 477.

5. MICROSTRUCTURAL CHARACTERIZATION OF α_2 +B2 TITANIUM ALUMINIDE INTERMETALLIC (SUPER- α_2) USING TRANSMISSION ELECTRON MICROSCOPY

5.1 Introduction

Titanium aluminide intermetallic alloys (Ti_3Al , TiAl) are potential aerospace engine materials because of their superior thermal performance, lower density, greater strength and lower cost compared to current nickel-base superalloys [1-12]. Despite displaying high tensile ductility and strength at elevated temperatures, these materials have low toughness and ductility at ambient temperatures [1,4,5,7,9,12]. As a result, there is considerable effort towards developing compositions and processing methods that optimize mechanical performance.

Ti_3Al intermetallics are based on the α_2 phase which has the ordered hexagonal DO_{19} structure with a single-phase composition range from approximately 22-36 at.% Al [13,14]. At elevated temperatures, both a disordered HCP α -phase and BCC β -phase form [14,15]; the β -phase martensitically transforms upon quenching [5,16]. The "super- α_2 " alloys (composition in wt.% Ti-20Nb-14Al-3.2V-2Mo) [17] have slightly superstoichiometric Ti:Al ratios; however, the Nb, V and Mo additions stabilize [16,18-24] β at the expense of disordered α and reduce the M_s -temperature [16,22-24]. Thus, moderate quench rates can completely suppress the $\beta \rightarrow \alpha_2$ transformation [22], and subsequent ordering produces a B2 (CsCl) structure. Elevated temperature aging results in various dual-phase α_2 +B2 microstructures ranging from Widmanstätten α_2 [25] (below $\sim 900^\circ\text{C}$) to spheroidized α_2 in B2 (above $\sim 900^\circ\text{C}$) [17,21,26], while slow cooling produces the Widmanstätten α_2 [17,27]. Finally, an ordered analog (w_2) of the w phase in conventional titanium alloys has been reported to precipitate from B2 [16]. In essence, the super- α_2 system is the ordered analog of β -stabilized titanium alloys [24,28].

Transmission electron microscopy (TEM) analyses of conventional α and $\alpha+\beta$ titanium alloys are complicated because the β -phase spontaneously relaxes* in electrochemically-thinned foils and leads to artifacts that are not representative of bulk structures [29-34]. Ion-beam thinning has been shown to suppress spontaneous relaxation and preserve bulk structures [32]. In light of such thin-foil observations and the extensive phase analogies between the super- α_2 intermetallic and β -stabilized titanium alloys, the present effort was conceived to determine the nature of any TEM thin-foil artifacts and characterize representative microstructures of the bulk super- α_2 intermetallic. Jet polishing was selected because it is ubiquitous and reliable, although gentler electropolishing procedures (such as the window technique [30]) can also reduce spontaneous relaxation and often provide extensive thin area. The study involved a comparison of foils prepared by twin-jet electropolishing and ion-beam thinning after various amounts of prior plastic deformation.

* Spurling et al. [32] distinguish between spontaneous transformations, which result in new phases, and spontaneous relaxations, which produce morphological (but not necessarily phase) transformations.

5.2 Experimental Procedures

The super- α_2 alloy, of nominal composition (wt.%) Ti-20Nb-14Al-3.2V-2Mo, was originally cast as a 0.4 m diameter ingot, hot-forged above 1175°C in the β range to a 0.2 m bar, hot-rolled at the same temperature to a ~25 mm plate, β -annealed to minimize directionality, reduced to 13 mm in two equal 90° cross-rolling steps at a proprietary temperature, and finally annealed in the α_2 +B2 phase field at 980°C. A single-phase B2 microstructure was also examined after oil quenching a 15 mm cube from 1200°C.

TEM thin foils were prepared from as-received material in undeformed, 3% tensile ($\sigma_y \sim 890$ MPa) and 15% compressive-strained microstructures; undeformed single-phase B2 alloy was also examined for comparison. Prior deformation was achieved using flat 3.5×1.4 mm (ASTM E606-80) bars for tension, and ~5 mm cubes for compression; in all cases, TEM disks were cut parallel to the loading direction. Initial 400 μm thick slices were cut with a slow-speed diamond wafering blade and thinned on dry 240 grit SiC paper to 150 μm . Mechanically punched 3 mm disks were then reduced on 600 grit paper to 100 μm for jet polishing and 25 μm for ion-beam thinning. To minimize undesired deformation during this stage, ~0.006 m² of paper was used so that the effective grit size decreased as mechanical thinning proceeded.

A perchloric acid electrolyte (600 ml methanol, 350 ml n-butyl alcohol, 26 ml 70% perchloric acid) [29] was used for twin-jet electropolishing; the polishing conditions on a Struers Tenupol were -30°C and 30V with a nominal current of 65 mA. To prevent the hydride formation, which can occur in the brief period after sample perforation when the foils remain in the electrolyte without an applied voltage or electrolyte flow, samples were immediately removed and washed in methanol before the voltage and electrolyte flow were terminated [35]. To accomplish this, it was necessary to defeat the automatic cutoff feature of the jet-polishing unit and determine perforation visually. Identical foils have been prepared using sulfuric acid electrolyte (950 ml CH₃OH, 50ml H₂SO₄) [30] at -30°C and 14V with a lower jet flow rate.*

Ion-beam thinning was performed on a Gatan dual-stage ion mill fitted with a liquid nitrogen-cooled sample stage in which Ar⁺ ion beams sputter material from both disk surfaces. A 5.5 kV accelerating voltage, with 14° incidence angle and 0.25 mA current on each ion gun, was used to thin a specimen disk clamped between copper washers to maximize thermal connection to the stage. Milling times averaged 13 h for the initial perforation; milling was then continued for an additional 30 min at 4.5 kV and an incidence angle of 10°. A Phillips EM-301, with a double tilt goniometer, or

* Hydride formation was not anticipated to complicate B2 substructures in this study for several reasons: previous TEM investigations have shown that hydride formation in the α -Ti and α_2 titanium aluminides is suppressed using the polishing methods in the present study [13,29,35,36]. Recently published phase analyses in the α_2 +B2 aluminides have used the same thinning conditions without hydride formation [16,21,26,36]. Work in α_2 +B2 systems have shown that the α_2 phase has a greater propensity for hydride formation than the B2 phase [37]; there are no studies, to date, showing hydrides in the B2 phase.

single tilt liquid nitrogen cooling stage operating at 100 kV, was used for TEM, and a Phillips EM-400T was used for energy dispersive X-ray spectroscopy (EDS).

Bulk samples were mechanically polished with 1 μm diamond paste to a mirror finish and subsequently etched using Keller's reagent (95 ml H_2O , 2.5 ml HNO_3 , 1.5 ml 36% HCl , 1 ml 40% HF) for examination by optical and scanning electron microscopy. Hydrogen, carbon, oxygen and nitrogen were analyzed at Oremet Titanium (Albany, OR). Atomic absorption spectroscopy for trace metals was performed at Metallurgical Laboratories (San Francisco, CA).

5.3 Results

Low magnification optical observations revealed well-developed rolling texture of the prior- β grains and a tendency for α_2 alignment along the rolling direction. Fig. 5.1a is an SEM micrograph of as-received super- α_2 showing the discontinuous α_2 phase surrounded by continuous cubic phase. This microstructure resembles the two-phase microstructure for super- α_2 sheet hot-rolled at 1000°C [17]. The corresponding TEM micrograph in Fig. 5.1b (from a jet-polished foil) shows the α_2 phase as large, elongated grains in dark contrast and a continuous cubic phase in light contrast. The two phases are shown in greater relief in the low magnification TEM insert in Fig. 5.1b. Preferential thinning of the B2 phase, which was a problem in these as-received microstructures with approximately 50% α_2 volume fractions, was reduced in microstructures with higher α_2 volume fractions or finer microstructures such as those obtained by annealed β -quenched material at 900°C. Selected area diffraction (SAD) patterns from the continuous phase (Fig. 5.1c) clearly show B2 superlattice reflections in the [110] zone axis (the (001) and (111) superlattice reflections are forbidden in a disordered bcc structure), and display intense streaking along $\langle 211 \rangle$. Very faint w_2 spots in original SAD prints could not be reproduced (the spots were much fainter and more diffuse than in Ref. 16). Diffraction patterns from ion-milled foils were indistinguishable. Crystallographic striations (tweed) corresponding to the diffraction streaks were imaged, but discrete w_2 particles were not detected using dark field techniques.

Pronounced tweed contrast developed when β -quenched material was annealed as bulk samples for 2 hrs at 400°C. Selected area diffraction patterns from jet-polished commercial alloys (>60 ppm hydrogen, 50 ppm nitrogen) and experimental alloys (<5 ppm hydrogen, 350 ppm nitrogen) displayed marked differences after this treatment. The commercial material had strong evidence of α_2 -like precipitation (it was not established whether these were hexagonal or orthorhombic) and weak w_2 spots formed at $1/3\langle 211 \rangle$ in some areas, but experimental alloys developed the strong w_2 diffraction spots observed by Strychor *et al.* [16]. These β -quenched alloys also became exceptionally brittle after treatment at 400°C; mechanical punching of 3 mm TEM disks shattered the surrounding material in 400°C annealed samples, yet these disks punched cleanly by both β -quenched and as-received material. The B2 phase in as-received two-phase alloy did not show evidence of precipitation or enhanced tweed contrast after annealing at 400°C and continued to have good mechanical punching characteristics.

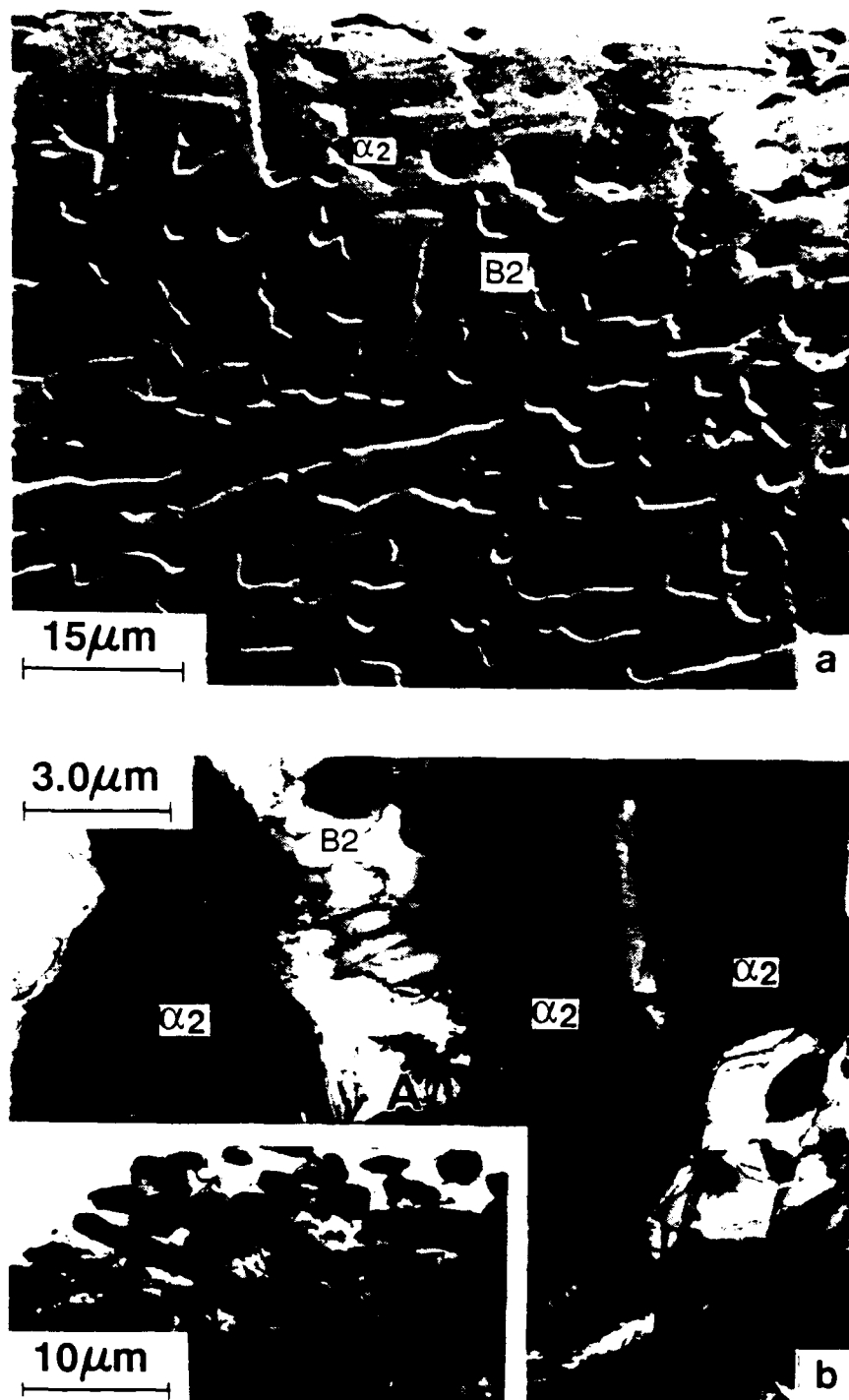


Fig. 5.1: General microstructure of super- α_2 titanium aluminide. a) Secondary electron image from a polished and etched surface showing the discontinuous α_2 grains in dark contrast and the B2 in bright contrast. b) TEM image from a jet polished foil showing thick α_2 grains and thin, continuous B2. The dark area marked A shows bend contours from a grain oriented near [001] B2. The inset illustrates the selectively thinned B2 phase produced during jet polishing. c) Selected area diffraction pattern and schematic drawing from $a=[1\bar{1}0]$ B2. The location of the w_2 reflections, too faint to be produced, are shown in the schematic. The heavy lines in the schematic show the direction of the SAD streaks that pass through bcc reflections, while the thin lines show the location of the faint streaks through B2 reflections.

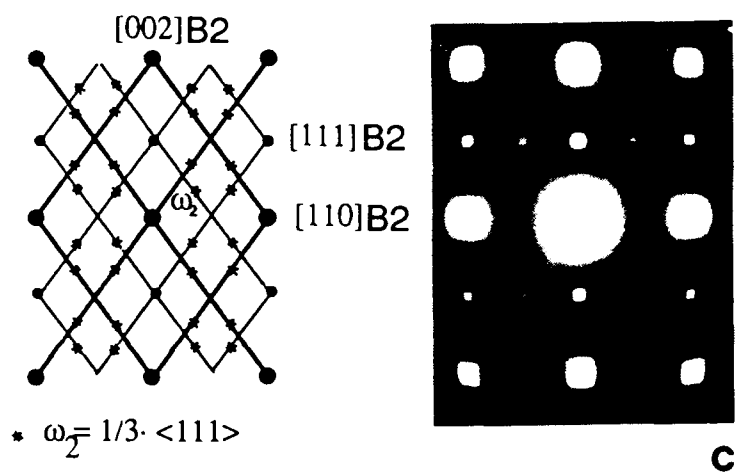


Fig. 5.1(c)

TEM micrographs of jet-polished as-received and β -quenched (100% B2) foils (Figs. 5.2a and 5.2b, respectively) show moderately high densities of dislocation loops which, in some areas, form lath-like systems. Such areas show lath-like residual contrast when imaged without strong diffraction contrast (Fig. 5.2c). Figs. 5.3a-d show the results of diffraction ($g \cdot b$) contrast analysis of dislocation loops in quenched material. Most of the loops, visible with two-beam diffraction conditions $z=[111]$ $g=1\bar{1}0$ in Fig. 5.3a, undergo nearly complete disappearance, consistent with $g \cdot b=0$, when the operating reflection is changed to $g=10\bar{1}$ (Fig. 5.3b). These reappear when the operating reflection is changed to $g=01\bar{1}$. In Fig. 5.3c, where the grain orientation has been changed to $z=[101]$ with $g=2\bar{1}1$, double images of the loop lines are visible when the deviation parameter, s_g , is near zero (when $s_g > 0$ the images become single) and is consistent with $g \cdot b=2$; conversely, when g is changed to $21\bar{1}$ ($s_g \approx 0$), the dislocation image contrast is very weak (Fig. 5.3d). Whereas inside-outside contrast (changes in loop dimensions) was observed when s_g was varied about zero for apparent $g \cdot b=1$ orientations, this behavior was absent when the faint residual loop contrast in apparent $g \cdot b=0$ orientations was analyzed. This confirms that the minimum contrast conditions in Figs. 5.3a and 5.3d occur at $g \cdot b=0$ [38]. Loop Burgers vectors of $b=\pm\frac{1}{2}[1\bar{1}1]$ are consistent with the above observations. Similar results were obtained from the two-phase as-received material, as illustrated by the loop visibility and invisibility conditions in Fig. 5.4a and 5.4b at $z=[111]$.

In Fig. 5.5, antiphase boundaries (APB's) are visible within the dislocation loops in the quenched material, and thermal APB's (formed when the β ordered during the quench) thread the image. It is interesting to note that antiphase boundaries can form to accommodate deviations from stoichiometry from the fully ordered state. These nonconservative antiphase boundaries arise in prismatic loops with $\frac{1}{2}\langle 111 \rangle$ Burgers vectors. Pure shear loops (loops with b in the habit plane) will also form antiphase boundaries, but these will be conservative. Traces from edge-on loops are consistent with shear loops in $\{110\}$ habit planes and energy dispersive X-ray analysis (EDS) from adjacent areas of high and low loop density (as in Fig. 5.1) exhibit neither significant nor the systematic compositional differences that would indicate nonconservative APB's are in the loops. Magnification-rotation calibration errors and limitations on detector sensitivity make it impossible to rule out the presence of slightly prismatic loops. The absence of thermal APB contrast in the as-received alloy is consistent with observations of α_2+B2 rather than $\alpha_2+\beta$ equilibrium at the 980°C two-phase anneal temperature [26]. No closely spaced superdislocations were imaged in weak beam dark field images which might account for the lack of APB contrast in dislocation loops, but loop depth, loop inclination, or loop dimensions will also affect APB visibility. Although some contrast differences between the as-received and 100% B2 microstructures exist, specifically the lack of APB contrast inside dislocation loops in the as-received material, other similarities in loop morphology and contrast imply these dislocations have the same character.

In all cases, foils that developed dislocation loops as thin foil artifacts displayed star-shaped buckling patterns around the perforation. These presumably were caused by the mechanical action of the electrolyte jets; while reduced flow rates decreased the size of the star patterns, such patterns were present even at the minimum jet flow setting. Thus, mechanical action probably plays some role in the generation of the

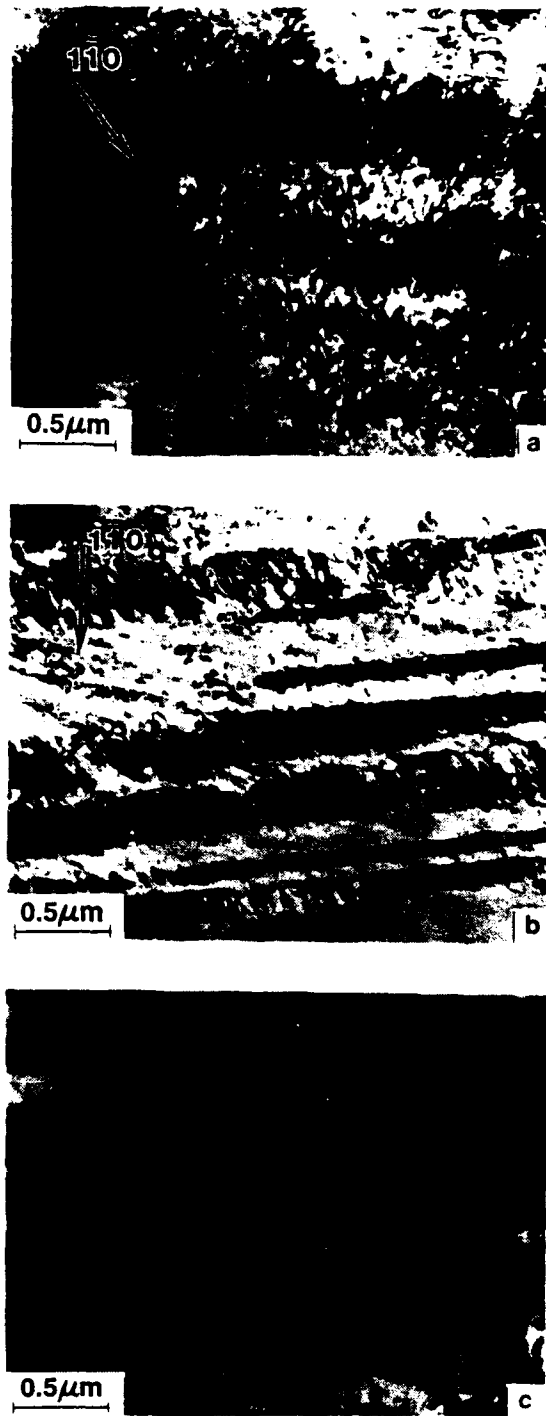


Fig. 5.2: Dislocation loop structures in jet polished foils from as-received super- α_2 (a) and quenched, β -annealed material (b) showing high dislocation density loop bands (laths). (c) Residual lath-like contrast from out-of-contrast loops in the quenched material.



Fig. 5.3: Diffraction contrast analysis in a jet-polished quenched sample. (a) $[111]B2$ zone axis (ZA) two-beam image showing strong dislocation loop contrast ($g \cdot b = 1$). Boxed area corresponds to (c). (b) Two-beam image from $[111]ZA$ corresponding to the $g \cdot b = 0$ dislocation loop invisibility criterion. (c) Two-beam image from $[110]ZA$ showing double images from dislocations when $g \cdot b = 2$. (d) Two beam image from $[110]ZA$ showing dislocation disappearance at a second $g \cdot b = 0$ condition and confirming $b = \pm \frac{1}{2}[1\bar{1}1]$. The arrow highlights the same dislocation in all four images. Note that the dotted line is the $[01\bar{1}]$ tilt axis used to change zone axes.

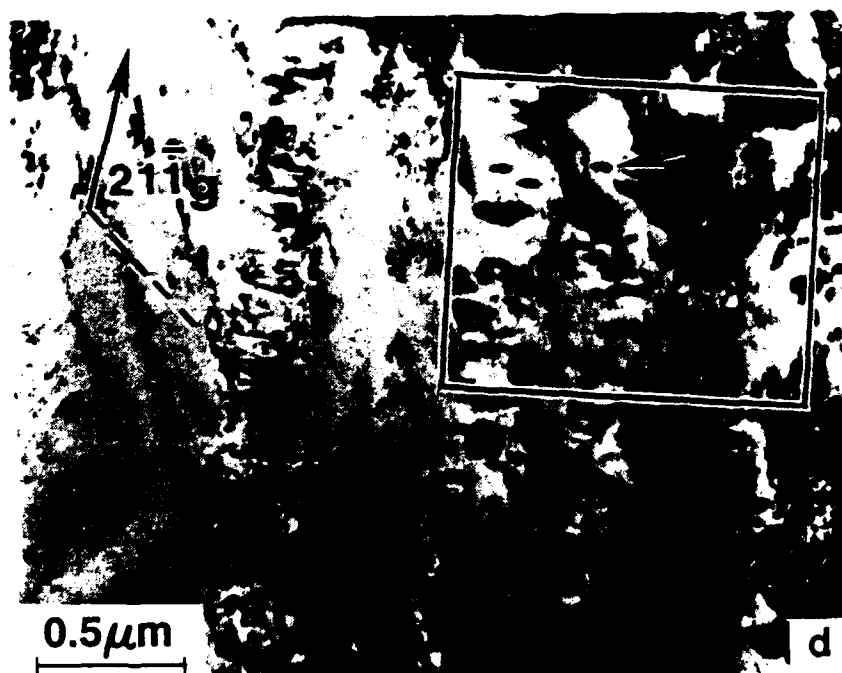
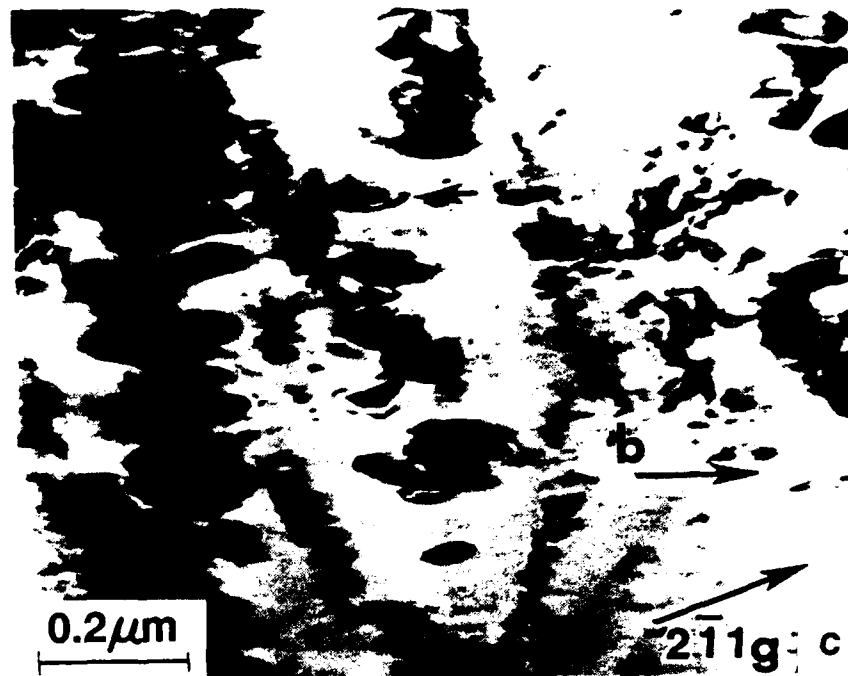


Fig. 5.3(c,d)

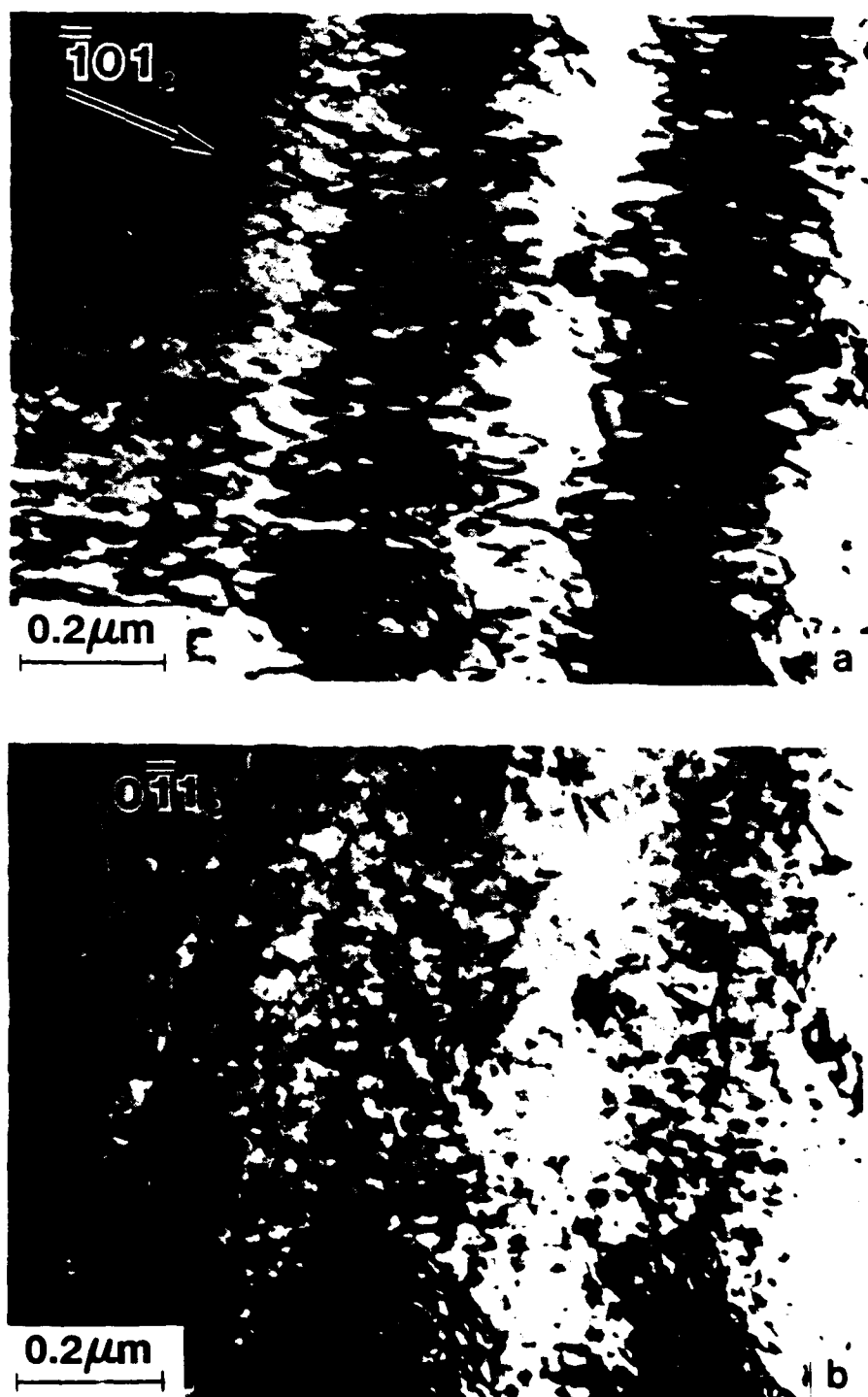


Fig. 5.4: Visibility (a) and invisibility conditions (b) for dislocation loops in a jet polished as-received foil in the [111] orientation.

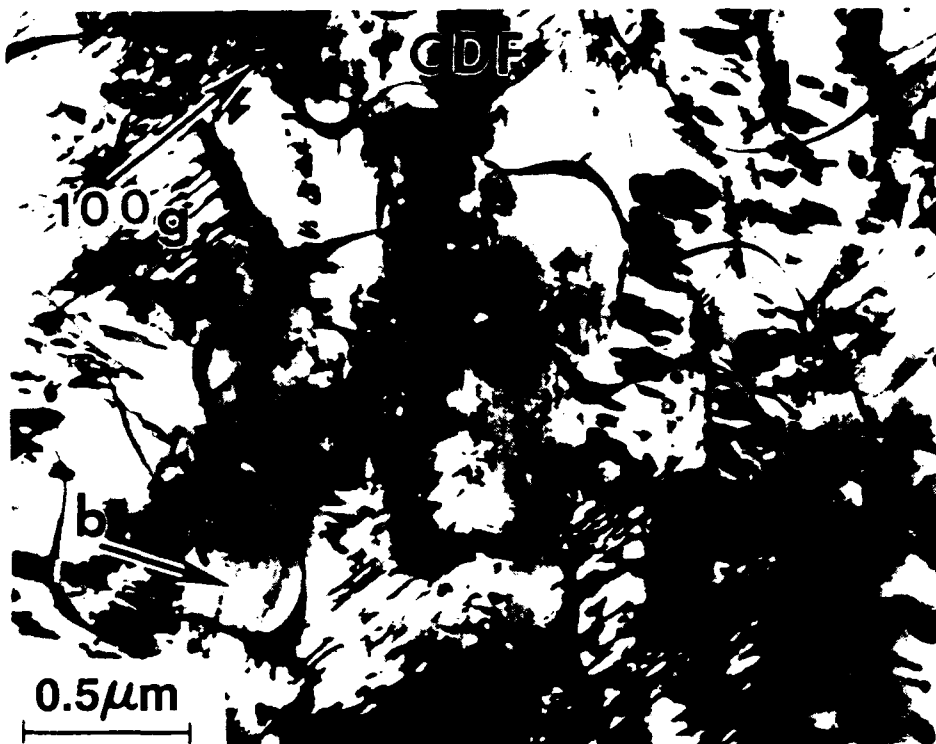


Fig. 5.5: Centered dark field image from the $[110]_{\text{ZA}}$ and same area as Figs. 3b and 3c showing thermal antiphase boundaries (APB's) threading the image and shear APB's within dislocation loops.

dislocation loops. For example brittle samples, which are presumably resistant to deformation, such as the β -quenched and aged at 400°C in Fig. 5.7a, have finely dispersed precipitates and show strong tweed contrast and very low dislocation densities although the post-quench pre-anneal foils have very high loop densities. If the β -quenched samples are deformed prior to the 400°C anneal, though, dislocations are present in the TEM images (Fig. 5.7b). Thus, the 400°C anneal does not remove existing dispersions.

In contrast to jet-polished foils, ion-milled foils from the as-received alloy display very low dislocation densities in the B2 phase (Fig. 5.6, $z=[111]$ $g=1\bar{1}0$). Unlike the B2 phase, dislocation densities in the hexagonal α_2 phase show little sensitivity to the sample preparation technique. However, ion milling thins both phases at similar rates (unlike jet-polishing where the α_2 phase remains thicker than the B2) and enables simultaneous contrast analysis on structures in adjacent phases. B2 grains oriented near the Bragg angle ($s_g \sim 0$) appear heavily mottled due to ion milling damage. Transient formation of martensite during jet polishing may account for the difference in dislocation densities between ion milled and jet polished foils. This was not expected though because cold stage ion milling should cool the TEM foil below the -30°C temperature encountered during jet polishing. Furthermore, *in situ* cooling in the TEM with a liquid nitrogen-cooled specimen holder failed to cause a martensite transformation in either jet-polished or ion-milled foils. Finally, homogeneous B2 ion-milled samples (which should have the greatest tendency to form martensite) were dipped in liquid nitrogen before inspection in the TEM, but dislocation loops did not form even if the foils were vigorously shaken.

Chemical effects do not appear to cause jet polishing artifacts. Dislocation loops could not be induced in the ion milled foils by immersing in the jet polishing solution for short periods with 30V applied potential (immersion for more than 10 sec destroyed the thinned area). Immersion for up to 10 minutes with no applied voltage at both -30°C and 20°C did not induce artifacts in the B2 phase although hydride formation in the α_2 phase has been demonstrated in earlier studies [35]. Finally, cathodic charging for up to 10 min at -1.5V in 1N HCl failed to form hydrides which might decompose and leave dislocation loops.

Similar TEM images, showing high dislocation densities and slip lines, were obtained from both the 15% compressively strained-and-electropolished and compressively strained-and-ion-milled foils (Figs. 5.8a and 5.8b, respectively); however, Burgers vector analysis was inconclusive due to these high densities. The slip line directions conform to traces from $\{110\}$ slip planes, but confirmation requires additional stereology. Prestrain markedly increased dislocation densities in ion-milled samples (Figs. 5.6, 5.8b, 5.9a-c), whereas dislocation densities in jet-polished samples showed only slight sensitivity to prestrain (Figs. 5.8a, 5.9d).

Dislocations in ion-milled, 3% tensile prestrained material are generally straight or slightly curved (e.g., Fig. 5.9a). The dislocation contrast in ion-milled tensile prestrained material (Figs. 5.9a-c) is consistent with screw dislocations of $b=\frac{1}{2}\langle 111 \rangle$: image disappearance occurs when $g \cdot l = 0$ (where l is the trace of the dislocation line, u , in the image) and image doubling occurs when g is parallel to l ; however, these are

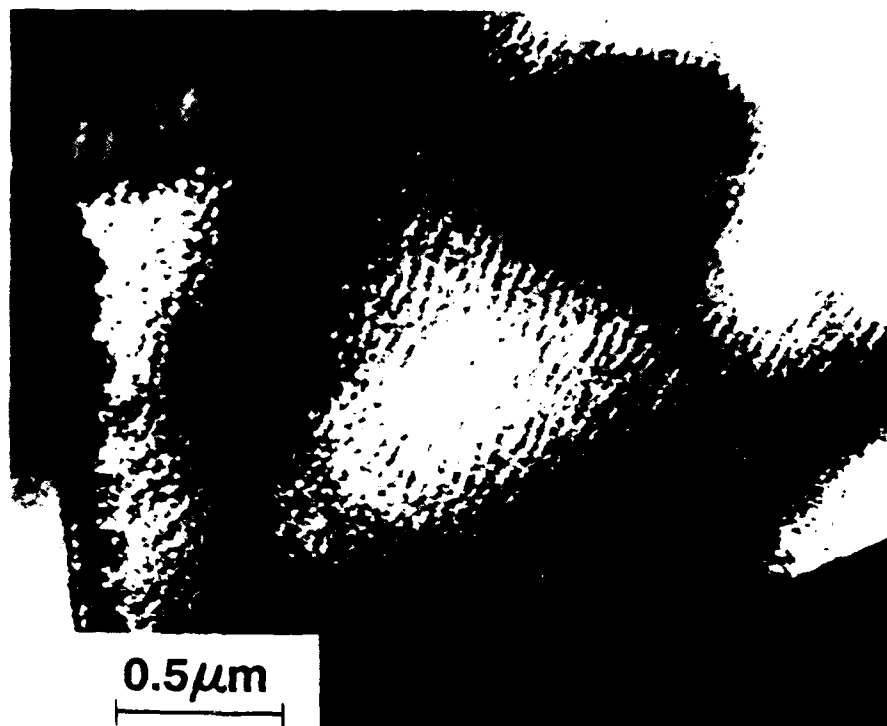


Fig. 5.6: $\langle 111 \rangle$ B2 ZA/110g two-beam image of ion milled as-received sample showing low ambient dislocation density and extensive mottling from ion beam-induced point defect clusters.

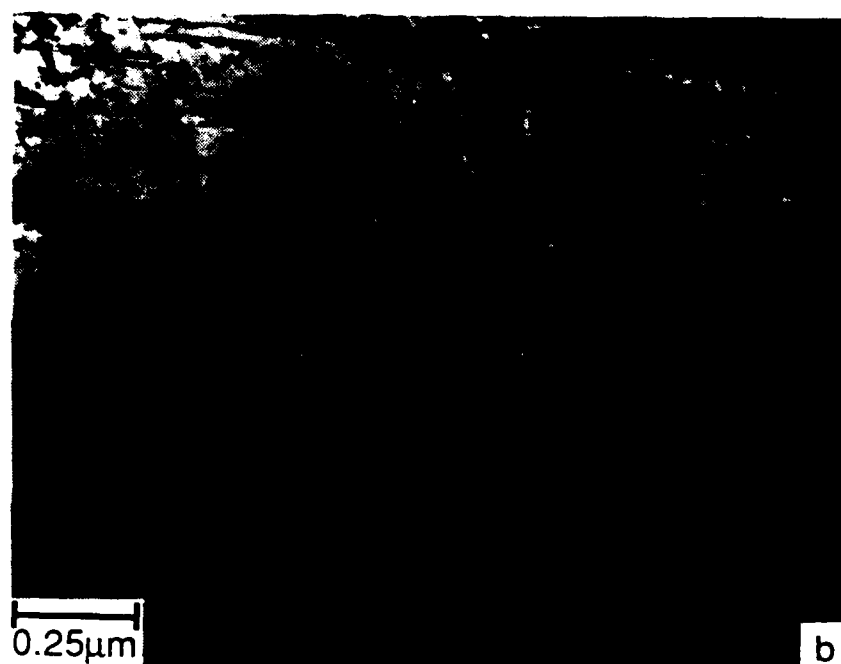
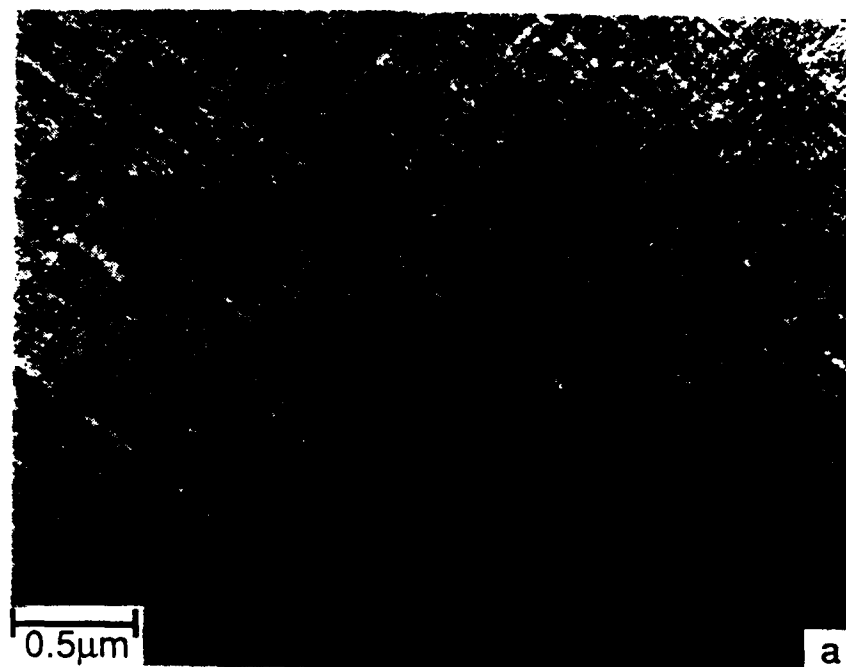


Fig. 5.7: TEM micrographs from jet-polished foils of β -quenched material following 2h annealing at 400°C, showing microstructures formed a) after no pre-anneal deformation and b) after 15% pre-anneal compression.

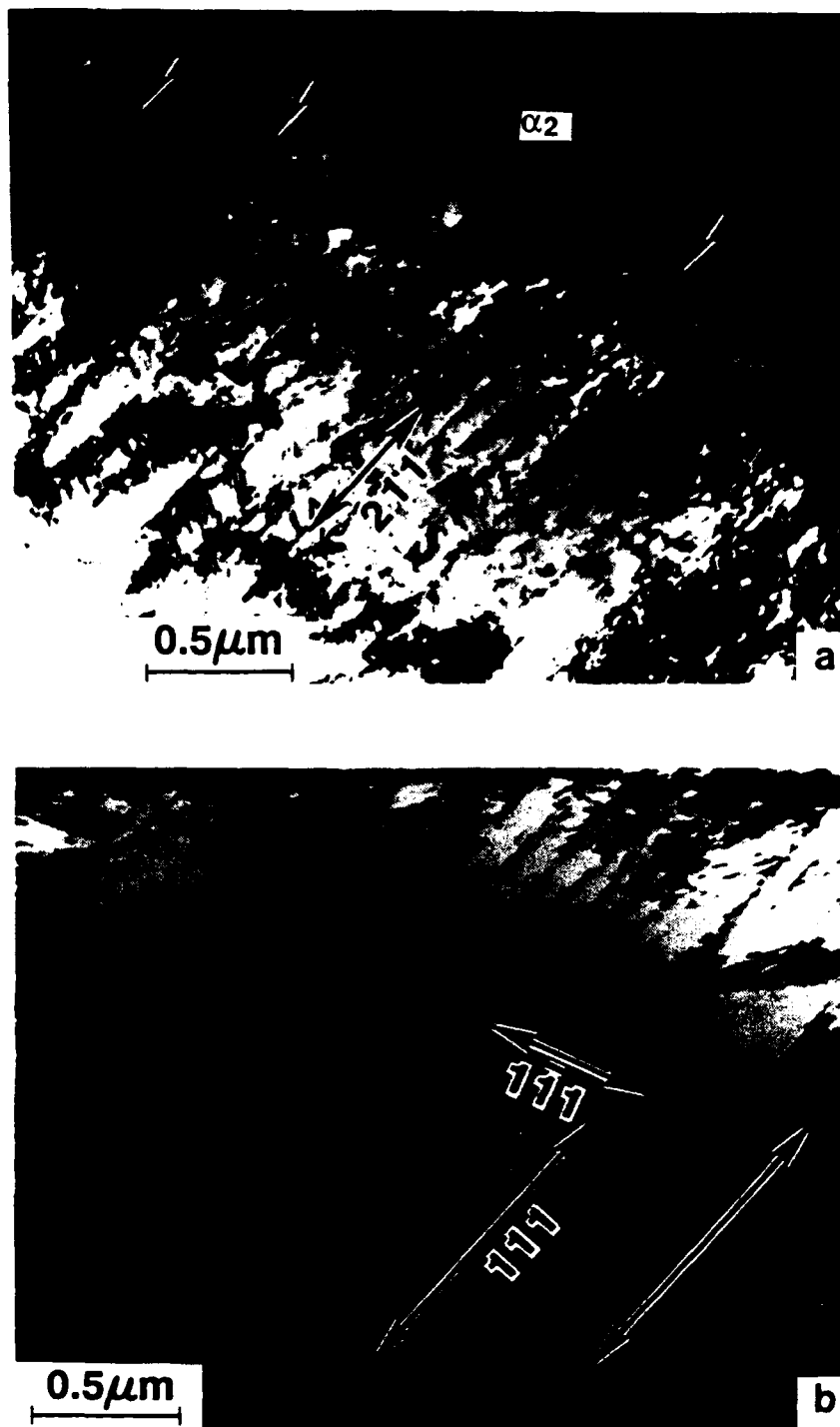


Fig. 5.8: Comparison of dislocation structures in a 15% prestrained, jet polished foil (a) and 15% prestrained, ion milled foil (b). In (a) foil is in a $\langle 111 \rangle_{\text{ZA}}$ and the predominant planar slip traces are along $\langle 211 \rangle$. In (b) the foil is in a $\langle 110 \rangle$ orientation and a number of slip traces along one family of $\langle 111 \rangle$ run from lower left to upper right. A second, less pronounced trace along another set of $\langle 111 \rangle$ runs from upper left to lower right. The arrows in (a) mark slip steps at the α_2 -B2 interface.

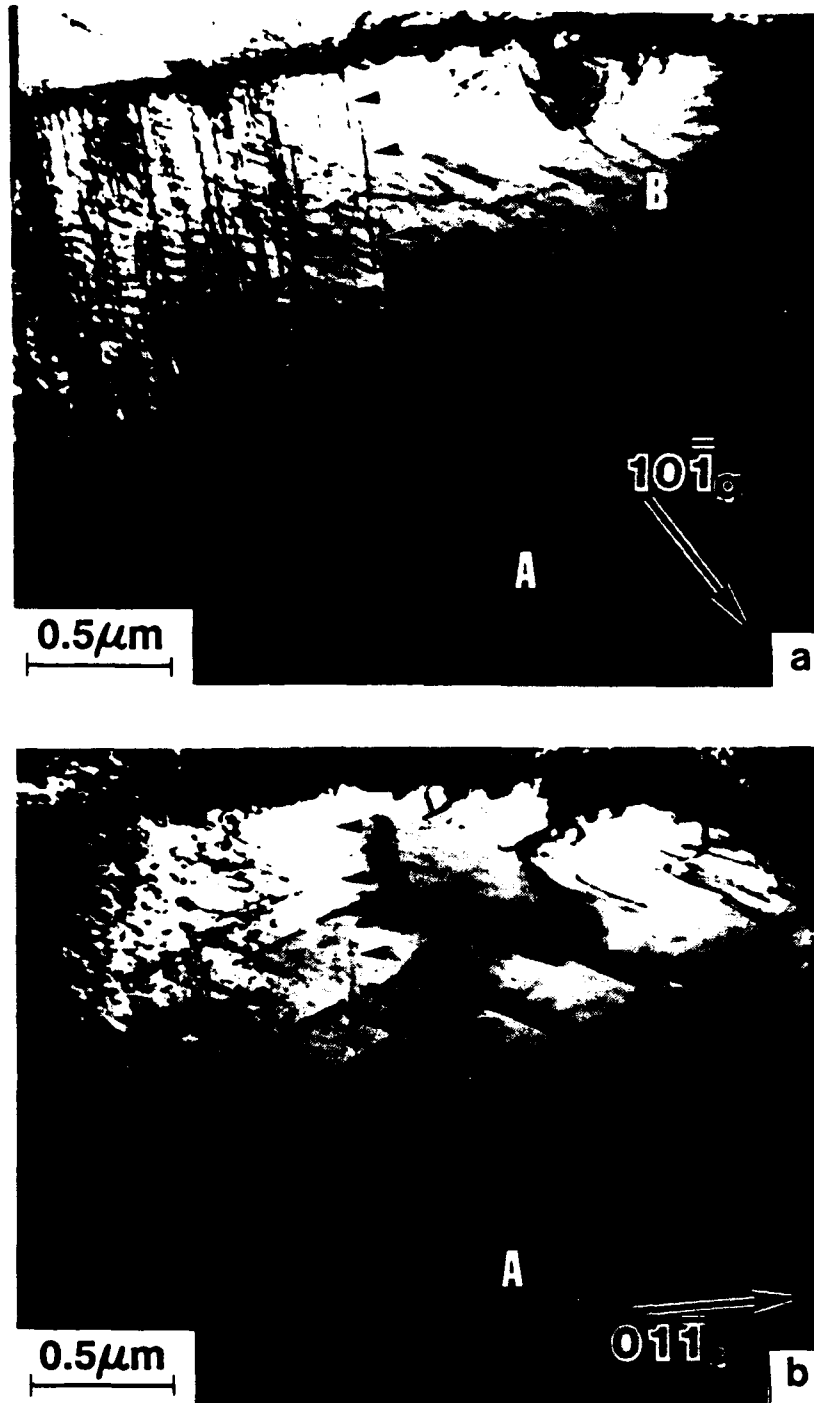


Fig. 5.9: (a)-(c) Diffraction contrast analysis of dislocations in ion-milled, 3% prestrained as-received material in $[111]_{ZA}$. The arrow-marked dislocations with line projections parallel to $[211]$ in (a) disappear when $g=011$ ($g \cdot b=0$) in (b) and double when $g=\bar{2}11$ ($g \cdot b=2$) in (c). A second set of dislocations parallel to $[1\bar{2}1]$, invisible in (a), become visible in (b) (labeled A), while a third set along $[11\bar{2}]$ (marked B) are visible in (a) and (b). (d) Comparison micrograph from jet-polished 3% prestrained material in a $\langle 110 \rangle$ orientation showing a hybrid structure of dislocation loops with b along b_2 and linear dislocations along b_1 .

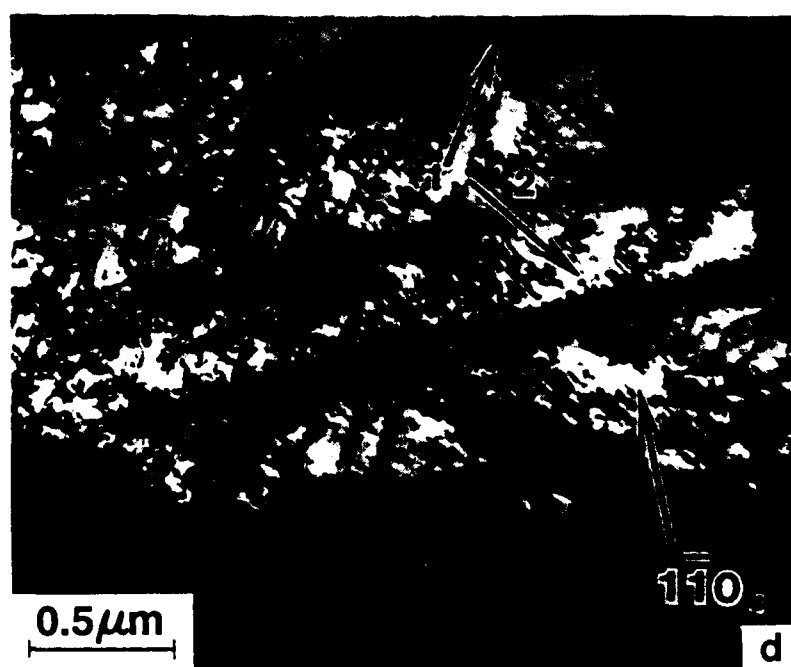
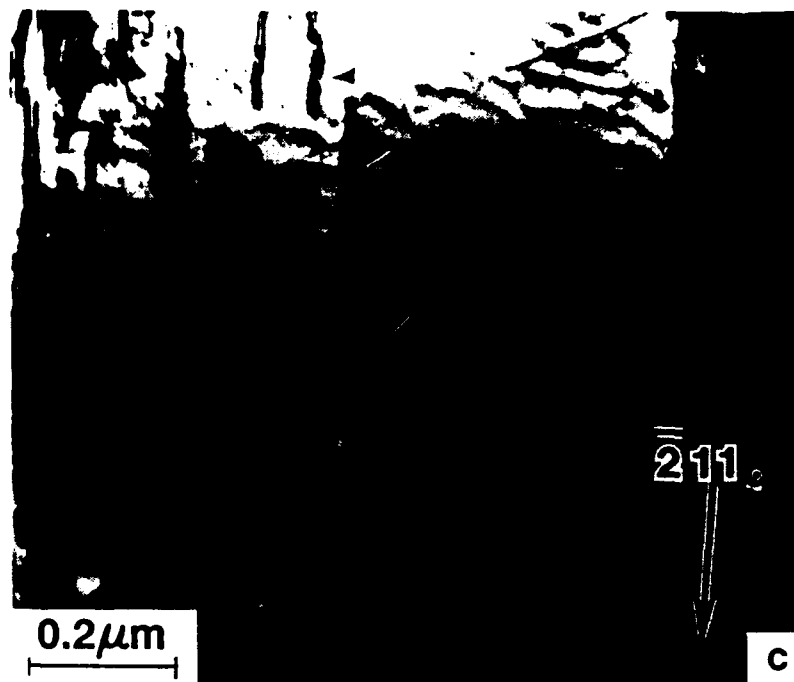


Fig. 5.9(c,d)

necessary but insufficient criteria to firmly establish that \mathbf{u} is parallel \mathbf{b} . Weak-beam and conventional dark-field analyses failed to resolve dislocation pairs or APB's between parallel dislocation lines. Subsequent tilting experiments in prestrained homogeneous B2 have established that these straight dislocations are actually screw dipoles. Generally these dipoles are too closely spaced to produce definite APB contrast [25]. Fig. 5.9d shows lightly deformed jet-polished tensile foils have a hybrid dislocation structure: a few dislocation lines have straight segments and contrast characteristics consistent with screw dislocations such as in the ion-milled material, but the majority of dislocations are the characteristic loops. Moreover, the dislocation densities are essentially unchanged from electropolished foils of unstrained as-received samples.

5.4 Discussion

Although the morphology of the phases directly imaged in the current TEM characterization of the super- α_2 intermetallic, i.e., the hexagonal α_2 and cubic B2, were found to be identical in jet-polished and ion-milled foils, clear differences in the dislocation structures were observed, due to artifacts present in the jet-polished foils. Several factors indicated ion beam thinning preserves the bulk deformation structure. (1) As-received material and β -quenched jet-polished samples displayed similar dislocation structures and densities although thermal and interphase stresses should produce differences. (2) The dislocation densities in jet-polished foils were independent of the degree of prestrain, while dislocation densities in ion-milled foils increased with the amount of deformation. (3) Dislocation loops present in undeformed jet-polished foils were absent in heavily deformed jet-polished material and the dislocation structure strongly resembled heavily deformed ion-milled foils. (4) Lightly deformed (3% tension) jet-polished foils displayed the characteristic dislocation loops, but also contained screw dislocations resembling those in similarly deformed ion-milled foils.

There is considerable indirect evidence that jet polishing stresses may induce shear dislocation loops ($\mathbf{b}=\frac{1}{2}\langle 111 \rangle$) on $\{110\}$ habit planes as artifacts. Obviously the star-shaped buckling patterns around the foil perforation indicate plastic deformation occurred during jet polishing. Burgers vectors and loop habit planes have the correct geometry and EDS data are not contradictory with a conservative shear mechanism. Low dislocation densities in jet-polished B2 samples embrittled by annealing β -quenched material at 400°C indicate material that is resistant to deformation does not form loops, while straight screw dislocations in jet-polished B2 samples deformed before 400°C annealing confirm that the anneal does not remove existing dislocations. Finally, screw dipoles in prestrained ion-milled foils suggest an initial deformation mechanism involving the nucleation of shear loops which expand through glide of edge segments trailing along screw dipoles. Nonconservative APB jet polishing artifacts are not likely because diffusion, which is required to redistribute metal atoms, should be very sluggish at the -30°C polishing temperature. Although trace analysis apparently rules out prismatic dislocation loops, polishing stresses may induce punched prismatic glide which does not require diffusion to produce prismatic dislocation loops.

The observation that ion-milled foils did not develop dislocation loops even when vigorously shaken in the polishing solution at -30°C does not violate the assertion that jet stresses may induce polishing artifacts; ion milling can produce high densities of defect clusters which may impede subsequent nucleation and growth of dislocation loops [39,40]. Furthermore, since high dislocation densities also inhibit dislocation motion, dislocation loop artifacts are absent in jet-polished foils from heavily deformed samples in Fig. 5.8a, when foils thinned from lightly deformed samples (Fig. 5.9d) contain both thinning artifacts and deformation dislocations, as expected. While it has been suggested that ion milling may suppress spontaneous relaxation through the introduction of point defect clusters [32], it may be that inherently lower stresses may be the reason spontaneous relaxation does not occur during ion milling. Thus, gentler electropolishing techniques may also be successful in reducing thinning artifacts. For example, the window technique has successfully inhibited spontaneous relaxation in some conventional β -stabilized titanium alloys [30].

Chemical effects do not appear to play a primary role in artifact formation. While the preferential removal of atoms from one sublattice in the B2 superlattice could conveniently adjust local composition closer to ideal B2 and would create dislocation loops, dislocation contrast analysis and trace analysis largely rule out the prismatic dislocation loops such a process would create and the required diffusion would be too slow. The second argument is heuristic but if diffusion removes material from 20 nm thick foils to form dislocation loops at -30°C in three minutes, such a process would enable decomposition of the metastable B2 phase at ambient temperatures at a scale of 200 nm in hours and microns in days. Hydride formation does not appear to cause the loops. Neither extended contact with the jet polishing solution nor cathodic charging changed the appearance of ion-milled foils. Unfortunately, it is not possible to perform these differential tests on jet-polished foils, and the point defect clusters in ion-milled foils may counteract hydrogen.

While the loop laths in the present study strongly resemble α_2 martensites formed from quenched β in earlier studies on titanium aluminides with lower β -stabilized additions [5,16] and selected area diffraction (SAD) patterns contain diffuse streaks that indicate premartensitic effects [16], no martensite was observed in the present study even in thin foils at liquid nitrogen temperatures. Perhaps there is some interaction with the shear strain waves that give rise to the diffuse streaks in SAD patterns and the jet-induced stresses which generate dislocation loops in martensite-like lath structures. Premartensitic effects may also explain why artifact formation is very sensitive to alloy composition and processing. For example, the enhanced stability of the retained B2 phase in higher α_2 may explain why there was no artifact formation in microstructures with lower B2 volume fractions such as those obtained on furnace cooling. Secondly, alloys that have lower β -stabilizer content may form fine precipitates during quenching which can also suppress artifact formation.

The $\mathbf{g}\cdot\mathbf{b}$ contrast rules used for dislocation analysis are based on isotropic elasticity. The isotropic invisibility criteria $\mathbf{g}\cdot\mathbf{b}_s=0$ (for screw components) and $\mathbf{g}\cdot\mathbf{b}_e=0$ and $\mathbf{g}\cdot(\mathbf{b}_e\times\mathbf{u})=0$ (for edge components) break down as anisotropy increases. There are special dislocation line orientations, namely \mathbf{u} parallel to an even-fold rotational axis or normal to a mirror plane, where the results for isotropic elasticity apply [41]. Although

the dislocations in the current study generally do not satisfy these orientation restrictions, isotropic elasticity provides a good approximation for the observed dislocation contrast; such analysis fails in β -brass (B2 structure), which has an elastic anisotropy ($A=(2c_{44})/(c_{11}-c_{12})$) of 8.5 [41]. Head *et al.* [41] have shown that A largely determines the validity of the isotropic assumption; $\mathbf{g} \cdot \mathbf{b} = 0$ is an effective invisibility criterion over the range $A \approx 0.5-3.0$ [38]. Consequently, the dislocation contrast in the current study indicates the B2 phase in super- α_2 has $A \leq 3.5$. This is plausible since NiAl, which also has the B2 structure, has an $A=3.28$ [38] and exhibits similar premartensitic characteristics to the B2 phase in super- α_2 (additionally, $A=3.33$ [38] in β -AuZn). Finally, dislocation analysis based on elastic isotropy has been successfully applied in a B2 TiNi shape-memory alloy [42].

While ion milling does not introduce dislocations as thinning artifacts, it does generate high densities of defect clusters and surface roughening, which result in mottled images; these mottled structures can conceal small precipitates and microdomains. Since jet polishing apparently does not cause bulk phases to spontaneously transform and is free of the mottling problem, this technique may be preferred for studying phase transformations in super- α_2 intermetallics. It is concluded that ion milling is the preferred foil-preparation technique for characterizing deformation structures in this alloy, as it suppresses spontaneous dislocation formation during thinning of lightly-deformed material; however, jet polishing is acceptable for heavily-deformed material because the higher dislocation densities act to limit thin-foil relaxation.

5.5 Conclusions

Based on a TEM study of the microstructure of super- α_2 intermetallic alloy that was intended to establish the correspondence of thin-foil and bulk phases, deformation structures, and microstructural instabilities, the following conclusions can be made:

1. The B2 phase in jet-polished foils contains high densities of spontaneously generated dislocation loops. These thin-foil artifacts make jet-polished foils unsuitable for the characterization of deformation structures in the super- α_2 alloy.

2. Ion-milled foils, conversely, are found to preserve the bulk deformation structure; defect clusters formed during thinning apparently impede subsequent relaxation. Consequently, jet polishing is an acceptable thinning method for heavily-deformed material since high dislocation densities also act to prevent foil relaxation. Ion-milled foils yield mottled images which make these foils undesirable for precipitation studies because the mottling conceals small intrinsic structures.

3. Dislocation Burgers vectors were $\frac{1}{2}\langle 111 \rangle$ for dislocation loops in jet-polished foils, while screw dipoles were present in lightly-deformed ion-milled foils. These may be the result of rapid movement of the edge segments in shear dislocation loops. Effective invisibility conditions for both the dislocation loops and screw dislocations indicate the elastic anisotropy is in the range 3.0-4.0.

5.6 References

1. J. B. McAndrew and H. D. Kessler, J. Metals, 8 (1956) p. 1348.
2. D. Shechtman, M. J. Blackburn, and H. A. Lipsitt, Metall. Trans., 5 (1974) p. 1373.
3. H. A. Lipsitt, D. Shechtman, and R. E. Schafrik, Metall. Trans. A, 6A (1975) p. 1991.
4. S. M. L. Sastry and H. A. Lipsitt, Acta Metall., 25 (1977) p. 1279.
5. S. M. L. Sastry and H. A. Lipsitt, Metall. Trans. A, 8A (1977) p. 299.
6. M. G. Mendiratta and H. A. Lipsitt, J. Mater. Sci., 15 (1980) p. 2985.
7. H. A. Lipsitt, R. E. Schafrik, and D. Shechtman, Metall. Trans. A, 11A (1980) p. 1369.
8. D. L. Martin, M. G. Mendiratta, and H. A. Lipsitt, Metall. Trans. A, 14A (1983) p. 2170.
9. H. A. Lipsitt, in High Temperature Ordered Intermetallic Alloys, C. C. Koch, C. T. Liu, and N. S. Stoloff, eds., MRS, Pittsburgh, PA, 1985, p. 351.
10. R. A. Perkins, K. T. Chiang, and G. H. Meier, Scripta Metall., 21 (1987) p. 1505.
11. P. R. Munroe and I. Baker, Structural Intermetallic Compounds: Metals and Materials (July 1988) p. 435.
12. C. Young-Won Kim, J. Metals, 42 (July 1989) p. 24.
13. M. J. Blackburn, Trans. Met. Soc. AIME, 239 (1967), p. 1200.
14. J. L. Murray, Metall. Trans. A, 19A (1988) p. 243.
15. C. McCullough, J. J. Valencia, H. Mateus, C. G. Levi, and R. Mehrabian, Scripta Metall., 22 (1988) p. 1131.
16. R. Strychor, J. C. Williams, and W. A. Soffa, Metall. Trans. A, 19A (1988) p. 225.
17. J. Wittenauer, C. Bassi, and B. Walser, Scripta Metall., 23 (1989) p. 1381.
18. H. Bohm and K. Lohberg, Z. Metallk., 49 (1958) p. 173.
19. T. Hanajima, G. Lütjering, and S. Weismann, Metall. Trans., 4 (1973) p. 847.
20. T. Hanajima and S. Weismann, Metall. Trans. A, 6A (1975) p. 1935.
21. D. Banjaree, J. Nandi, and A. K. Gogia, Scripta Metall., 21 (1987) p. 597.
22. T. T. Nartova and G. G. Sopochnik, Russian Metallurgy (Metally), 2 (1970) p. 138.
23. O. N. Andreyev, Russian Metallurgy (Metally), 2 (1970) p. 127.

24. S. R. Seagle and L. J. Bartle, in Titanium and Titanium Alloys, M. J. Corchie, ed., ASM, Metals Park, OH, 1982, p. 23.
25. L. H. Edelson and R. O. Ritchie, Scripta Metall., 24 (1990) in review.
26. D. Banjaree, A. K. Gogia, T. K. Nandi, and V. A. Joshi, Acta Metall., 36 (1988), p. 871.
27. P. B. Aswath and S. Suresh, Mater. Sci. Eng., A114 (1989) p. L5.
28. Microstructures of Titanium and Titanium Alloys, Metals Handbook, 5th ed., vol. 7, ASM, Metals Park, OH, 1977.
29. M. J. Blackburn and J. C. Williams, Trans. Met. Soc. AIME, 239 (1967) p. 287.
30. R. A. Spurling, Metall. Trans. A, 6A (1975) p. 1660.
31. M. G. Mendiratta, G. Lütjering, and S. Weissman, Metall. Trans., 2 (1971) p. 2599.
32. R. A. Spurling, C. G. Rhodes, and J. C. Williams, Metall. Trans., 5 (1974) p. 2597.
33. H. J. Rack, D. Kalish, and K. D. Fike, Mater. Sci. Eng., 6 (1970) p. 181.
34. R. H. Ericksen, R. Taggart, and D. H. Polonis, Trans. Met. Soc. AIME, 245 (1969) p. 359.
35. G. Sanderson and J. C. Scully, Trans. Met. Soc. AIME, 239 (1967) p. 1883.
36. E. Manor and D. Eliezer, Scripta Metall., 23 (1989) p. 1313.
37. D. S. Shih, G. K. Scall, and G. Z. Wasielewski, Scripta Metall., 23 (1989) p. 973.
38. J. W. Edington, in Practical Electron Microscopy in Materials Science, Monograph 3: Interpretation of Transmission Electron Micrographs, Philips, Eindhoven, 1974, Sections 3.4.3 and 3.5, p. 97.
39. J. A. Venables and R. W. Balluffi, Phil. Mag., 11 (1965) p. 1021.
40. M. W. Thompson, Defects and Radiation Damage in Metals, Cambridge University Press, Cambridge, England, 1969, p. 316 ff.
41. A. K. Head, P. Humble, L. M. Clarebrough, A. J. Morton, and C. T. Forwood, Computed Electron Micrographs and Defect Identification, North Holland Publishing Co., New York, NY, 1973.
42. D. Kuskimaki, M. J. Marcinkowski, and A. S. Sastri, Trans. Met. Soc. AIME, 245 (1969) p. 1883.

6. ACKNOWLEDGEMENTS

This work was supported by the U.S. Air Force Office of Scientific Research under Grant No. AFOSR-87-0158, with Dr. A. H. Rosenstein as contract monitor. The authors would like to thank Alcoa, specifically Drs. R. J. Bucci and L. N. Mueller, for supplying the ARALL Laminate materials, the Lockheed Palo Alto Research Laboratories, specifically Drs. T. G. Nieh and J. Wadsworth, for supplying the SiC-fiber continuously-reinforced aluminum-alloy sheet, Mr. R. Friedman of Grumman Aerospace for providing titanium-matrix composites, and Dr. N. E. Paton of Rocketdyne for providing the titanium aluminide intermetallic alloys.

7. PROGRAM ORGANIZATION AND PERSONNEL

The work described was performed in the Department of Materials Science and Mineral Engineering, University of California in Berkeley, under the supervision of Dr. R. O. Ritchie, Professor of Materials Science, aided by a research engineer, graduate student research assistants and undergraduate research helpers. The individual personnel are listed below:

- i) Professor R. O. Ritchie, Principal Investigator
(Department of Materials Science and Mineral Engineering)
- ii) Dr. K. T. Venkateswara Rao, Assistant Research Engineer
(Department of Materials Science and Mineral Engineering)
- iii) Dr. J.-K. Shang, Post-Doctoral Investigator (10/1 - 12/31/89)[†]
(Department of Materials Science and Mineral Engineering)
- iv) S. C. Siu, Graduate Student Research Assistant
(Department of Materials Science and Mineral Engineering)
- v) L. H. Edelson, Graduate Student and IBM Fellow
(Department of Materials Science and Mineral Engineering)
- vi) D. Kovar, Undergraduate Engineering Aide
(Department of Materials Science and Mineral Engineering)

[†]Currently Assistant Professor, University of Illinois at Urbana-Champaign.

8. PUBLICATIONS

8.1 Refereed Journals

1. R. O. Ritchie, W. Yu, and R. J. Bucci, "Fatigue Crack Propagation in ARALL Laminates: Measurement of the Effect of Crack-Tip Shielding from Crack Bridging," Engineering Fracture Mechanics, vol. 32, 1989, pp. 361-377.
2. L. H. Edelson and R. O. Ritchie, "Microstructural Characterization of α_2 +B2 Titanium Aluminide Intermetallic (Super- α_2) Using Transmission Electron Microscopy," Materials Science and Engineering A, 1990, in press.
3. J.-K. Shang and R. O. Ritchie, "Monotonic and Cyclic Crack Growth in TiC Particulate Reinforced Ti-6Al-4V Metal-Matrix Composites," Scripta Metallurgica et Materialia, 1990, in press.

8.2 Invited Presentations

4. R. O. Ritchie, "Kinetics of Subcritical Crack Growth in Advanced Monolithic and Composite Materials," invited presentation to the Gordon Conference on High Temperature Chemistry, Plymouth, NH, July 1988.
5. R. O. Ritchie, "Fracture and Fatigue Testing of Advanced Materials," invited presentation to MTS Systems Corp., Minneapolis, MN, Aug. 1988.
6. Jianku Shang, W. Yu, and R. O. Ritchie, "Mechanisms of Fatigue Crack Propagation in SiC-Reinforced Aluminum Alloy Composites and Laminates," invited presentation at the topical Symposium on Mechanical Properties of Advanced Composites, TMS Fall Meeting, Chicago, IL, Sept. 1988.
7. R. O. Ritchie, "Studies of Fracture and Fatigue in Advanced Materials," Department of Materials Science and Mineral Engineering Seminar, University of California, Berkeley, CA, Nov. 1988.
8. R. O. Ritchie, "Fatigue-Crack Propagation in Metals, Ceramics and the Interfaces that Separate Them," invited plenary lecture at the Seventh International Conference on Fracture, Houston, TX, March 1989.
9. R. O. Ritchie, "Micro-Mechanisms of Fracture in Structural Metals, Ceramics and Composites," invited seminar to the Materials Science and Engineering Dept., University of Washington, Seattle, WA, May 1989.
10. R. O. Ritchie, "Fatigue and Fracture in Composite Metals and Ceramics," invited seminar to Battelle Pacific Northwest Laboratories, Richland, WA, May 1989.
11. R. O. Ritchie, "Mechanisms of Fatigue-Crack Growth in Metals, Composites, Ceramics and Ceramic/Metals Interfaces," invited presentation at the Third International Conference on Fundamentals of Fracture, Irsee, F.R. Germany, June 1989.

12. R. O. Ritchie, "Mechanics of Fatigue and Fracture in Metallic Alloys: Role of Metallic, Ceramic and Polymeric Reinforcements," invited presentation at *Fracture '89*, the Third National Conference on Fracture, Johannesburg, South Africa, June 1989.
13. R. O. Ritchie, "Behavior of Real Materials: Composites," invited presentation at the Physical Metallurgy Gordon Conference, Tilton, NH, August 1989.
14. R. O. Ritchie, "Mechanics and Mechanisms of Fatigue in Advanced Materials," invited seminar to the Research Laboratory of Precision Machinery and Electronics, Tokyo Institute of Technology, Yokohama, Japan, Sept. 1989.
15. R. O. Ritchie, "Mechanical Behavior of Metal-Matrix Composites," invited seminar to Korea Institute of Technology, Seoul, Korea, Sept. 1989.
16. R. O. Ritchie, "Ceramics and Ceramic Composites: Fatigue and Fracture," invited seminar to Materials Research Laboratory, Industrial Technology Research Institute, Hsinchu, Taiwan, Sept. 1989.
17. JianKu Shang and R. O. Ritchie, "Micromechanisms of Fatigue-Crack Growth in Model Particulate-Reinforced Metal-Matrix Composites," ASM Symposium on *Metal-Matrix Composites*, ASM Fall Meeting, Indianapolis, IN, Oct. 1989.
18. JianKu Shang and R. O. Ritchie, "Crack Bridging during Fatigue-Crack Growth in Metal-Matrix Composites," TMS Symposium on *Structure/Property Relationships in Metal-Matrix Composites*, TMS-AIME Fall Meeting, Indianapolis, IN, Oct. 1989.
19. R. O. Ritchie, "Mechanisms of Fracture and Fatigue in Advanced Aerospace Materials," invited presentation to the Australian Aeronautical Conference - 1989 on *Research and Technology - The Next Decade*, Melbourne, Australia, Oct. 1989.
20. R. O. Ritchie and J.-K. Shang, "Fatigue Resistance and Toughening Mechanisms in Particulate-Reinforced Metal-Matrix Composites," invited presentation to SAMrE Australian Chapter Conf. on *Advanced Composites and Materials*, Melbourne University, Australia, Oct. 1989.
21. R. O. Ritchie, "Micromechanisms of Fatigue-Crack Growth in Structural Composites," invited seminar to the Materials Research Laboratory (MRL of the Defence Science and Technology Office), Melbourne, Australia, Oct. 1989.
22. L. H. Edelson, K. T. Venkateswara Rao, and R. O. Ritchie, "Deformation Structures in Super- α_2 Titanium Aluminides," presented at the 119th TMS Annual Meeting, Anaheim, CA, Feb. 1990.
23. R. O. Ritchie and J.-K. Shang, "Fatigue-Crack Propagation in Metal-Matrix Composites," invited paper at the Symposium on *Advanced Metal & Ceramic Matrix Composites*, 119th TMS Annual Meeting, Anaheim, CA, Feb. 1990.

9. DISTRIBUTION LIST

AFOSR/NE

ATTN: Dr. A. H. Rosenstein

Bldg. #410

Bolling Air Force Base

Washington, D.C. 20332

AFWAL/MLLM

ATTN: Branch Chief

Wright-Patterson Air Force Base

Dayton, OH 45433

AFWAL/MLLS

ATTN: Branch Chief

Wright-Patterson Air Force Base

Dayton, OH 45433

AFWAL/MLLN

ATTN: Branch Chief

Wright-Patterson Air Force Base

Dayton, OH 45433

Dr. Hugh R. Gray

NASA Lewis Research Center

Materials and Structures Division

21000 Brookpark Rd.

Cleveland, OH 44135